Near side jet yield from two particle identified triggered correlation in PbPb collisions at 5.02 TeV ALICE

By

SANCHARI THAKUR

PHYS04201504011

Variable Energy Cyclotron Centre, Kolkata

A thesis submitted to

The Board of Studies in Physical Sciences

In partial fulfillment of requirements

For the Degree of

DOCTOR OF PHILOSOPHY

of

HOMI BHABHA NATIONAL INSTITUTE

January, 2022

Homi Bhabha National Institute[1]

Recommendations of the Viva Voce Committee

As members of the Viva Voce Committee, we certify that we have read the dissertation prepared by Sanchari Thakur entitled ”Near side jet yield from two particle identified triggered correlation in PbPb collisions at 5.02 TeV ALICE” and recommend that it may be accepted as fulfilling the thesis requirement for the award of Degree of Doctor of Philosophy.

Chairman–⟨Prof. Jane Alam⟩	Jane Alam	**Date**: 7.01.2022
Guide/Convener–⟨Prof. Subhasis Chattopadhyay⟩		**Date**: 7.01.2022
Examiner–⟨Dr. Prabhat Ranjan Pujahari⟩	Prabhat R. Pujahari	**Date**: 7.01.2022
Member 1–⟨Prof. Premomoy Ghosh⟩	07/01/22	**Date**: 7.01.2022
Member 1–⟨Prof. Gargi Chaudhury⟩	Gargi Chaudhuri	**Date**: 7.01.2022
Member 2–⟨ Prof. Abhijit Bhattacharya⟩	Abhijit Bhattacharyya 7/1/2022	**Date**: 7.01.2022

Final approval and acceptance of this thesis is contingent upon the candidate’s submission of the final copies of the thesis to HBNI.

I hereby certify that I/we have read this thesis prepared under my direction and recommend that it may be accepted as fulfilling the thesis requirement.

Date: 7.01.2022

Guide: Dr. Subhasis Chattopadhyay

Place: VECC, KOLKATA

---

[1] This page is to be included only for final submission after successful completion of viva voce.

STATEMENT BY AUTHOR

This dissertation has been submitted in partial fulfillment of requirements for an advanced degree at Homi Bhabha National Institute (HBNI) and is deposited in the Library to be made available to borrowers under rules of the HBNI.

Brief quotations from this dissertation are allowable without special permission, provided that accurate acknowledgement of source is made. Requests for permission for extended quotation from or reproduction of this manuscript in whole or in part may be granted by the Competent Authority of HBNI when in his or her judgment the proposed use of the material is in the interests of scholarship. In all other instances, however, permission must be obtained from the author.

Sanchari Thakur

Sanchari Thakur

DECLARATION

I, hereby declare that the investigation presented in the thesis has been carried out by me. The work is original and has not been submitted earlier as a whole or in part for a degree / diploma at this or any other Institution / University.

Sanchari Thakur

Sanchari Thakur

List of Publications

List of published and communicated journals

1. S. Thakur, S. K. Saha, P. Dasgupta, R. Chatterjee and S. Chattopadhyay, Nucl. Phys. A **1014** (2021), 122263 doi:10.1016/j.nuclphysa.2021.122263 [arXiv:2101.09998 [nucl-th]].
2. S. Basu, S. Thakur, T. K. Nayak and C. A. Pruneau, J. Phys. G **48** (2020) no.2, 025103 doi:10.1088/1361-6471/abc05c [arXiv:2008.07802 [nucl-ex]].
3. M. Mukherjee, S. Basu, A. Chatterjee, S. Chatterjee, S. P. Adhya, S. Thakur and T. K. Nayak, Phys. Lett. B **784** (2018), 1-5 doi:10.1016/j.physletb.2018.07.021 [arXiv:1708.08692 [nucl-ex]].
4. S. Thakur, S. K. Saha, S. N. Alam, R. Chatterjee and S. Chattopadhyay, [arXiv:2109.07225 [nucl-th]] (Accepted for publication).
5. S. Muhuri, S. Mukhopadhyay, V. B. Chandratre, T. K. Nayak, S. K. Saha, S. Thakur, R. N. Singaraju, J. Saini, A. van den Brink and T. Chujo, *et al.* JINST **15** (2020) no.03, P03015 doi:10.1088/1748-0221/15/03/P03015 [arXiv:1911.00743 [physics.ins-det]].

List of conferences and symposia

1. S. Thakur, K. Dutta, S. P. Adhya, T. K. Nayak and S. Basu, DAE Symp. Nucl. Phys. **61** (2016), 854-855
2. S. Thakur, T. K. Nayak and S. Basu, DAE Symp. Nucl. Phys. **61** (2016), 856-857
3. M. Mukherjee, S. Basu, S. Thakur, S. Choudhury, S. Chatterjee and T. K. Nayak, DAE Symp. Nucl. Phys. **61** (2016), 758-759
4. M. Mukherjee, S. Basu, S. Thakur, S. P. Adhya, A. Chatterjee, S. Chatterjee and T. K. Nayak, EPJ Web Conf. **171** (2018), 14010 doi:10.1051/epjconf/201817114010

5. S. Muhuri, S. Mukhopadhay, S. K. Saha, S. Thakur, V. B. Chandratre, S. A. Khan, T. K. Nayak, J. Saini, R. N. Singaraju and M. Sukhwani, DAE Symp. Nucl. Phys. **61** (2016), 748-749
6. Correlation between initial spatial anisotropy and final momentum anisotropies in relativistic heavy ion collisions, PoS(LHCP2021)204 (Proceedings)
7. S. Thakur, S. K. Saha, Sk. N. Alam, R. Chatterjee and S. Chattopadhyay, Proceedings of the DAE Symp. on Nucl. Phys. 65 (2021)

Sanchari Thakur

Sanchari Thakur

Dedicated to my beloved supportive parents
who are the biggest source of motivation
and encouragement to complete this thesis

ACKNOWLEDGEMENTS

I would like to thank my supervisor Dr. Subhasis Chattopadhyay for his support and encouragement. I am thankful to my ALICE PWG-CF convenors Malgorzata Anna Janik and Davide Caffari for their constant help in my analysis. Without them, I could not do my analysis. They helped me in every step whenever I faced any problem. I thank my senior Dr. Noor Alam, Dr. Subikash Choudhury, Dr. Debojit Sarkar and Dr. Sumit Basu for their help and useful discussions. I specially thank Dr. Noor Alam and Dr. Subikash Choudhury for helping me whenever I needed. I am thankful to my senior Dr. Arghya Chatterjee and Dr. Rajendra Nath Patra for their helpful discussion, suggestions, support and encouragement. I am very much thankful to Dr. Rupa Chatterjee and Dr. Pingal Dasgupta for their constant help and suggestions and I am really very fortunate to work with them. I am grateful to VECC grid for helping me in my work. I specially thank Abhisek Seal and Prasun Sing Roy for their constant help in my work without whom I could not pursue my work. I thank Dr. Saikat Biswas for motivating me and giving me helpful suggestions. I thank Dr. Tilak Kumar Ghosh for helping, motivating and encouraging me. I would like to thank Prof. Tapan K. Nayak for useful physics discussions and suggestions. I thank Dr. Jane Alam, Dr. Sourav Sarkar ,Dr. Zubayer Ahmed, Dr. Anand Dubey, Dr. Premomoy Ghosh for useful discussions. I also like to thank my committee members Dr. Abhijit Bhattacharya and Dr. Gargi Chaudhury. I thank my seniors Dr. Nachiketa Sarkar, Dr. Ashik Ikbal, Dr. Samranjy Sadhu, my friends Shreyasi Acharya, Sinjini Chandra, Mitali Mondal, Soumen Nandi, Santanu Pathak, Mahfuzur Rahman and my juniors Dipen Paul,Vivek Kumar Sing, Sudipta Mohsat with whom I enjoyed a lot to work and spend many memorable moments. Finally, I thank Sumit and my parents for being the source of continuous, endless support, encouragement and inspiration over years and giving me motivation at every step.

Sanchari Thakur

Sanchari Thakur

Contents

Synopsis

0.1 Introduction

As per the prediction on Quantum ChromoDynamics (QCD), the theory of strong interaction, when the temperature and energy density are very high, the quarks and gluons cannot stay bound anymore inside the hadrons and can exist as asymptotically free in a volume comparable to the nuclear volume. This deconfined state of quarks and gluons is called QGP (Quark-Gluon-Plasma) which is known to prevail in our early universe about a microsecond after the Big Bang when the temperature was very high [1, 5]. As the temperature of the expanding universe decreased, the quarks and gluons fragment to form hadrons. The transition from the QGP to hadronic state can be depicted by a diagram of baryonic chemical potential (μ_B) vs. temperature (T) commonly known as the phase diagram of the strongly interacting matter. The transition is expected to be of first-order at low temperature $\sim$ 50 MeV and high μ_B , whereas, at very high temperature $\sim$ 150 MeV and very low μ_B, the transition is a smooth crossover. A critical point is expected to lie at the junction between these two types of transitions. Experiments are being carried out worldwide to study the formation of QGP in the laboratory. This is performed by creating a high energy density region ($> 1\, GeV/fm^3$) by colliding $Pb + Pb$ nuclei at Large Hadron Collider (LHC) , CERN and $Au + Au$ at Relativistic Heavy Ion Collider (RHIC), BNL. ALICE at LHC-CERN and STAR, PHENIX at RHIC-BNL are among the experiments dedicated to study the properties of the QGP medium and its evolution to hadrons . Results from the experiments at RHIC have indicated the formation of a strongly coupled nearly perfect liquid in central Au-Au collisions at $\sqrt{s_{NN}} = 200$ GeV [2, 3, 4]. The matter created in Pb-Pb collisions at LHC energies shows similar behaviour. The properties of particles produced in the collisions reflect the production mechanism and thereby the characteristics of the medium created. The distributions of the longitudinal momenta of the produced particles represented by rapidity (y) or pseudorapidity (η) and the transverse momenta (p_T) of the produced particles provide basic information about the medium. The η-distributions and their dependence on various observables provide information on energy density, entropy, mechanism of particle production. The transverse momentum (p_T) distribution of the produced particles on the other hand characterizes the medium like thermalization, temperature among others [6, 7, 8]. The lower part of the p_T spectrum at LHC energy, i.e., up to $p_T = 2$ GeV/c follows an exponential distribution and the higher p_T part ($> 6\ GeV/c$) follows the power law. The particle production in the lower p_T region is expected to be explained using the hydrodynamical evolution of the bulk matter, whereas, at higher p_T region, particles are produced mainly from the fragmentation of partons. The particle production at an intermediate p_T (2-6 GeV/c) cannot be described fully by either of these processes or a combined one. An observed enhanced yield of baryons relative to that of the mesons in this p_T range was an interesting observation at RHIC [9]. Also, the nuclear modification factor R_{AA} which measures the p_T dependent particle yield in nucleus-nucleus collisions with respect to that in pp collisions, shows lower suppression for baryons compared to that for mesons at the intermediate p_T [10, 11]. It was initially established experimentally that the observed suppression is due to the energy loss of partons in the medium [12]. But the absence of similar effect in proton yield was puzzling. Later, it is proposed that the particle production at the intermediate p_T can mainly be explained as due to the recombination of constituent quarks or quark coalescence rather than fragmentation

[13, 14, 15] . The Number of Constituent Quark (NCQ) scaling which shows the similarity of baryon and meson properties (like variation of particle yield, v_2 etc. with p_T) after scaling it by the corresponding constituent quarks numbers is one of the natural consequences of the recombination model. However, the situation is somewhat different at LHC energies. ALICE experiment showed that the scaling properties are deviated by almost 20% at all centralities [16] . On the other hand, in models other than that of the recombination, the radial flow pushing the massive baryons towards higher p_T or the baryon production from gluon junction have been found to reproduce the observed baryon enhancement over mesons. This scaling property apart from baryon to meson enhancement should also be reflected in the measurement of hadronic correlations.

0.2 Measurements of two particle correlation at intermediate p_T

Two particle correlation is a powerful tool to explore the properties of the hot and dense medium produced in heavy ion collision and the underlying particle production mechanism. For example, it offers a convenient way to probe the medium effect on the jet-fragmentations which cannot be studied well through inclusive measurements. In this thesis, two particle correlations in $(\Delta\eta, \Delta\phi)$ space with pions and protons as trigger and charged hadrons as associated particles are studied in PbPb collision at 5.02 TeV , where $\Delta\eta$ and $\Delta\phi$ are the relative pseudo-rapidity and azimuthal angle between the trigger and the associated particles. The particles generated from a di-jet fragmentation are correlated in azimuthal plane near $\Delta\phi \approx 0$ and $\Delta\phi \approx \pi$ (commonly known as near and away side peaks, respectively). The trigger particles are chosen in the intermediate p_T range $2\,GeV/c < p_T < 4\,GeV/c$ as it has contributions from both soft and hard processes of particle production. The correlation strength of the near side jet-like yield is measured. Comparing the per-trigger yields of pion and proton triggered correlations as a function of centrality can shed light on the particle production mechanism at intermediate p_T. Unidentified associated particles are chosen in the range of $1\,GeV/c < p_T < 4\,GeV$. Particles are identified using ALICE TPC and TOF by a combined $n\sigma$ method that was the combination of particle dependent energy deposition in TPC and time of flight in TOF detectors. The correlation function is corrected for limited acceptance by mixed event method. The measured correlated yields need to be corrected for finite detector efficiencies and contaminations due to the misidentifications of particles. A Monte Carlo simulation technique has been used to obtain these correction factors passing through the GEANT simulation package to include the detector related effects. The detector geometry and reconstruction procedures used in MC are the same as in data. To validate the procedure, a closure test is performed by taking the ratio of the input and reconstructed observables.

The near side jet yield is extracted after subtracting the flow-modulated background. If the baryon enhancement is due to coalescence mechanism which is not correlated to the charged hadrons, then the per-trigger yield will be diluted for protons compared to that for pions. This dilution will be more in the central collision as the medium effect is stronger there. Finally, the uncertainties in the measurements are estimated. Uncertainties are mainly classified into two types, one is the statistical uncertainty representing the robustness of the observable with respect to the event statistics and the second one is the systematic uncertainty, which represents the variation of the observable with respect to the variation of different selection criteria etc. The statistical uncertainty estimation is based on the numerical error propagation method and the systematic uncertainties are estimated by varying different track quality cuts, tracking efficiency and conditions for particle identification. Fig. 1(a) represents the fully corrected 2D-correlation plots with pion trigger for three centralities and Fig. 1(b) represents the near side yield variation with centrality along with model comparison.

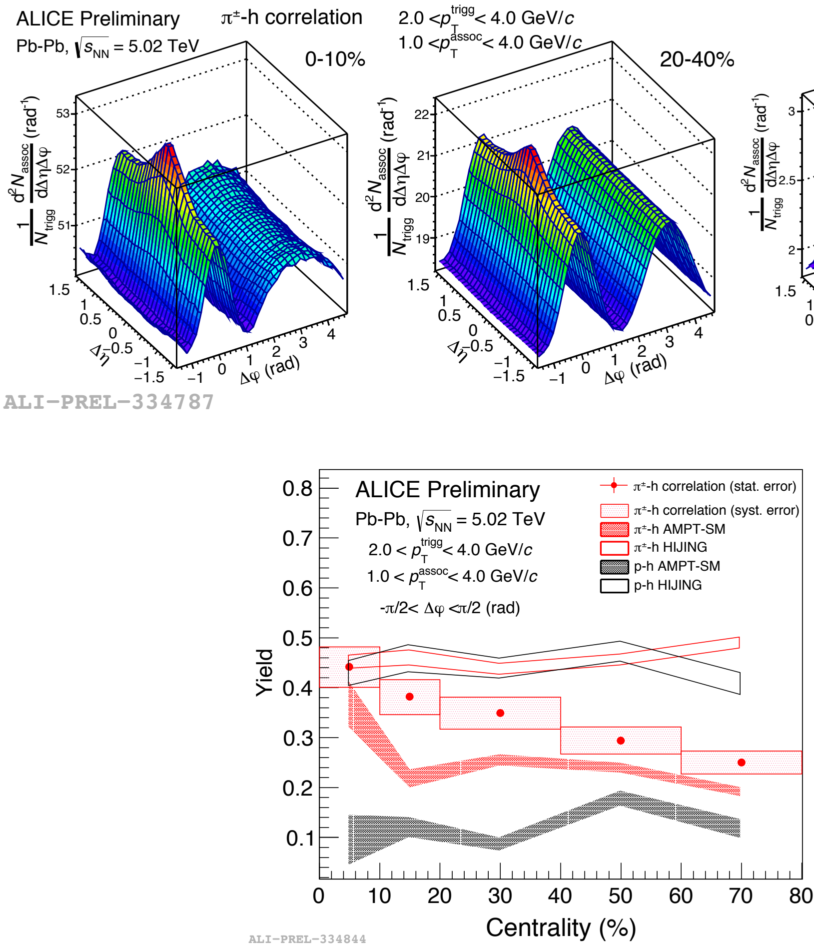

Figure 1: (a) Top panel: Pion triggered 2D correlation for three centralities (b) Bottom panel: Near side pion triggered yield as a function of centrality with model comparison (statistical errors are shown as vertical lines and systematics errors are as boxes)

0.3 Pseudorapidity distribution: a systematic study

As a part of the thesis, a comprehensive study of the multiplicity and pseudorapidity distributions of charged particles produced in p-p, p-Pb, d-Au, Cu-Cu, Au-Au and Pb-Pb collisions at energies ranging from a few GeV to several TeV, corresponding to the available experimental data at RHIC and LHC are presented. With the goal of extrapolating the measured data to forward rapidities to estimate the total charged particle production in various collision systems and to obtain the dependence on the collision energy, three different functional forms to describe the experimental data on the pseudorapidity distributions have been studied. One of these functional forms, the difference of two Gaussian distributions best reproduces the measured multiplicity densities at different collision systems and collision energies.

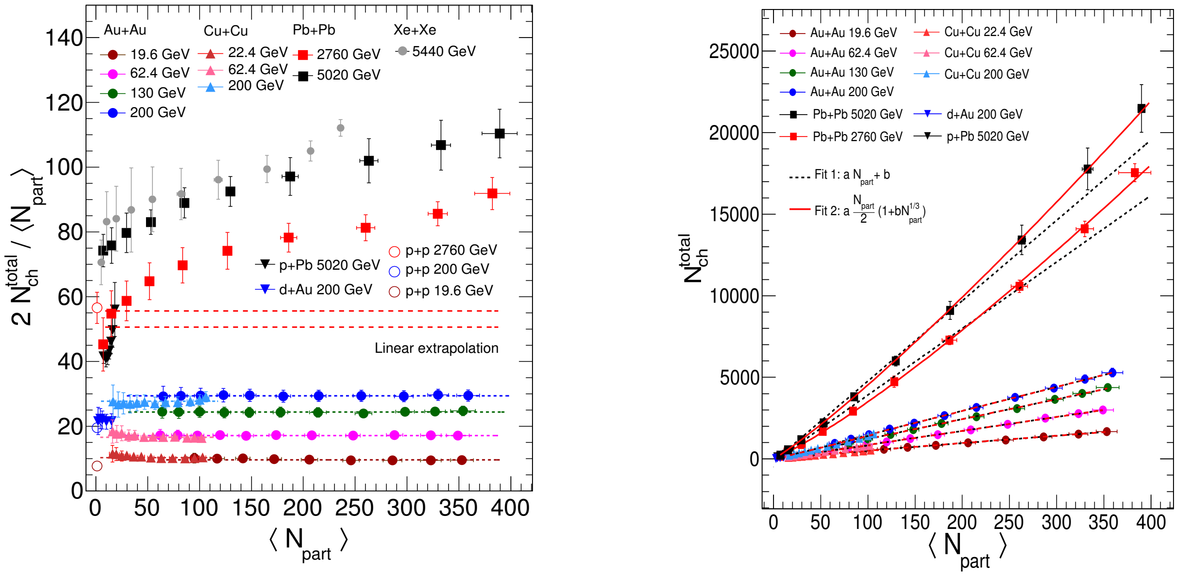

Figure 2: Left: Centrality dependence of total charged multiplicity per participant pair in pp, p+Pb, d+Au, Cu+Cu, Au+Au and Pb+Pb collisions at RHIC and LHC energies Right: Centrality dependence of the total charged-particle multiplicity, estimated from integrals of Eq. (3) across the full rapidity range

The limiting fragmentation behavior in these collisions are studied and evidence for participant scaling violations in high-energy collisions at the TeV energy scale shown in Fig.2 is reported. It is concluded that there is a qualitative change in the particle production at LHC relative to that at RHIC. In addition, charged-particle multiplicity productions considering different initial conditions have been studied. It is found that Color Glass Condensate like initial condition is best suited to describe the published data for both symmetric and asymmetric types of collisions. The particle production studies to lower collision energies corresponding to those of upcoming accelerator facilities of FAIR at GSI, Darmstadt and NICA at Dubna have been extended.

0.4 Correlation between flow coefficients in high energy heavy ion collision

As a part of the thesis, the correlation between the initial spatial anisotropy and the final momentum anisotropy for positively charged pions, kaons and protons in Pb+Pb collisions at 2.76 TeV LHC energy for different centrality bins using an event-by-event viscous hydrodynamic model framework with fluctuating initial conditions has been calculated. The linear correlation is found to be stronger for central collisions than for peripheral collisions for all the particles. In addition, the correlation between $v_3 - \epsilon_3$ is found to be weaker compared to that for $v_2 - \epsilon_2$. However, the correlation between $v_n(p_T)$ and ϵ_n as a function of p_T shows interesting behaviour where the correlation coefficient C is found to depend strongly on the mass of the particles in Pb+Pb collisions.

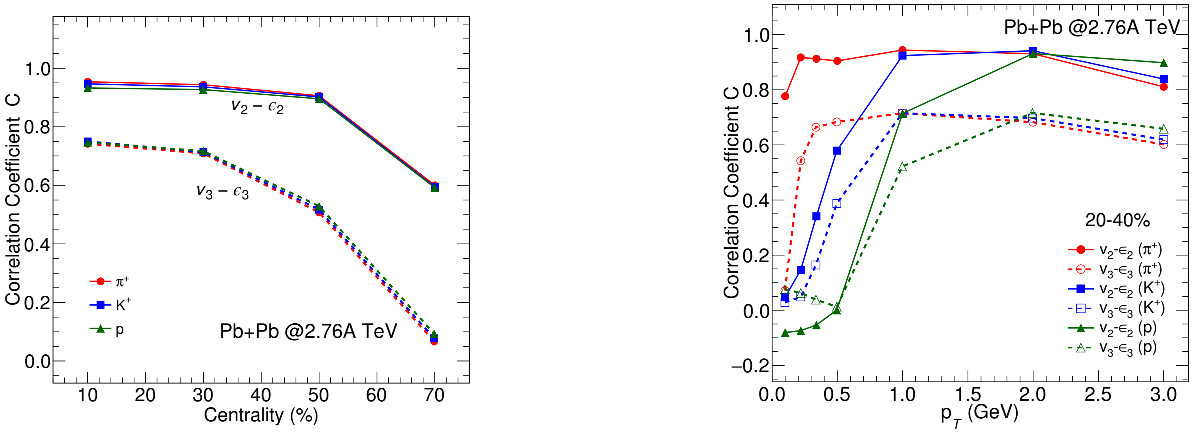

Figure 3: Left: C(ϵ_n, v_n) as a function of centrality from 2.76A TeV Pb+Pb collisions at LHC Right: Correlation between ϵ_n and $v_n(p_T)$ for π^+, K^+ and p at $\sqrt{s_{NN}} = 2.76$ TeV Pb+Pb collisions for $20 - 40\%$ centrality bin

Bibliography

[1] P. Braun-Munzinger and J. Stachel, Nature **448**, 302 (2007). doi:10.1038/nature06080

[2] G. Kestin and U. W. Heinz, Eur. Phys. J. C 61, 545 (2009).

[3] H. Song, S. A. Bass, U. Heinz, T. Hirano, C. Shen, Phys. Rev. Lett. 106, 192301 (2011).

[4] D. Teaney, J. Lauret and E. V. Shuryak, Phys. Rev. Lett. 86, 4783 (2001).

[5] F. Karsch, Nucl. Phys. A **698** (2002), 199-208 doi:10.1016/S0375-9474(01)01365-3

[6] J. L. Klay et al. (STAR Collaboration), Nucl. Phys. A, 715-733 (2003).

[7] S. S. Adler et al. (PHENIX Collaboration), Phys. Rev. C 69, 034909 (2004).

[8] B. Ablev et al. (ALICE Collaboration), Phys. Rev. C 88, 044910 (2013).

[9] T. Sakaguchi [PHENIX], Nucl. Phys. A **715** (2003), 757-760 doi:10.1016/S0375-9474(02)01482-3

[10] B. Ablev et al. (ALICE Collaboration) Phys. Lett. B. 736, 196-207 (2014).

[11] B. I. Abelev et al. (STAR Collaboration) Phys. Rev. Lett. 97, 152301 (2006).

[12] C. Adler *et al.* [STAR], Phys. Rev. Lett. **89** (2002), 202301 doi:10.1103/PhysRevLett.89.202301

[13] R. Fries, B. Muller, C. Nonaka, and S. Bass, Phys. Rev. Lett. 90, 202303 (2003)

[14] R. J. Fries, B. Muller, C. Nonaka and S. A. Bass , Phys. Rev. C 68, 044902 (2003)

[15] R. J. Fries, S. A. Bass and B. Muller Phys. Rev. Lett. 94, 122301 (2005)

[16] B. B. Abelev *et al.* [ALICE], JHEP **06** (2015), 190 doi:10.1007/JHEP06(2015)190

[17] S.S. Adler et. al (PHENIX Collaboration) Phys. Rev. C 71, 051902 (2005).

[18] L. Adamczyk et al. (STAR Collaboration), Phys. Lett. B 751, 233 (2015).

[19] R. J. Fries, S. A. Bass and B. Muller, Phys. Rev. Lett. **94** (2005), 122301

List of Figures

List of Tables

Chapter 1

Introduction

According to the Big Bang theory, the Universe started from a point of infinitesimally small volume with very high temperature and energy density called the singularity about 13.8 billions of years ago. All the matters were compressed into a single point and this point exploded and then started expanding [2].This is considered to be the beginning of space and time. The evolution of the universe from Big bang is shown schematically in Fig. 1.1. In the early universe, immediately after the Big Bang when the temperature was extremely high [3], all the four forces were united to a single force. After $\sim 10^{-43}$ sec of Big Bang, the gravitational force got separated first, then the strong force and finally the electromagnetic and weak forces split after $\sim 10^{-11}$ sec of the Big Bang. The universe was so hot that the quarks and gluons, participants in the strong force, were free. The universe was then filled with the hot and dense quark gluon plasma. This stage is known as the Quark Epoch. At about 10^{-6} sec after the Big Bang when the temperature was about 0.2

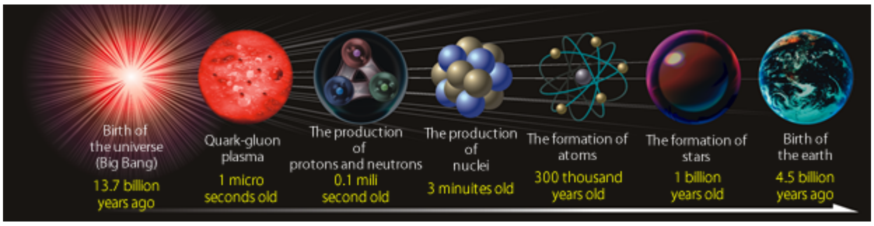

Figure 1.1: Evolution of the universe after Big Bang [5]

GeV, a transition from the phase of quark-gluon-plasma to hadronic matter happened. This is known as the Hadron Epoch. After that, protons and neutrons got combined to form nuclei. After that, the atoms, molecules and the matter were formed. Similar conditions like the microsecond old universe is believed to have been created in the laboratory by colliding two heavy nuclei [4].

1.0.1 Standard Model of elementary particles

Now, to understand the formation of matter and their interactions, it is necessary to know the fundamental forces of nature and the composition of matter. The Standard Model is a theoretical model that describes the interactions among the elementary particles and the force carriers [Fig. 1.2]. According to the Standard Model, the elementary particles are divided into two groups - quarks and leptons. Matter is made up of molecules which consist of atoms. An atom consists of a nucleus made of protons and neutrons surrounded by an electron cloud. Inside protons and neutrons, quarks are bound by strong interactions mediated by the exchange of gluons. On

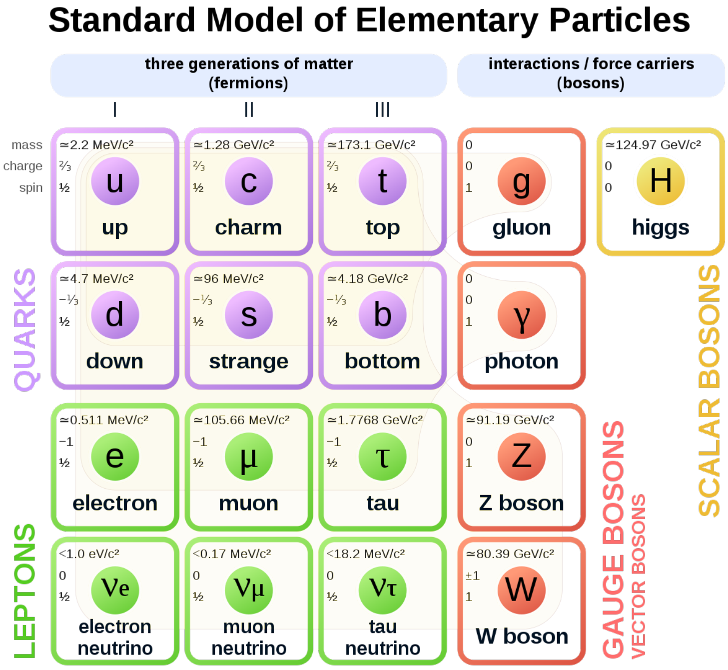

Figure 1.2: Elementary particles in Standard model [6]

the other hand, the four fundamental forces of nature are Gravitational, electromagnetic, weak and strong force. The Gravitational force, acting between any two objects are attractive and of long range. The long ranged electromagnetic forces act between any two charged particles mediated by photons and can be attarctive or repulsive depending on the nature of charges. The short ranged weak force is responsible for β decay and of neutrino interactions which is mediated by bosons and the strong nuclear force, which is of shortest range, holds neutrons and protons together inside a nucleus, gluons are mediator of strong force. The Standard model has a set of theories describing the interactions. The Quantum Electro Dynamics (QED) is the theory of electromagnetic interaction, the Electro-weak theory is the theory for weak and electromagnetic interaction and the strong interactions are described by the Quantum Chromo Dynamics (QCD) [1]. According to QCD, the hadrons are formed by quarks and gluons that interact strongly by color exchange which is a quantum number analogous to the electric charge. Inside a hadron, quarks are almost free, but if they are separated, the force increases linearly. This is known as the asymptotic freedom i.e. the strength of interaction becomes weaker when the distance becomes shorter which is of opposite trend to that of the electromagnetic interaction. The strong coupling constant is defined as, $\alpha_s(Q^2) = \frac{12\pi}{(33-2n_f)ln(Q^2/\lambda^2_{QCD})}$, where Q^2 is the momentum transfer [7, 8]. Therefore, at very high energy density and temperature i.e. for high momentum transfer, the coupling constant decreases and therefore the confinement of the quarks and gluons inside hadrons is not possible any more. They are like free particles in a state called QGP [9, 10].

1.0.2 Quark-Gluon-Plasma and the QCD phase diagram

The goal of the experiments with nuclear collisions at high energy is to create a state of deconfined quarks and gluons in the laboratory similar to that existed in the early universe. This can be produced for a very short time and over a nuclear volume by colliding nuclei at ultra relativistic energies. The first search of such a state of matter began at Bevalac at Barkeley National Lab, USA using Au beam at 1 GeV/nucleon hitting a target. A number of experiments were performed subsequently in search of QGP at the Alternate Gradient Synchrotron (AGS), BNL, USA and at the Super Proton Synchrotron (SPS), CERN, Geneva like NA49,WA98 among others. Then, the Relativistic Heavy Ion Collider (RHIC) at BNL started operation in 2000 with four experiments BRAHMS, PHENIX, PHOBOS and STAR with Au+Au collisions upto $\sqrt{s_{NN}} = 200$ GeV/nucleon. After that, in 2008, experiments were performed at LHC using high energy beams of Pb ions at $\sqrt{s_{NN}} = 2.76$ TeV. In a collision, if the energy density of nuclear matter is high ($\epsilon \approx 1\ GeV/fm^3$) [11], it is predicted that a region of deconfined quarks and gluons will be formed for a very short time, soon after it expands and cools down and they again undergo hadronization. So, knowing about the conditions needed to form the Quark Gluon Plasma phase is important. Calculations have been performed [13, 14] for QCD implemented on a lattice to know the necessary conditions for the formation of the QGP phase and the results are shown [15, 12, 23] in Fig 1.3 for the energy density ϵ normalized by T^4 vs temperature T. The figure shows a first order phase transition

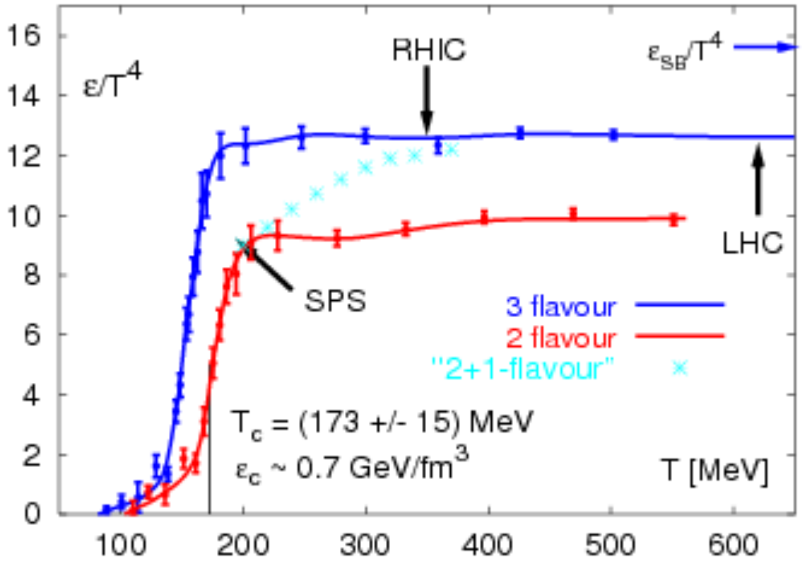

Figure 1.3: Lattice QCD calculation for energy density vs. temperature. [12]

showing an abrupt change of energy density per T^4 around the critical temperature T_C. This calculation gives the critical temperature $T_C \sim 173 \pm 15 MeV$ and the critical energy density $\epsilon_C \sim 0.7 GeV/fm^3$. A similar transition might also take place when the nuclear medium is compressed to a net baryon density of about 2-3 times the nuclear matter density. Such a transition from hadron to QGP and back to hadron is represented by a diagram showing the net baryon density or the baryon chemical potential μ_B, which is the energy needed to add or remove a baryon to the system versus the temperature of the fireball [Fig. 1.4]. The extreme region of high temperature and zero net baryon density is represented by the early universe and has been created at LHC. At low temperature and high net-baryon density, the matter is like that of the core of neutron stars. These two extreme regions are separated by a QCD critical point. Lattice QCD predicts a smooth crossover at high T and low μ_B beyond the critical point [16, 17] and below the critical point, the transition is of the first order [18]. At LHC, a cross-over transition is found to be around T_C =160 MeV. The top RHIC and LHC energies fall in the high temperature region and SPS, AGS and the upcoming FAIR , NICA and low energies at RHIC probe mostly the high net baryon density region.

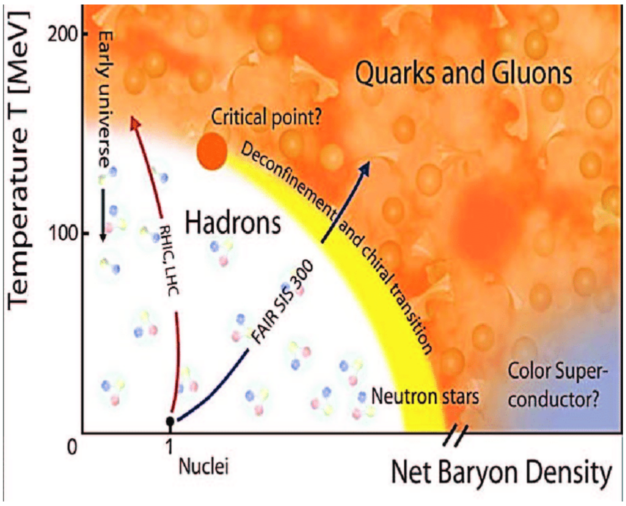

Figure 1.4: A schematic of QCD phase diagram. [20]

Now, to talk about the thermodynamic phases, phase transition, temperature etc, the system

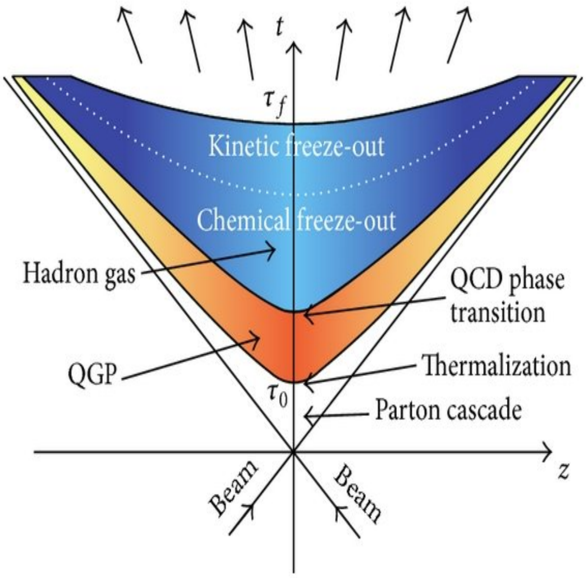

Figure 1.5: Space-time evolution of a heavy ion collision [21]

must consist of a large number of particles with respect to its size and it should reach local thermal equilibrium, therefore a sufficient number of interactions must occur for equilibration and for this, the mean free path should be much smaller compared to the system size. At very high collision energy, the gluons dominate over quarks and the interactions among the quarks are very small. So they are basically transparent in the medium and they just pass through without interaction, thereby resulting in very small net-baryon density in the central region. The particles are then produced from a gluonic medium. It is assumed that the particle production occurs when the fireball reaches an equilibrium temperature, volume and baryon-chemical potential. The space-time evolution of the created matter in a high energy collision is shown in Fig.1.5. Initially, the quarks and gluons are not thermalized. They gradually interact and equilibrate. The typical formation time of QGP is about 1 fm/c and the lifetime of QGP phase is about 8 fm/c. As the system expands and cools, quarks and gluons are combined to form hadrons. If the phase transition were first order, a mixed phase would exist. After some time, as the system expands, the system becomes dilute and the mean free path increases. A transition occurs from a strongly interacting hadron gas to a weakly interacting hadron gas. Eventually, the inelastic scattering between the particles stop first, therefore the particle ratios become constant. This stage is known as the chemical freeze-out. But still the resonance decay and elastic collisions continue to occur. After some time, the elastic collisions stop and the energy momentum transfer among them stops - this is kinetic freeze-out. ($T_{chem} > T_{kin}$). After that, the particles freely flow and reach the detector.

1.1 Global observables of nucleus-nucleus collision

In our discussion, a collision is called an event. A nuclear collision is characterized by its centrality, number of produced particles, energy density and pressure of the formed state, the freeze-out temperature and volumes etc. One way to study them is to measure the global quantities obtained from the final particles reaching the detectors. Charged particle multiplicity is one of the first observable measured in nucleus nucleus collisions. The differential measurements are done using two quantities called rapidity (y) and transverse momentum (p_T). Rapidity is the relativistic measure of velocty of a particle which is defined by, $y = \frac{1}{2} ln \frac{E+p_z}{E-p_z}$, where E is the total energy and p_z is the longitudinal momentum. At very high energy, $p >> m$, $y = -ln\ tan(\theta/2) = \eta$, where particles are emitted at an angle θ with beam axis and η is the pseudorapidity of the particles. In terms of momentum, $\eta = \frac{1}{2} ln \frac{|p|+p_z}{|p|-p_z}$. Pseudorapidity can be measured easily as θ is a direct measurable quantity. The distribution of particles as a function of rapidity and pseudorapidity is related by the formula, $\frac{dN}{d\eta dp_T} = \sqrt{1 - \frac{m^2}{m_T^2 cosh^2 y}} \frac{dN}{dy dp_T}$. Fig.1.6 (a) shows the pseudorapidity distribution of Pb-Pb collision at 5.02 TeV in ALICE for different centralities. For $y >> 0$, the pseudorapidity distribution and rapidity distribution are almost same, except that for $y \approx 0$, a small dip appears in the $dN/d\eta$ distribution around $\eta \approx 0$ due to mass term which is absent in dN_{ch}/dy distribution. The rapidity of a particle requires mass identification, whereas, pseudorapidity does not require mass identification. For photons, no such dip arises [8]. The peak of the rapidity density is around

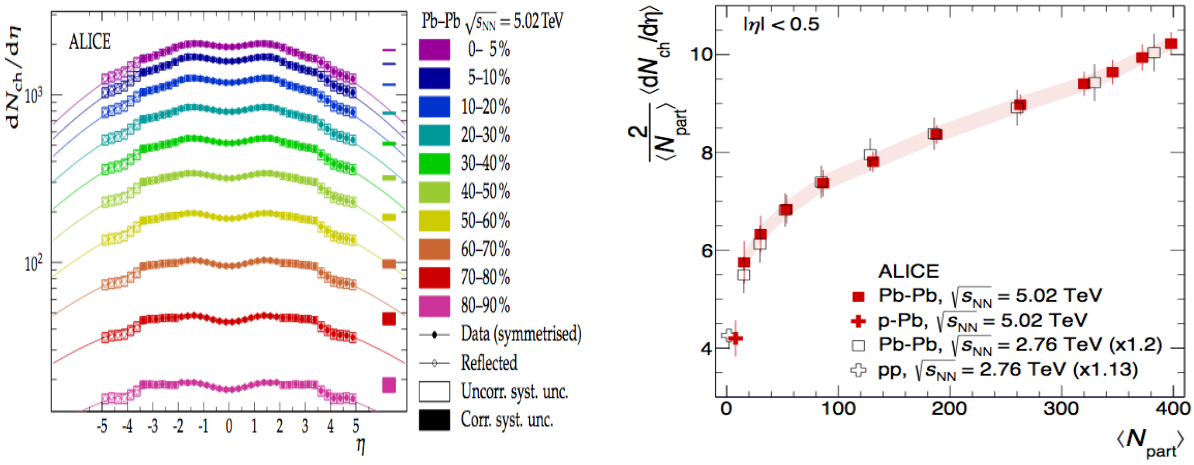

Figure 1.6: Pseudorapidity distribution as a function of centralities (left) and pseudorapidity density as a function of number of participant nucleons (right) in Pb-Pb collision at LHC energies. [24, 25]

mid-rapidity i.e. in the transverse plane around $\theta \approx 90^o$, and the yield decreases as one moves away from the mid-rapidity region. Average number of total charged particles produced in a colli-son can be determined by extrapolating the distribution upto beam rapidity and integrating over the whole range. The pseudorapidity distribution can be used to estimate the Bjorken energy density, $\varepsilon(\tau_0) = \frac{1}{\pi R^2 \tau_0} \frac{dE_T}{d\eta} = \frac{<E>}{\pi R^2 \tau_0} \frac{dN}{d\eta}|_{\eta=0}$, where, the volume of the initially produced collision is considered as a cylinder of length $dz = \tau_0 d\eta$, πR^2 is the longitudinally projected overlap area of the colliding nuclei, dN is the number of particles ,$< E >$ is the average energy per particle and τ_0 is the proper time of thermalization taken as 1 fm/c.

Fig.1.6 (right) shows the event averaged charged-particle density with N_{part} (number of partici-pants). The data at high energy indicates that the multiplicity at mid-rapidity increases faster than N_{part} (number of participants), probably due to the onset of the hard process contributions to particle production [26]. The transverse momentum spectra of charged particles and identified particles provide information about the mean transverse momenta, temperature, radial flow along with other observables [19]. Fig. 1.7 shows the transverse momentum distribution of the charged

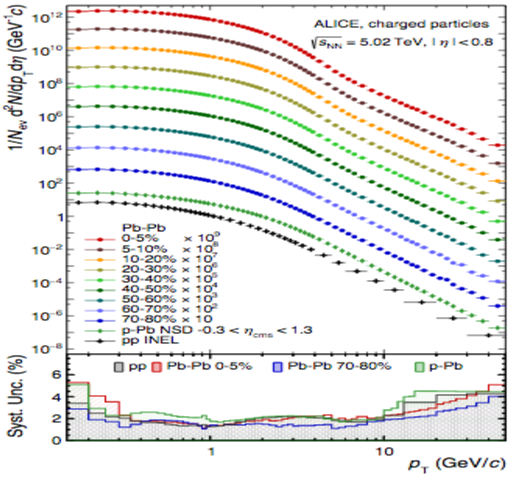

Figure 1.7: Transverse momentum (p_T) spectra of charged hadrons in Pb-Pb collision at $\sqrt{s_{NN}}$ = 5.02 TeV. [27]

particles in Pb-Pb collision at $\sqrt{s_{NN}} = 5.02$ TeV for different centralities. The part of the spectra with low p_T having the thermal origin is described by an exponential function and the high p_T region has power law behaviour having contribution from the fragmentation of hard parton scattering. The entire p_T range is described by a Levy function which has both an exponential part and a power-law function [8]. The inverse slope of the spectra gives the effective temperature that has a thermal origin and has a contribution from the collective flow of particles.

1.2 QGP signals

As discussed earlier, nuclear matters formed in A-A collision thermalize and form a soup of deconfined quarks and gluons called QGP medium which then expands, cools down, and hadronise. Experimentally we cannot observe each stage separately, but can infer only through the final state observables. Each stage of QGP expansion has some specific properties depending on their production mechanism and has corresponding signals that can be used as the evidence of the formation of the QGP matter. A few of such signals have been discussed below.

1.2.1 Collective flow

One of the signals of the collective behaviour of the matter created is the collective flow. In non-central collision, the overlapping zone has an elongated shape. A particle going to a direction where the collision zone is longer has a larger probability to scatter and change its direction than a particle going to the direction having shorter collision zone. Therefore, more particles are in the direction which has the edge of the collision zone nearer. The pressure gradient along the shorter direction between the centre of the system and the vacuum is higher, the flow velocity is also higher there and more particles are emitted in that direction [28]. The evolution of the fireball is governed by the relativistic hydrodynamics and an equation of state. This initial spatial anisotropy of nuclear overlap zone gets converted to the observed momentum anisotropy resulting in asymmetrical particle emission in the perpendicular plane which is expressed by the Fourier expansion of the azimuthal distribution of emitted particles relative to event plane angle Ψ: $E\frac{d^3N}{dp^3} = \frac{d^2N}{2\pi p_T dp_T dy}(1 + 2\sum_{n=1}^{\infty} v_n cos(n(\phi - \psi)))$. The coefficients of expansion are called flow parameters and are defined as, $v_n = \langle cos(n(\phi - \psi_n))\rangle$, ψ is the reaction plane angle. v_1 is directed flow coefficient, v_2 is elliptic flow coefficient and v_3 is triangular flow coefficient [Fig. 1.8]. Since, the reaction plane angle is not a direct observable, the flow coefficients cannot be measured directly. So, it is usually measured by two particle azimuthal correlation, for example, for elliptic flow, it is defined by, $\langle\langle e^{2i(\phi_1-\phi_2)}\rangle\rangle = \langle\langle e^{2i(\phi_1-\psi-(\phi_2-\psi))}\rangle\rangle \approx \langle v_2^2\rangle$. As discussed earlier, the elliptic and the triangular flow are sensitive to initial geometry and its fluctuation. A high value of elliptic flow means the rescattering among the particles is large enough to bring the matter to local thermal equilibrium. As at the beginning of evolution, the spatial anisotropy is highest, therefore, the elliptic flow gives information about the thermalization time scale of the early stage of collision [34]. The earlier the equilibrium, the larger the anisotropies are [14, 32]. The anisotropy coefficients are sensitive to the properties of fluid - its viscosity and equation of state. As the positions of nucleons

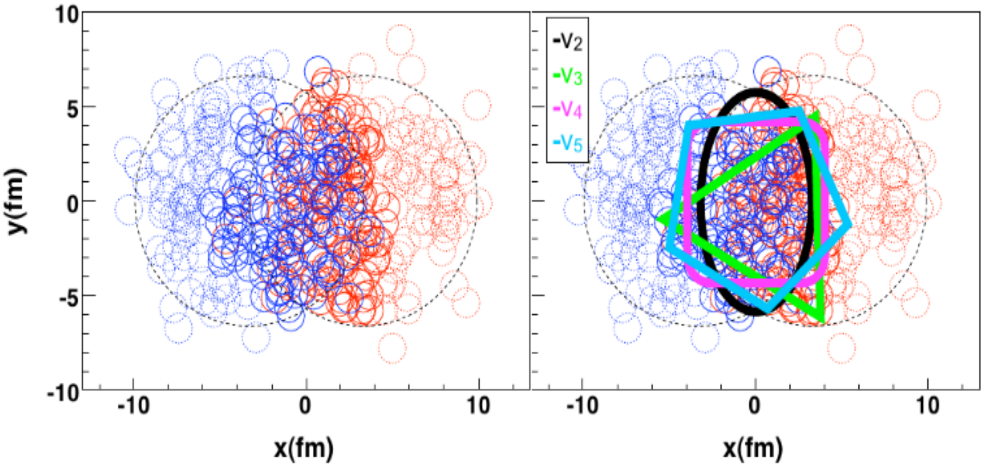

Figure 1.8: Simulation of Pb-Pb collision at $\sqrt{s_{NN}} = 2.76$ TeV with the PHOBOS Glauber Monte Carlo [29].

in nuclei fluctuate, the shape of the initial collision region fluctuates event by event. Thus, v_n also fluctuates event by event. The spatial anisotropy is defined by the eccentricity $\varepsilon = \frac{\langle y^2 - x^2 \rangle}{\langle y^2 + x^2 \rangle}$ where x and y are the positions of the participants [14]. v_n is found to be proportional to the eccentricity ε_n of the initial collision region for small n values [78]. For larger n, v_n is more sensitive to the viscosity of the fluid. Fig. 1.9 shows the time evolution of the interaction zone where the energy density profile is represented by the contours and it shows the evolution of the system from an asymmetric overlap zone to an almost symmetric system. For a given p_T range, elliptic flow decreases with increase in the mass of particle which reflects the effect of mass-dependent radial flow

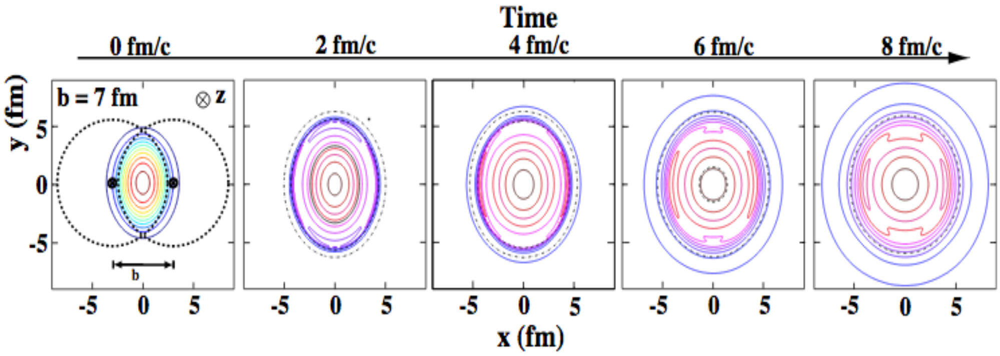

Figure 1.9: Time dependence of the formed initial transverse energy density profile in coordinate space in case of a non-central heavy-ion collision. [32, 14]

on the p_T spectrum of single particle [34] as shown in Fig. 1.10. It is known that, due to the radial flow, the particles get a boost in transverse momentum which depends on the mass of the particle and flow velocity β of the fluid medium. Thus, radial flow shifts the p_T distribution to higher p_T and this effect increases with particle mass and flow velocity. Therefore, the spectrum is depleted at low p_T and this depletion along with the range over which this happens increases with particle mass and flow velocity. Now, in case of elliptic flow $v_2 > 0$, radial velocity is higher in x direction than in y direction, so the depletion also. Therefore, it prevents the excess of particles with p_T along the x direction over the y direction, thereby, reducing the v_2 at low p_T ($p_T < 2$ GeV/c). The p_T range for which this occurs and the amount of the reduction increase with particle mass and radial flow $v_{2,\pi}(p_T) > v_{2,K}(p_T) > v_{2,p}(p_T)$ [34].

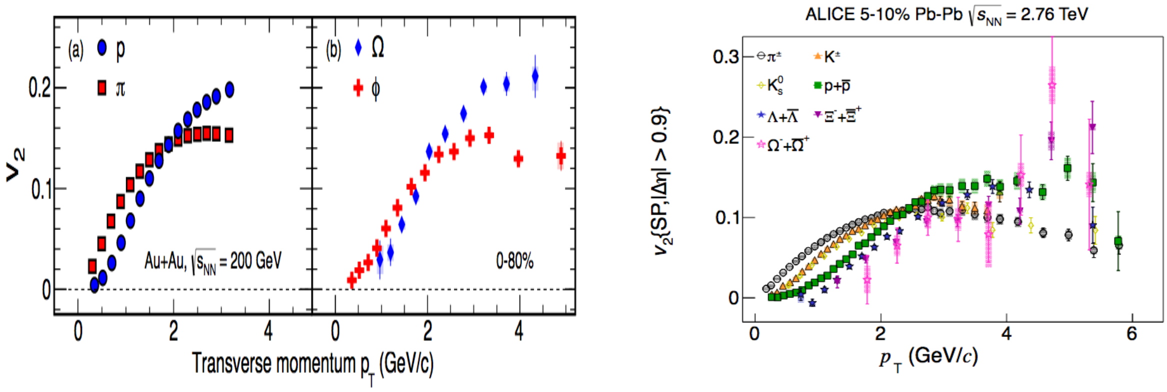

Figure 1.10: The v_2 vs. p_T in minimum bias Au+Au collisions at $\sqrt{s_{NN}} = 200$ GeV for 0-80% centrality for π, p and ϕ, Ω (left panel) [36] and the p_T-differential v_2 for different particle species, forthe 5–10% centrality interval of Pb–Pb collisions at $\sqrt{s_{NN}} = 2.76$ TeV. [37]

At intermediate p_T, $2 < p_T < 5$ GeV/c region, the mass ordering is not observed as shown in Fig. 1.10. v_2 of baryons is higher than that of the mesons in this region. The reason can be explained by assuming the hadronization by the recombination of quarks [30]. The constituent quark number scaling of this observable provides a strong evidence of this quark coalescence [36]. But in LHC, this NCQ scaling is violated for $p_T > 3$ GeV/c [37]. Also, v_2 of ϕ-meson at the intermediate p_T shifts towards baryon instead of mesons. These observations indicates that the possible cause of baryon-meson ordering of v_2 at LHC is due to mass of the particles, not the constituent quark number.

1.2.2 Jet Quenching

High momentum partons are formed at the initial stage of the collision and propagate through the medium. Therefore, they are considered to be the key probes of the QGP medium. The partons from the hard scattering fragments into a collimated shower of particles called Jets [47]. Thus, measurement of Jets can shed light on the propagation through the medium like energy loss mechanism in the medium. The fragments carry fractions of the original parton momentum whose distribution is called fragmentation function. This fragmentation function is modified in A-A collision compared to that in p-p collision due to the presence of medium in A-A collision. Jets are produced back to back on the transverse plane at a separation of 180^o in azimuthal angle carrying equal amount of energy called di-jets. If the scattering happens near the surface of fireball, one parton traverses through the medium and loses energy by interacting with the QGP medium before fragmenting. This is known as Jet quenching which is schematically shown in Fig. 1.11.

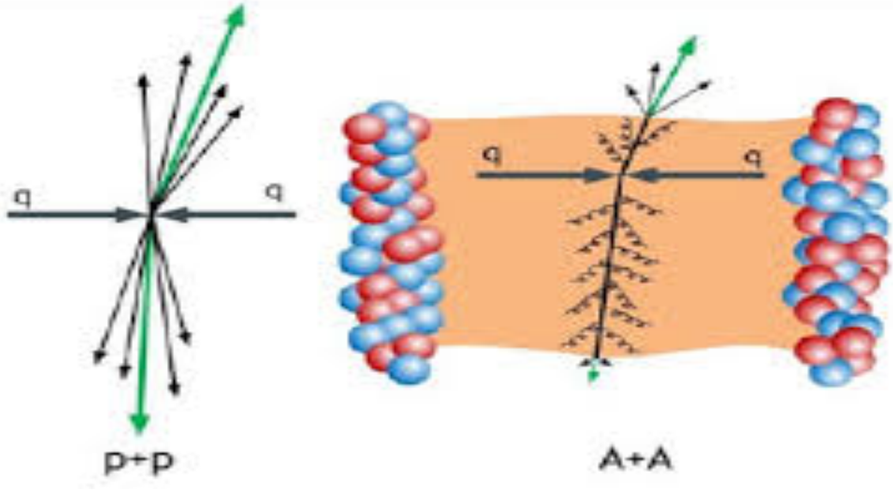

Figure 1.11: Jet-quenching in heavy ion collision. Figure is taken from [50]

This Jet quenching is expressed by the Nuclear Modification factor R_{AA} and defined by, $R_{AA}(p_T) = \frac{d^2N_{AA}/dydp_T}{<N_{coll}>\times d^2N_{pp}/dydp_T}$, where, $< N_{coll} >$ is the average number of binary collisions. This is the measure of the deviation of the yield in A-A collisions compared to the scaled p-p reference as the high p_T particles are suppressed due to the partonic energy-loss in the medium. Any deviation from R_{AA} =1 indicates the presence of medium. Fig. 1.12 shows the suppression of hadrons in central Pb-Pb collisions with respect to peripheral collisions. This suppression of high-p_T hadrons was studied at RHIC using azimuthal correlations between the trigger and associated particles. The presence of a near side peak is the indication of the dominant effect of jet fragmentation in correlation. The back-to-back peaks indicate the fact that the dijets are azimuthally back-to-back. The away-side correlation peak decreases in heavy ion collision due to the suppression [40].

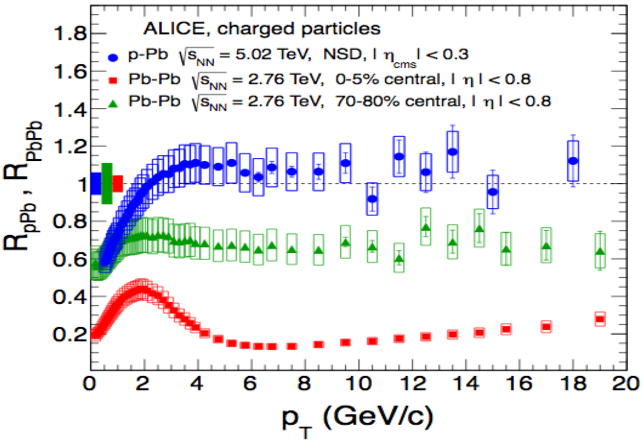

Figure 1.12: The nuclear modification factor of charged particles as a function of transverse momentum [39]

1.2.3 Electromagnetic probe and dileptons

Direct photons and dileptons are useful probes of QGP medium as they are emitted from the whole space time volume carrying the medium property, whereas, hadrons are emitted mostly from the freeze out surface. Also, they interact via electromagnetic and weak processes having large mean free path, therefore they are emitted almost without interacting with the medium. So they carry the undistorted properties of the medium. The direct photons should be separated from the background photons like decay products from neutral pions. There are a few sources of the direct photons - at high p_T, direct photons might come from initial hard collisions and jet fragmentation. The latter can be modified in heavy ion collisions compared to that in the p-p collisions due to the parton energy loss in the medium. At low p_T, direct photons are radiated from the thermalized QGP medium by $q\bar{q}$ annihilation and compton scattering having a thermal origin. Therefore, the spectrum has an exponential nature containing information regarding the initial temperature of the produced medium along with its evolution. An excess of photons is observed in heavy ion collision in the thermal region ($1 < p_T < 4$ GeV/c) compared to that in p-p collisions as shown in Fig. 1.13. But at large p_T, no such enhancement is observed [54, 55]. R_{AA} of direct photons is consistent with unity showing no suppresion [41].

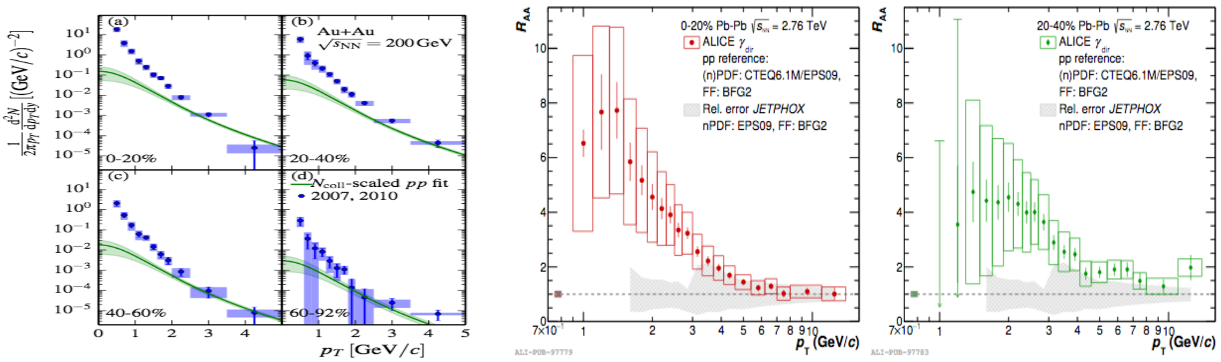

Figure 1.13: (a) Direct photon p_T spectra in AuAu collision for four different centrality bins compared to N_{coll} scaled modified power-law fit to the PHENIX p-p data (b) R_{AA} for two centrality classes in ALICE showing that the direct photon production is enhanced strongly at low p_T over the expected value from p-p collisions scaled with N_{coll} and binary scaling is valid at high p_T. [54, 55]

1.2.4 Heavy quarks as a probe

Charm and Bottom quarks are the heavy quarks that are produced at the early stage of the collision. At a later stage, available energy for particle production decreases, so there is not much energy available to create them. Due to their heavy mass, the possibility of formation of these quarks from thermal bath is also very low. The color charge of the heavy quarks is screened by the presence of quarks and gluons in the medium. Due to the screening, interactions between heavy quarks and anti-quarks are diluted and the probability of forming the bound state (quarkonia) decreases. A strong suppression of the yield of charmonia is observed in heavy ion collisions compared to that in p-p collisions [52, 53] at SPS energy, however the yield increases at higher energy (RHIC and LHC). It is suggested to be due to the regeneration of Charmonia. Bottomonia shows a suppression at LHC energy.

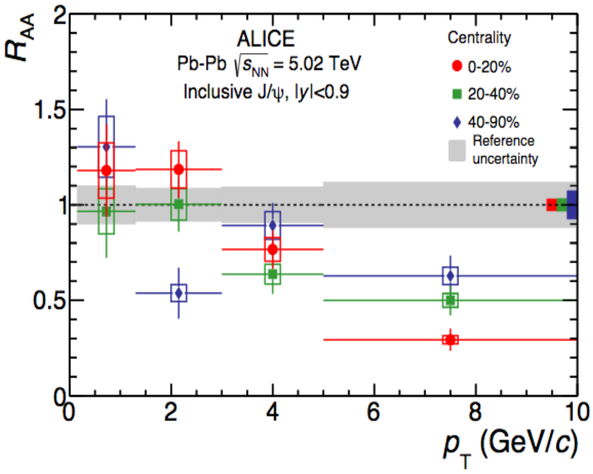

Figure 1.14: Inclusive J/ψ R_{AA} at midrapidity vs. p_T in Pb-Pb collisions at$\sqrt{s_{NN}}$ =5.02 TeV for three centrality intervals [53]

1.2.5 Strangeness enhancement

Strangement enhancement is believed to be a strong signal of QGP [51]. Strange quarks are absent in the initial state as valence quarks unlike up and down, but as they are sufficiently light,they can be abundantly produced in the collisions. In QGP medium, the production of up and down quarks needs more energy than that for the production of strange quarks. Therefore, strange quarks from QGP medium are likely to be produced in heavy ion collision with higher yields than p-p or p-A collisions. Recent study has shown a significant enhancement of the strange to non-strange hadrons with increasing particle multiplicity in p-p collisions at $\sqrt{s_{NN}} = 7$ TeV [56] as well as in p-Pb collisions at $\sqrt{s_{NN}} = 5.02$ TeV as shown in Fig. 1.15. No significant dependence on collision energy is observed at LHC . It implies that the strangeness production is possibly governed by the final state characteristics of instead of the collision energy or the colliding system. The ratios of yields become similar to that observed in Pb–Pb collisions at high multiplicity [56].

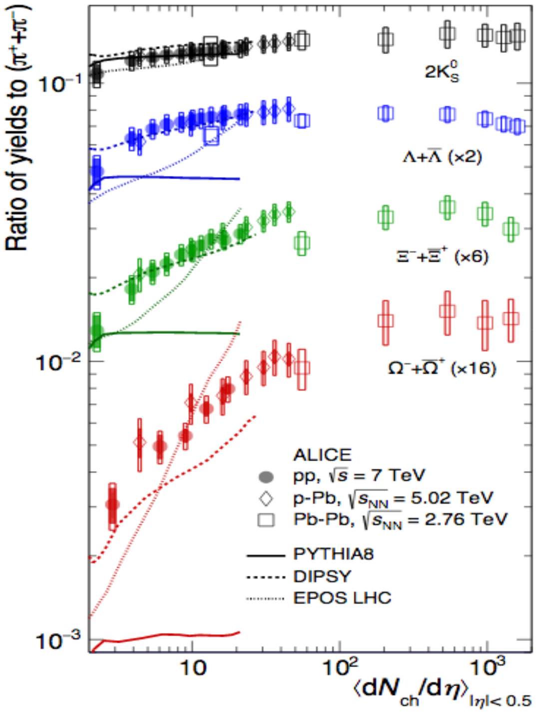

Figure 1.15: p_T-integrated yield ratios of $K_S^0, \lambda, \Xi, \Omega$ to pions $(\pi^+ + \pi^-)$ as a function of $< dN/d\eta >$ measured in mid rapidity [56]

1.2.6 Quark coalescence as an indirect probe of QGP

At the intermediate p_T range (2 to 5 GeV/c), a strong nuclear suppression in the pion yield was observed in central Au + Au collisions in Relativistic Heavy Ion Collider (RHIC) [30], compared to that in p-p collisions [31]. Whereas, similar suppression was not observed in case of protons and Λ's. On the other hand, the p/π ratio exceeds unity for transverse momenta 2 to 5 GeV/c. The p/π ratio and the nuclear modification factors for p-Pb and Pb-Pb systems are shown in Fig. 1.16. The elliptic flow also shows a particle species dependence [36, 58]. It was experimentally established that the observed suppression of the intermediate and high p_T hadrons was due to the energy loss of partons in the hot and dense medium [47] – but it was puzzling why the similar effect was absent in the proton yield. This is known as Baryon Anomaly. It was proposed that hadrons at momenta of a few GeV, where the parton density is high, are produced by recombination of partons, rather than by fragmentation. Now, as long as, the parton spectra is exponential, the recombination dominates fragmentation but fragmentation takes over when the parton spectra takes power law form [30]. In fragmentation formalism, a parton of a certain p_T remains connected with other partons by color strings even after leaving the interaction region which breaks into quark-antiquark pairs to form hadrons finally. One of these hadrons carries a fraction of the

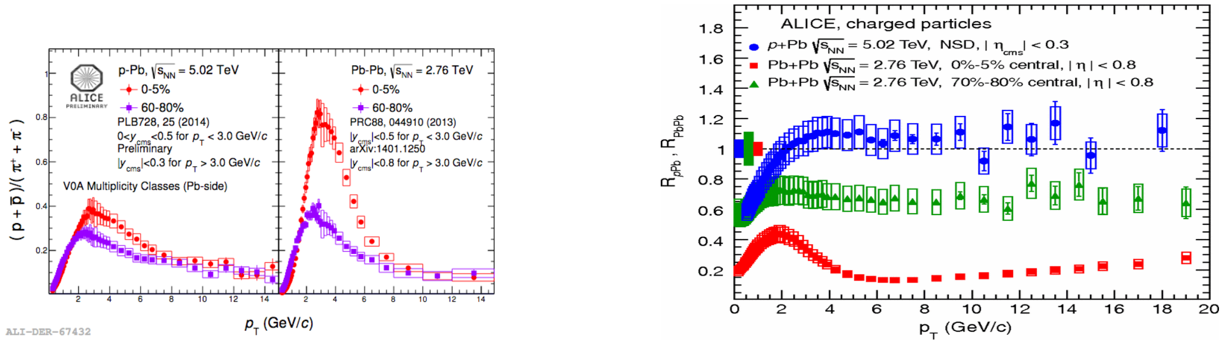

Figure 1.16: p/π ratio with p_T in p+Pb collision at $\sqrt{s_{NN}}$ =5.02 TeV and Pb-Pb collisions at $\sqrt{s_{NN}}$ =2.76 TeV (left). The nuclear modification factor for charged particles with p_T in minimum bias p+Pb collisions with comparison to the central (0-5%) and peripheral (70-80%) Pb-Pb collisions [59, 60]

parent parton p_T, $P_T = zp_T$, where z<1. Therefore, to get a meson of a given momentum P from fragmentation, the parent parton will have a higher momentum p=P/z. For example, average value of z is 0.5 for pion in p-p collision. Therefore, for a pion of 5 GeV/c, a parton of 10 GeV/c will be required which is rare to get because of the steeply falling parton spectrum. Moreover,the parton energy loss further supresses the high p_T partons. On the other hand, in recombination process, for a hadron of momentum P, a parton of momentum P/2 is required, i.e. a 5 GeV/c pion can be produced from the recombination of a quark-antiquark pair each of momentum of 2.5 GeV/c which is far more abundant than 10 GeV/c parton. For this, two such partons have to be close to each other in phase space, that means, the parton density in phase space has to be high so that they can combine. In that case, the hadron momentum will be sum of the momenta of individual partons. It is shown that, the recombination is the main hadronization mechanism and baryon dominates over meson when the parton phase space distribution are described by exponential tail of thermal distributions [30] [Fig. 1.17]. If the phase space density is low,the recombination will be supressed.

The threshold between the two mechanisms depends on the size of the emitting system and the

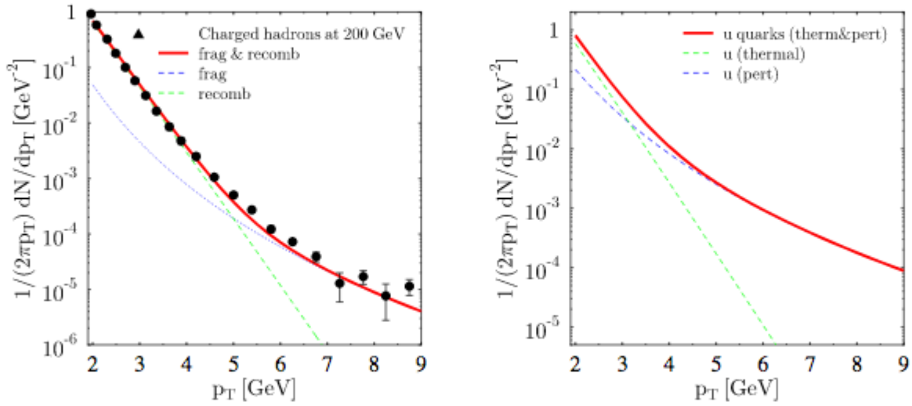

Figure 1.17: Left: the p_T spectra of charged hadrons in Au+Au collisions at $\sqrt{s_{NN}}$ = 200 GeV showing the contributions from recombination (dotted), fragmentation (dashed) and the sum of both (solid line). Right: the p_T spectrum of up quarks. [30]

hadron species. Also, since the recombination is more important for protons than for pions,the nuclear suppression for protons is much less, though there is no sharp cut between two processes. This coalescence mechanism solves the puzzle of baryon-meson enhancement anomaly at intermediate p_T range, the particle species dependence of nuclear suppression factor R_{AA} at intermediate p_T and the observed baryon - meson splitting of $v_2(p_T)$ which basically shows the NCQ scaling [36] as shown in Fig. 1.18. Here, the deviation from scaling is within 10% except pions for which the reason of deviation could be resonance decay and non-flow correlation.

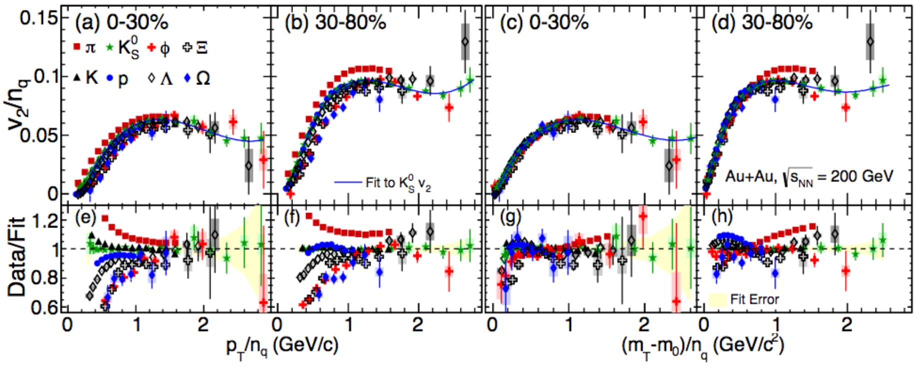

Figure 1.18: v_2/n_q with p_T/n_q and $(m_T - m_0)/n_q$ for identified hadrons in Au + Au collisions at $\sqrt{s_{NN}} = 200$ GeV, n_q is the number of constituent quarks. Ratios of data relative to a polynomial fit to the v_2 of K_S^0 are shown in the lower panels. [36]

1.3 Motivation of this thesis:

As discussed, the recombination mechanism describes quite well the baryon enhancement as well as the particle species dependence of R_{AA} and v_2. On the other hand, the radial flow can also be another reason of the observed baryon meson enhancement as the radial boost from the flowing bulk matter pushes the heavier particles more towards higher p_T. The hydrodynamical model EPOS which includes the strong radial boost and the jet-medium interaction, describes the baryon meson enhancement qualitatively, but it overestimates the magnitude when compared to data. The exact origin of the effect is still under investigation. For many years, at RHIC energies, the baryon meson enhancement and the NCQ scaling at intermediate p_T was believed to be the consequence of quark coalescence which is the dominant mechanism of particle production at intermediate p_T. To validate whether the observed effects are related to particle mass or particle species, ϕ - meson was considered as it has mass similar to that of proton. But it was observed that, ϕ meson exhibits same nature in R_{AA} & v_2 like that of the other lighter mesons. The Λ baryon also shows similar enhancement over K mesons. This implies that the observed effect is not due to mass, it is the constituent quark numbers which plays the primary role. AMPT model with string melting option which has quark coalescence as the particle production mechanism, can reproduce the baryon mson enhancement qualitatively.

However the situation is different at LHC energies. Recently, ALICE experiment has shown that the scaling properties deviate in heavy ion collisions upto almost ±20% for all centrality events for $p_T/n_q > 1$ GeV/c. [37]. Also, the magnitudes of $v_2(p_T)$ are comparable for ϕ meson and

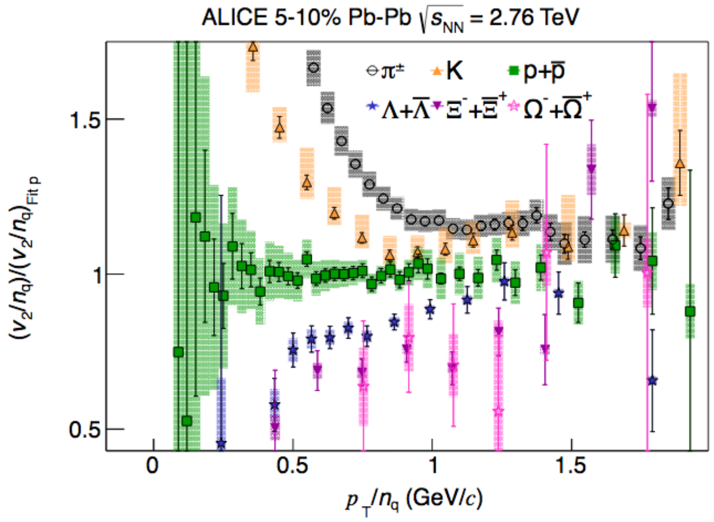

Figure 1.19: The p_T/n_q dependence of the double ratio of v_2/n_q for every particle species relative to a fit to v_2/n_q of p and $\bar{p}$ for the 5–10% Pb-Pb collisions at $\sqrt{s_{NN}}$ =2.76 TeV. [37]

proton at intermediate p_T range. May be, this is the indication that at LHC energies, the particle momentum distribution is determined by mass of the particle, not by the constituent quarks and this contradicts with the coalescence mechanism, however agress with hydrodynamics. Therefore, the observed anomalous enhancement of baryon over meson, particle species dependence of R_{AA} and v_2 at intermediate p_T can be well understood by either quark coalescence or radial flow (Hydrodynamics) - both are soft processes. Though, the particle production via fragmentation occurs at high p_T ($p_T > 6$ GeV/c), however due to the absence of a sharp boundary between the two mechanisms, particle production mechanism at intermediate p_T might have contributions from both hard and soft processes. Apart from that, jet fragmentation functions are altered by the dense medium. This medium modified fragmentation can also be responsible for the baryon enhancement. Jet like peak structure from the correlation measurement of baryon and charged hadrons at intermediate p_T performed at STAR and PHENIX also show an indication of this fact, but still the effect of jet-medium interaction is not known completely [43].

In this thesis, two particle correlations between identified particles as triggers and charged hadrons as associate particles have been studied in Pb-Pb collision at 5.02 TeV in ALICE. Pions and Protons are chosen as trigger particles at intermediate p_T , $2 < p_T < 4$ GeV/c. Two particle correlation is a powerful tool to explore the properties of the hot and dense medium produced in heavy ion collision and the underlying particle production mechanism by studying many aspects of the physics like jet fragmentation and collective effects. Di-hadron angular correlation is important when it is difficult to identify jets on event-by-event basis due to the fluctuating background and also when large quenching effects is there [57]. The per-trigger yield is obtained by constructing the distributions in $\Delta\phi = \phi_{trig} - \phi_{assoc}$ and $\Delta\eta = \eta_{trig}$ - η_{assoc} and is defined by, $C(\Delta\eta, \Delta\phi) = \frac{1}{N_{trig}} \frac{d^2N}{d\Delta\eta d\Delta\phi}$. The particles generated from hard processes are correlated near $\Delta\phi \approx 0$ and $\Delta\phi \approx \pi$ and near $\Delta\eta \approx 0$. So, there will be two peaks at $\Delta\eta, \Delta\phi \approx (0, 0)$ and $\Delta\eta, \Delta\phi \approx (0, \pi)$ while the away side will be suppressed as it traverses through the medium. On the away side $\Delta\phi = \pi$, long range structure extended in $\Delta\eta$ is observed, which represents the correlation from recoiling parton. In heavy ion collisions, apart from the jet-like correlations, a peak around $\Delta\phi = 0$ called the near-side peak is observed extending over a long range in $\Delta\eta$. This long range correlation is called ”ridge” and is expected to be due to the hydrodynamic flow. This is also observed in high multiplicity p-p collisions. The di-hadron correlations has the advantage that, here, it is possible to perform an event-averaged subtraction of the background due to the particles not correlated to the jet.

The intermediate p_T is chosen because it has contribution from both soft and hard processes of particle production. In this study, the correaltion strength is determined by the near side jet-like yield, then comparing the per-triggered yields of pion and proton trigger as a function of centrality can shed light on the particle production mechanism at intermediate p_T. The main goal of this thesis is to understand the origin of the baryon - meson difference through correlation study. Since the triggers at intermediate p_T contain particles from both hard and soft origins and the particles with soft-process origin like quark coalescence or radial flow will not contribute to the jet-like region, so when the correlation function is normalized by the total number of triggers, those soft triggers will suppress the yield towards the central collisions. This suppression will then be particle species dependent since, as already discussed earlier, there is an enhancement of baryons over mesons at intermediate p_T due to the coalescence or radial flow. This suppression is already seen in small system like p-Pb where the medium effect is expected to be less significant [42]. But, in heavy ion collisions like Pb-Pb, apart from these effects, medium effect plays a significant role. Therefore the interaction with medium also contributes to the near side yield in a way not known completely. Understanding this mechanism in data from a competing process is the main aim of the present thesis. The Trigger particles at intermediate p_T range have both hard and soft origin, i.e. $N_{Trigger} = N_{hard} + N_{soft}$, where the first one comes from fragmentation and contributes to jet-like peak, whereas, the latter comes from flow or coalescence and will not have any correlated partner in the near side, they will only contribute to the bulk region. Therefore, when we normalise the correlation function by the number of triggers,

$C(\Delta\eta,\Delta\phi) = \frac{1}{N_{hard}+N_{soft}}\frac{d^2N}{d\Delta\eta d\Delta\phi}$, the soft triggers will cause dilution in per triggered yield. This trigger dilution is observed in small system collision from peripheral to central for proton triggers [42] as shown in Fig. 1.20. The dilution can be directly related to radial flow or quark coalescence, as the medium effect is less significant. In heavy ion collisions, where the jet medium interaction plays an important role, a hint of trigger dilution was observed in AuAu collision at RHIC. There, the near side jet-like yield was estimated for AuAu collisions for both pion and non-pion triggers taking dAu as the reference. Significant differences were reported for pion triggers between the two systems in the per trigger jet-like yield. Whereas, correlations with non-pion triggers showed similar yields for the two systems [43] as shown in Fig. 1.21. The jet-like yield at the intermediate p_T range with pion triggers in central Au+Au collisions is enhanced by almost 24% relative to d+Au. Whereas, yield of non-π triggers are almost same for them. The enhancement of the yield

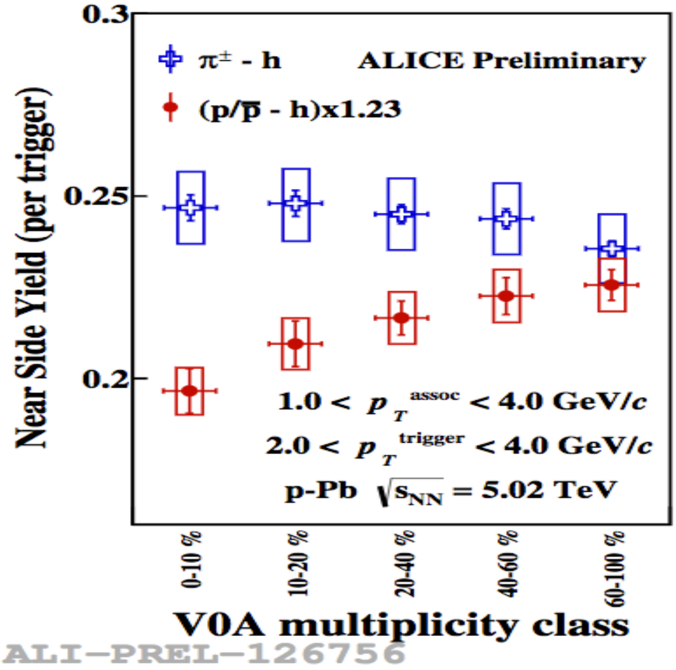

Figure 1.20: Centrality evolution of near side yield for p-Pb collision at 5.02 TeV. [42]

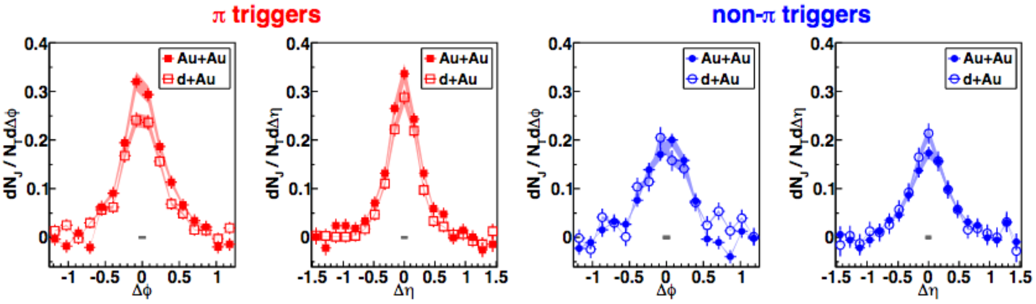

Figure 1.21: Projections of the correlations in $\Delta\phi$ and $\Delta\eta$ for pion triggers (left two panels) and non-pion triggers (right two panels) [43].

with π-triggers might be due to the jet-quenching effect or the modification of the fragmentation functions in AuAu due to presence of medium. Gluon-jets are expected to produce a larger fraction of non-π trigger with respect to π-triggers instead of quark-jets [43, 13, 45, 46] and therefore, a predicted higher energy loss for in-medium gluons should cause larger jet-like yields for non-pion triggers [48]. The particle production from recombination is expected to reduce the yields which would be there from hard processes only like fragmentation. Therefore, the per-trigger yield is diluted and it is expected to be more for baryons at intermediate p_T because of the higher production of baryons over mesons via such mechanism [43]. Thus, the yields associated with the non-pion triggers have the effects of both of these competing process.

The thesis is organized as follows.

In chapter 2, I have discussed the overview of LHC and ALICE experiment, its sub detectors systems and their working principles. In the present work, particle identification is performed using the Time Projection Chamber (TPC) and the Time Of Flight (TOF) detectors. In chapter 3, a detailed study on the multiplicity and pseudorapidity density distributions of charged particles in p-p, p-A and A-A collisions at RHIC and LHC energies has been presented. The production of charged particles over the full kinematic range has been characterized by extrapolating the measured distributions to large η-range through parameterization. Three different ansatze have been used for quantitative descriptions of the shapes of η-distributions in p-p, p-A and A-A collisions in the energy range of few GeV to TeV. An evidence for participant scaling violations in high-energy collisions at the TeV scale has been reported here. One of the preferred ansatze has been used to predict charged particle multiplicity distributions at FAIR and NICA energies. In chapter 4, the experimental data analysis details have been presented. In this chapter, data sets, events and track selection, particle identification, and centrality selection procedures are discussed. Additionally, efficiency, purity estimation and correction, both systematic and statistical uncertainty estimation are also discussed in details in this chapter. In chapter 5, the linear correlation between ε_n and v_n that quantifying the conversion efficiency of the initial spatial eccentricity to the final momentum anisotropy has been performed in heavy ion collisions. The dependence of this correlation on the p_T, collision centrality, and beam energy have been studied for different charged particles using a hydrodynamical model framework. The transverse momentum p_T dependent correlation coefficient shows interesting features which strongly depends on the mass as well as p_T of the emitted particle. The correlation coefficient for both v_2 and v_3 shows mass ordering in the low p_T region and the higher p_T region contributes more to the correlation strength for heavier particles.

Bibliography

[1] H. Fritzsch and M. Gell-Mann, eConf **C720906V2** (1972), 135-165 [arXiv:hep-ph/0208010 [hep-ph]].

[2] M. Riordan and W. A. Zajc, The first few microseconds, Sci. Am. 294N5, 24 (2006) [Spektrum Wiss. 2006 N11, 36 (2006)].

[3] D. J. Schwarz, Annalen Phys. 12, 220 (2003) [astro-ph/0303574].

[4] K. A. Olive, Nucl. Phys. B 190, 483 (1981).

[5] https://j-parc.jp/c/en/facilities/nuclear-and-particle-physics/hadron.html

[6] wikipedia

[7] D. J. Gross and F. Wilczek, Phys. Rev. Lett. **30** (1973), 1343-1346 doi:10.1103/PhysRevLett.30.1343

[8] H. D. Politzer, Phys. Rev. Lett. **30** (1973), 1346-1349 doi:10.1103/PhysRevLett.30.1346

[9] J. C. Collins and M. J. Perry, Phys. Rev. Lett. **34** (1975), 1353 doi:10.1103/PhysRevLett.34.1353

[10] E. V. Shuryak, Sov. J. Nucl. Phys. **28** (1978), 408 doi:10.1016/0370-2693(78)90370-2

[11] F. Karsch, Lect. Notes Phys. **583** (2002), 209-249 doi:10.1007/3-540-45792-5_6 [arXiv:hep-lat/0106019 [hep-lat]].

[12] T. Nayak and B. Sinha, doi:10.1007/978-81-8489-295-6_9 [arXiv:0904.3428 [nucl-ex]].

[13] O. Philipsen, arXiv:0808.0672v1 [hep-ph]

[14] S. Gupta, J. Phys. G: Nucl. Part. Phys. 35 (2008) 104018.

[15] F. Karsch, E. Laermann and A. Peikert Nucl. Phys. B605 (2001) 579.

[16] Y. Aoki, Z. Fodor, S. D. Katz and K. K. Szabo, Phys. Lett. B **643** (2006), 46-54 doi:10.1016/j.physletb.2006.10.021 [arXiv:hep-lat/0609068 [hep-lat]].

[17] Y. Aoki, G. Endrodi, Z. Fodor, S. D. Katz and K. K. Szabo, Nature **443** (2006), 675-678 doi:10.1038/nature05120 [arXiv:hep-lat/0611014 [hep-lat]].

[18] S. Ejiri, Phys. Rev. D **78** (2008), 074507 doi:10.1103/PhysRevD.78.074507 [arXiv:0804.3227 [hep-lat]].

[19] N. Armesto et al., e-Print: arXiv:0711.0974.

[20] Bicudo, Pedro & Cardoso, M. & Cardoso, Nuno. (2011). QCD confinement and chiral crossovers, two critical points.

[21] H. Wang, [arXiv:1304.2073 [nucl-ex]].

[22] M. Kliemant, R. Sahoo, T. Schuster and R. Stock, Lect. Notes Phys. **785** (2010), 23-103 doi:10.1007/978-3-642-02286-9_2 [arXiv:0809.2482 [nucl-ex]].

[23] Phases of nuclear matter https://pdfs.semanticscholar.org/246d/d4028e86528e4d27ba40f79838a100f85287.pdf

[24] J. Adam *et al.* [ALICE], Phys. Lett. B **772** (2017), 567-577 doi:10.1016/j.physletb.2017.07.017

[25] J. Adam *et al.* [ALICE], Phys. Rev. Lett. **116** (2016) no.22, 222302 doi:10.1103/PhysRevLett.116.222302

[26] Roland, G.; Safarik, K.; Steinberg, P. Heavy-ion collisions at the LHC.Prog. Part. Nucl. Phys.2014,77, 70–127

[27] S. Acharya *et al.* [ALICE], JHEP **11** (2018), 013 doi:10.1007/JHEP11(2018)013

[28] P Huovinen 2017 J. Phys.: Conf. Ser.798 012063

[29] B. Alver, M. Baker, C. Loizides and P. Steinberg, [arXiv:0805.4411 [nucl-ex]].

[30] R. J. Fries, B. Muller, C. Nonaka and S. A. Bass, J. Phys. G **30** (2004), S223-S228 doi:10.1088/0954-3899/30/1/025

[31] K. Adcoxet al.[PHENIX], Phys. Rev. Lett.88, 022301 (2002); C. Adleret al.[STAR],nucl-ex/0210033

[32] R. Snellings, New J. Phys. **13** (2011), 055008 doi:10.1088/1367-2630/13/5/055008 [arXiv:1102.3010 [nucl-ex]].

[33] P. F. Kolb and U. W. Heinz, [arXiv:nucl-th/0305084 [nucl-th]].

[34] P. Huovinen, P. F. Kolb, U. W. Heinz, P. V. Ruuskanen and S. A. Voloshin, Phys. Lett. B **503** (2001), 58-64 doi:10.1016/S0370-2693(01)00219-2

[35] H. Niemi, G. S. Denicol, H. Holopainen and P. Huovinen, Phys. Rev. C **87** (2013) no.5, 054901 doi:10.1103/PhysRevC.87.054901

[36] L. Adamczyk *et al.* [STAR], Phys. Rev. Lett. **116** (2016) no.6, 062301 doi:10.1103/PhysRevLett.116.062301 [arXiv:1507.05247 [nucl-ex]].

[37] B. B. Abelev *et al.* [ALICE], JHEP **06** (2015), 190 doi:10.1007/JHEP06(2015)190 [arXiv:1405.4632 [nucl-ex]].

[38] Radial and elliptic flow at RHIC: further predictions.P. Huovinenet al., Phys. Lett.B 503, 58 (2001).

[39] B. Abelev *et al.* [ALICE], Phys. Rev. Lett. **110** (2013) no.8, 082302 doi:10.1103/PhysRevLett.110.082302

[40] J. Adams *et al.* [STAR], Phys. Rev. Lett. **97** (2006), 162301

[41] S. Afanasiev *et al.* [PHENIX], Phys. Rev. Lett. **109** (2012), 152302 doi:10.1103/PhysRevLett.109.152302

[42] Analysis note of Debojit Sarkar, https://alice-notes.web.cern.ch/node/287

[43] L. Adamczyk *et al.* [STAR], Phys. Lett. B **751** (2015), 233-240 doi:10.1016/j.physletb.2015.10.037 [arXiv:1410.3524 [nucl-ex]].

[44] J. Adams et al.(STAR Collaboration), arXiv:nucl-ex/0601042 [nucl-ex]; Phys. Lett. B637, 161 (2006).

[45] S. Albino, B. Kniehl, and G. Kramer, Nucl. Phys. B725, 181 (2005).

[46] B. Mohanty (STAR Collaboration), inProceedings ofthe 23rd Winter Workshop on Nuclear Dynamics(2007)arXiv:0705.0953

[47] C. Adler *et al.* [STAR], Phys. Rev. Lett. **89** (2002), 202301 doi:10.1103/PhysRevLett.89.202301

[48] X.-N. Wang, Phys. Rev. C58, 2321 (1998); Q. Wang andX.-N. Wang, Phys. Rev. C71, 014903

(2005); S. Wicks,W. Horowitz, M. Djordjevic, and M. Gyulassy, Nucl.Phys. A784, 426 (2007);N. Armesto, A. Dainese,C. A. Salgado, and U. A. Wiedemann, Phys. Rev. D71, 054027 (2005).

[49] R. J. Fries, Nucl. Phys. A783, 125 (2007); R. C. Hwa,arXiv:0904.2159 [nucl-th]

[50] https://lphe.epfl.ch/seminar/extern/Marta_Verweij_02052016.pdf

[51] J. Rafelski and B. Muller, Phys. Rev. Lett. **48** (1982), 1066 [erratum: Phys. Rev. Lett. **56** (1986), 2334] doi:10.1103/PhysRevLett.48.1066

[52] T. Matsui and H. Satz, Phys. Lett. B **178** (1986), 416-422 doi:10.1016/0370-2693(86)91404-8

[53] S. Acharya *et al.* [ALICE], Phys. Lett. B **805** (2020), 135434 doi:10.1016/j.physletb.2020.135434

[54] J. Adam *et al.* [ALICE], Phys. Lett. B **754** (2016), 235-248 doi:10.1016/j.physletb.2016.01.020 [arXiv:1509.07324 [nucl-ex]].

[55] A. Adare *et al.* [PHENIX], Phys. Rev. C **91** (2015) no.6, 064904 doi:10.1103/PhysRevC.91.064904 [arXiv:1405.3940 [nucl-ex]].

[56] J. Adam *et al.* [ALICE], Nature Phys. **13** (2017), 535-539 doi:10.1038/nphys4111 [arXiv:1606.07424 [nucl-ex]].

[57] A. Ohlson [ALICE], J. Phys. Conf. Ser. **668** (2016) no.1, 012074 doi:10.1088/1742-6596/668/1/012074 [arXiv:1509.05889 [nucl-ex]].

[58] P. Sorensen [STAR], J. Phys. G **30** (2004), S217-S222 doi:10.1088/0954-3899/30/1/024 [arXiv:nucl-ex/0305008 [nucl-ex]].

[59] A. Ortiz Velasquez [BNL-Bielefeld-CCNU], Nucl. Phys. A **932** (2014), 146-151 doi:10.1016/j.nuclphysa.2014.07.034

[60] B. Abelev *et al.* [ALICE], Phys. Rev. Lett. **110** (2013) no.8, 082302 doi:10.1103/PhysRevLett.110.082302 [arXiv:1210.4520 [nucl-ex]].

Chapter 2

A Large Ion Collider Experiment(ALICE)

2.1 Large Hadron Collider(LHC)

The accelerator complex at CERN consists of a series of machines providing increasingly higher particle energies [1, 3, 4] as shown in Fig. 2.1. Each machine accelerates the beam particles to a certain energy and injects into the next one, which further increases the beam energy to a higher value and injects it to next one and so on. LHC, the last machine of this chain, can accelerate proton beam up to the centre of mass energy ($\sqrt{s_{NN}}$) of 13 TeV and heavy ions up to $\sqrt{s_{NN}}$= 5.44 TeV. As an example, electrons are stripped from the hydrogen atoms to obtain protons which are then fed to the PS Booster at an energy of 50 MeV. These are then accelerated to 1.4 GeV and injected to the Proton Synchrotron (PS). They are subsequently accelerated to 25 GeV and then fed to the Super Proton Synchrotron (SPS) where they gain 450 GeV after being accelerated and finally sent to the LHC where they are accelerated to TeV energy. The stored beams circulate for many hours in the beam pipes. Similarly, lead ions are also accelerated to the design value of

$\sqrt{s_{NN}}$ =5.7 TeV energy. The Large Hadron Collider is of 27 km circumference that accelerates hadrons to the desired energy. In LHC, two beams which are circulating in opposite directions are made to collide at four interaction points i.e. the intersecting points of the two rings - they are ALICE, ATLAS, CMS and LHCb. Three more smaller experiments also joined the quest- TOTEM next to CMS, LHCf next to ATLAS and MoEDAL next to LHCb [1].

In circular accelerators, the energy loss per turn by synchrotron radiation is inversely proportional to the fourth power of mass of the particle, hence it is more effective to accelerate massive particles to obtain higher energy collisions than the lighter ones. The tunnel is built at a mean depth of 100 m from the consideration of cost, impact on landscape and good shielding for radiation by the earth crust.

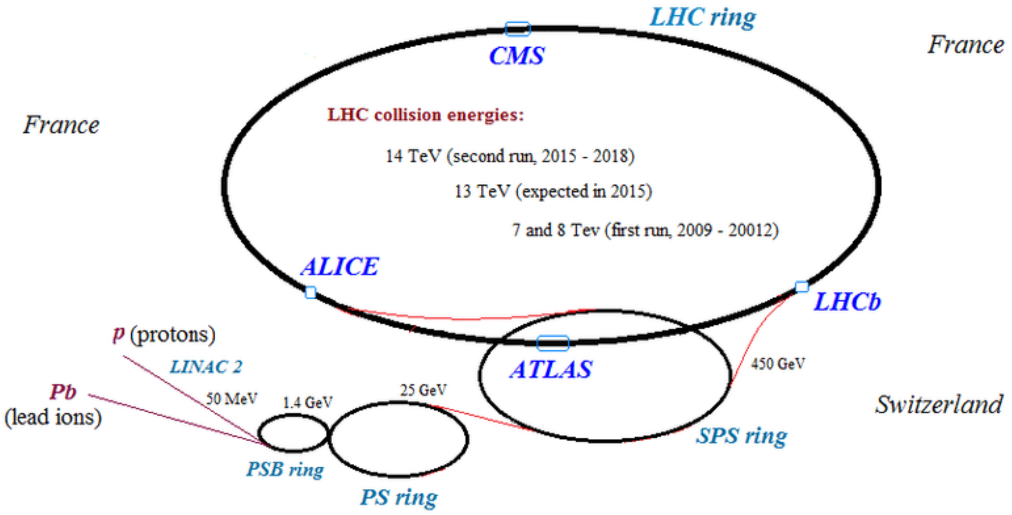

Figure 2.1: LHC accelerator complex [1]

The goal of LHC through proton-proton collision is primarily to produce and study the details of Higgs boson which is responsible for the mass of the elementary particles. Other topics include understanding of the supersymmetry, dark matter and dark energy, and the heavy ion collisions at LHC which helps to shed light on the matter existed in micro-second old universe called Quark-Gluon-Plasma.

The Universe, created from the Big Bang, went through a phase during which the matter was extremely hot and dense and composed of quark and gluons - called ”Quark-Gluon-Plasma”. As the Universe cooled, the quarks are combined to form hadrons. This phenomenon is called the hadronization of quarks. The LHC produces QGP by colliding two beams of heavy ions at extremely high energy. Finally, the hadrons produced at the LHC collisions reach the detectors and can be detected to study the properties of QGP through the particles.

The LHC consists of arcs that contain dipole magnets to move the particles in nearly circular orbits by bending them, quadrupole magnets to focus the beam and RF cavities to accelerate particles and keep them at a constant energy by compensating for energy losses. The vacuum pressure is 10^{-13} atm to avoid collisions with gas molecules. The particles circulate in the LHC ring in bunches. The bunches get squeezed to few mm or μm as they approach the interaction points to increase the collision probability and are expanded to few centimetres long and a millimetre wide when they are far from a collision point.

2.1.1 Beam parameters

Apart from energy, the reaction rate of a process depends on the instantaneous luminosity (L) which is defined as, $R = L \times \sigma$ where R is the event rate and σ is the interaction cross-section of a process. L depends on the number of particles in each bunch, the frequency of complete revolution, the number of bunches and the beam cross-section. To increase the collision rate, bunch size is squeezed to few μm near the collision point [15]. Luminosity in a machine can be increased by increasing the number of bunches. The bunch spacing in LHC is 25 nsec at the full design luminosity. Each beam consists of nearly 3000 bunches of particles and each bunch contains as many as 100 billion particles. When the bunches cross each other, there are up to 40 collisions between 200 billion particles. Bunches cross on an average of about 30 million times per second, so the LHC generates about 1 billion particle collisions per second [1]. A stored beam might circulate for more than 10 hours. The target luminosity for the ALICE p-p data taking is typically from L $\approx 10^{29}$ s^{-1} cm^{-2} to L$\approx 10^{31}$ s^{-1} cm^{-2}. The average number of interactions per bunch crossing (μ) is between 0.05 to 0.3. In 2010 and 2011 with Pb ions, ALICE took data at the highest achievable luminosity of the order 10^{25} $s^{-1}cm^{-2}$ in 2010 and 10^{26} $s^{-1}cm^{-2}$ in 2011. For p-p collisions, the design luminosity of LHC is of the order of 10^{34} $s^{-1}cm^{-2}$ but ALICE operates at around $10^{30}s^{-1}cm^{-2}$.

2.2 ALICE detectors

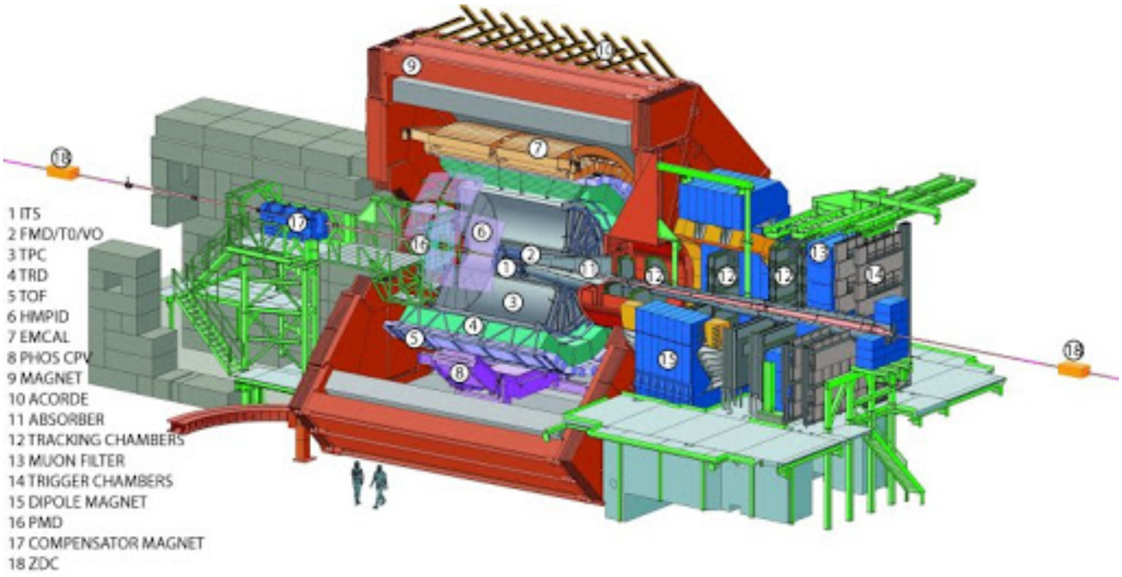

Figure 2.2: Schematic layout of ALICE detectors [2]

ALICE is an experiment placed at an intersection point of LHC to study the formation and the properties of Quark-Gluon Plasma, a state of matter where quarks and gluons, under conditions of very high temperatures and energy densities, are not confined inside the hadrons. Such a state is predicted to have existed a micro-second after the Big Bang, before particles like protons and neutrons were formed. It probes such a state by analyzing the particles formed in such collisions by studying their identity and 4-momentum as far as practicable. To achieve this, it consists of several sub-detectors as shown in Fig. 2.2. ALICE collects data with the collisions of proton-proton, proton-lead, lead-lead, Xe-Xe at $\sqrt{s_{NN}}$ upto a few TeV. The weight of the ALICE experiment is about 10000 tonnes and size is about 26 m × 16 m × 16 m. ALICE can measure particles of momentum 100 MeV/c to 10 GeV/c. The sub-systems of ALICE have been described in the subsequent section.

2.3 The Central Barrel Detectors

The central part of ALICE contains Inner Tracking System (ITS), Time Projection Chamber (TPC), Transition Radiation Detector (TRD), Time Of Flight (TOF), PHOton Spectrometer (PHOS), Electromagnetic Calorimeter (EMCal) and High Momentum Particle Identification Detector (HMPID) all at the mid-rapidity region. ITS, TPC, TRD and TOF have full azimuthal coverage at mid rapidity ($|\eta| < 0.9$), the rest of the detectors are of limited coverage.

2.3.1 Inner Tracking System (ITS)

ITS is closest to the collision point where the track density is very high, up to 90 / cm^2, so high granularity Si-pixels are used in the inner most layers to provide very good position and momentum resolution. ITS is designed for about 8000 tracks per unit rapidity. The spatial resolution of ITS is of the order of a few tens of μm [5]. Layout of ITS detector is shown in Fig. 2.3. The primary functions of ITS are :

- primary vertex reconstruction using the first two layers of ITS.
- secondary vertex finding for hyperons, B,D mesons
- particle identification of low momentum particles via energy loss measurement (< 1 GeV) using the next four layers

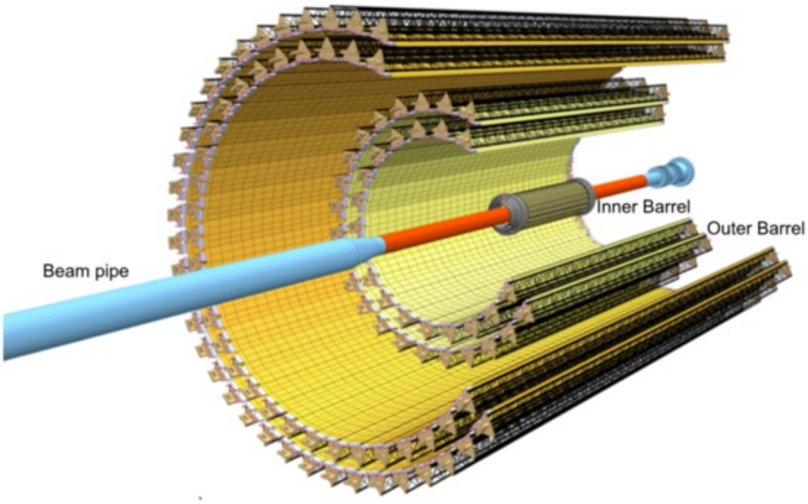

Figure 2.3: Layout of the ITS detector of ALICE [6]

- tracking and standalone reconstruction of low p_T particles
- improvement of momentum resolution of TPC tracks, providing good position as well as energy momentum resolution .

ITS has six cylindrical layers of silicon detectors - two Silicon Pixel Detector (SPD), two Silicon Drift Detectors (SDD) and two Silicon Strip Detectors (SSD). Except the two innermost SPD, all the layers have analog readout to identify particles via energy loss measurement. The low momentum particles can be detected by ITS only. The first ITS layer SPD has a wider coverage of $|\eta| < 1.75$, while the other layers SDD and SSD have $|\eta| < 0.9$.

Silicon Pixel Detector: It is placed at radius R =3.9cm to 7.6 cm. It has high granularity with maximum spatial resolution of 12 μm in r-ϕ and 100 μm in the z-direction. SPD helps in precise primary vertex measurement and secondary vertex reconstruction.

Silicon Drift Detector: The two middle layers of ITS are SDD with radius R =14.9cm to 23.8 cm from beam pipe. This is used for particle identification using specific energy loss (dE/dx) and tracking of the tracks passing through it. It uses drift time of electrons to find the position of track hits and the z-position of the hits are determined from the centroid of the charge accumulated in the anodes. It has position resolution of 38 μm in r-ϕ and 28 μm in Z.

Silicon Strip Detector: These are the last two layers of ITS used for particle identification and tracking. It is placed at radius R =38.5cm and 43.6 cm respectively. It has spatial resolution of 20 μm in r-ϕ and 830 μm in Z. This layer is important for TPC-ITS track matching.

Performance of ITS:

Primary vertex reconstruction: The high particle density in SPD is beneficial to determine the vertex position. By combining the hits in the two pixel layers, the z-coordinate of the vertex is found with a precision of about 10 μm though it becomes worse at lower multiplicity. For p-p collisions it is around 90 μm. The interaction vertex is a space point to which maximum number of tracklets converge. Each cluster on layer 1 is associated to all clusters on layer 2 of SPD within a window $\delta\phi < 0.5$ rad by a line in z,r. This is called tracklets. At $r = 0$, DCA between the tracklet and nominal beam position is calculated for all such tracklets. The position of the maximum in the z-distribution of DCA is considered as the preliminary vertex. (x,y) position of vertex is determined from the centre of beam spot averaged over many events and the resolution is given by the size of the beam spot. If N tracklets are used, vertex resolution $\propto 1/\sqrt{N}$, N $\propto dN_{ch}/d\eta$.

Tracking: The track finding for TPC and ITS is done using Kalman filter algorithm. Track seeds are built using the TPC clusters and the preliminary vertex at the outer radius of TPC. The seeds are propagated inward and at each step, nearest found clusters are associated to them. Only the tracks built from $>$ 20 clusters in the outer volume are propagated to the inner TPC region. The reconstructed TPC tracks (based on maximum 159 points) are extrapolated to the ITS outermost layer and become its seed. The seeds are then propagated inward and updated at each ITS layer similar as TPC. Reconstruction efficiency in TPC for low p_T particles is very poor. To recover them, Standalone ITS reconstruction is done with the clusters leftover by TPC+ITS. Tracks reconstructed in ITS are extrapolated to their point of closest approach to the preliminary determined vertex. Now the tracks are propagated outward using the clusters found at previous stage. Tracks reaching TOF are matched with the TOF clusters. Similarly track matching is performed with TRD, EMCal, PHOS, HMPID and re-fitted. Also, the time of flight expected for different particles are updated for particle identification with TOF.Again the tracks are propagated inwards and re-fitted : track's position, direction, curvature etc. are determined.

The reconstructed tracks in TPC and ITS are used to find the vertex more precisely than SPD tracklets alone. The tracks reconstructed in TPC and ITS are extrapolated to the point of closest approach to the nominal beam line and far outliers are removed. Thus the precise vertex is determined.

Secondary vertex reconstruction: Tracks with DCA (which is the closest distance of the track from vertex) to the interaction vertex > some value are selected. For each unlike-sign pair of such tracks, PCA (point of closest approach of the two tracks) between the two tracks is calculated.

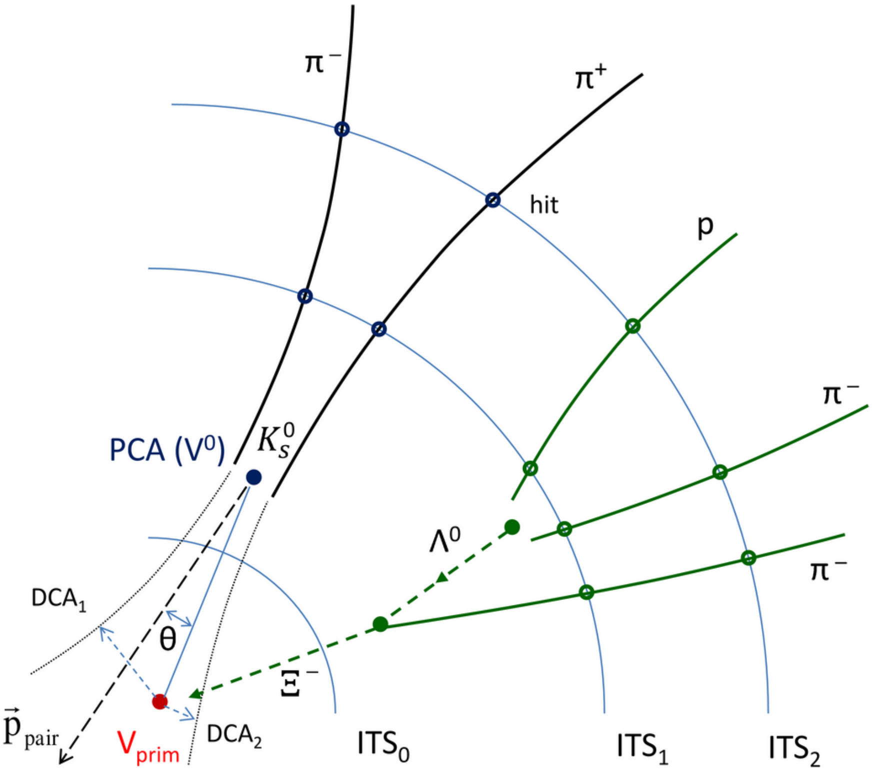

Figure 2.4: Secondary vertex determination [15]

Then the following cuts are used: 1. Distance between two tracks at PCA < 1.5 cm, 2. PCA should be closer to the interaction vertex than the innermost hit of either of the two tracks. 3. $cos\theta$ between the total momentum vector of the track pair and the line connecting the primary and secondary vertices > 0.9. The secondary vertex reconstruction is schematically given in Fig. 2.4.

Particle identification: ITS allows hadron separation below 100 MeV/c. dE/dx is measured from the analog readout of electronic signal produced in SDD and SSD. Good π-K separation upto 0.5 GeV/c and good π-p and p-K separation upto 1 GeV/c are performed.

ITS SPD is also used to determine centrality in p-p and p-A collision.

2.3.2 Time Projection Chamber (TPC)

TPC is the main tracking detector in ALICE surrounding ITS [7] [Fig. 2.5]. It does charged particle momentum measurement, particle identification and vertexing together with ITS, TOF and TRD with good momentum resolution, two track separation and dE/dx resolution for $p_T < 10$ GeV/c in mid-rapidity region. The inner and outer radius of TPC are about 80 cm and 250 cm respectively and the overall length in the beam direction of 500 cm. TPC provides a large volume of 88 m^3 filled with a gas of 90% Ne, 10% CO_2 and N_2 in Run1, Ar+CO_2 in Run2 (Pb-Pb interaction rate >10 kHz) and Ne+CO_2+N_2 in Run3. In Run3, MWPC readout pads will be replaced by the GEM chamber and Pb-Pb interaction rate up to 50 kHz will be achieved. Choice of gas mixture is optimized to ensure good momentum resolution, high rate handling capacity, low space charge effect and low scattering. Since the medium is gaseous, there is a low multiple scattering due to large radiation length. TPC is divided into two regions with an High Voltage (100 kV) electrode at its axial centre providing uniform axial electric field of 400 V/cm. The charged particles going through the gas volume ionises the gas and liberates electrons which drift towards the readout

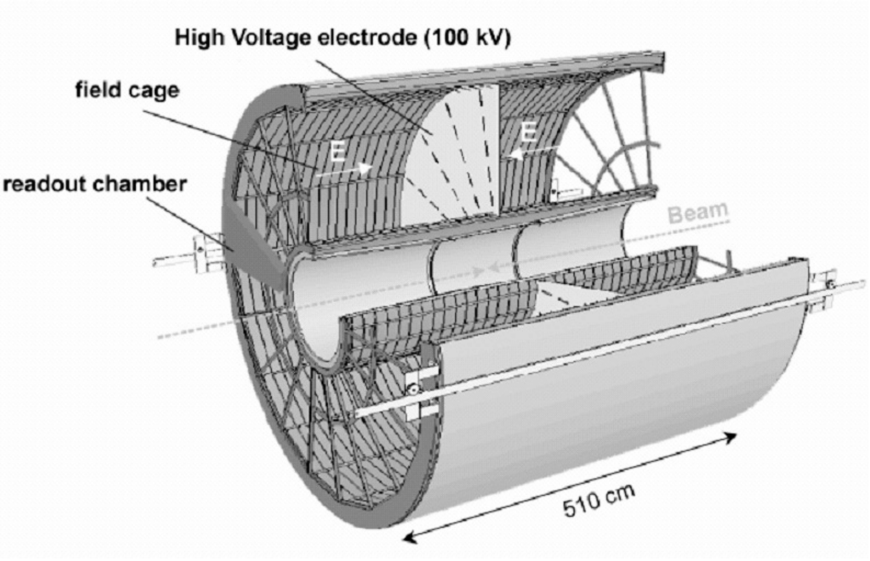

Figure 2.5: ALICE Time Projection chamber [8]

plates with drift velocity ≈ 2.7 cm/s and hit the readout pads. Depending on the charge and momentum, the particles bend in either direction. The readout of the signal is done by the 570132 pads of the multiwire proportional chambers (MWPC) located at the TPC end plates. A track of a particle can have up to 159 clusters in the TPC volume as there are 159 pad rows. Under the action of electric field and magnetic field (0.5 T), a particle moves in a helical path. From the radius of curvature and magnetic field, the momentum of the particle is determined. The (x,y) position is determined by the hit in MWPC at the end plates and z coordinate is measured from the arrival time of the signal with respect to collision time of the beams. The position resolution of the detector is about 800-1100 μm in the r-ϕ plane and 1100-1250 μm in the z-direction. The specific energy loss dE/dx is measured by the charge collected from readout pads. Knowing the particle momentum and $< dE/dx >$, the particle identity can be found from the Bethe-Bloch formula as shown in Fig. 2.6. TPC can separate the particles well upto p_T=1 GeV/c using dE/dx measuremt.The momentum resolution varies from 2% to 20% for tracks of p_T of 100 MeV/c to 100 GeV/c for TPC alone and with other detectors, TPC provides better momentum resolution up to 10% for tracks up to 100 GeV/c . For good dE/dx resolution, particle identification is possible down to 0.3 GeV/c.

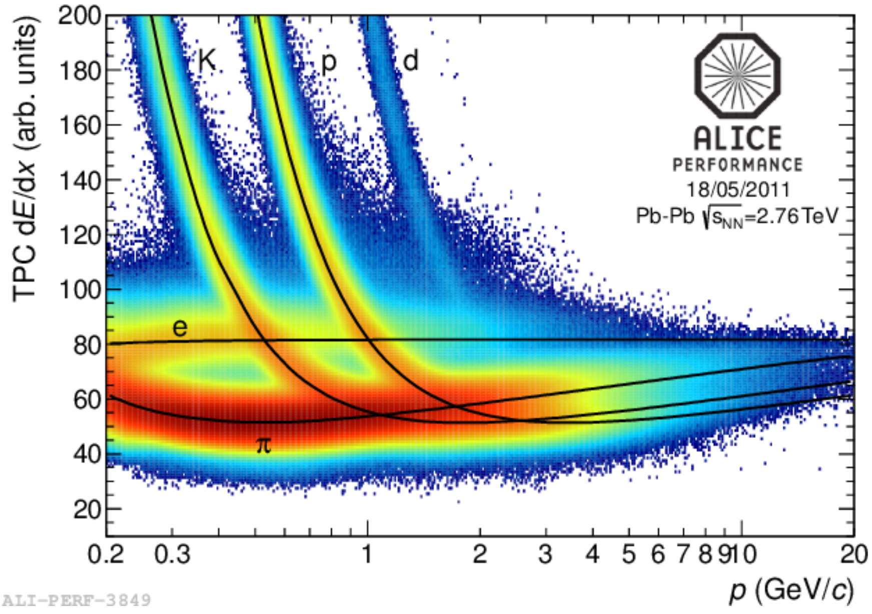

Figure 2.6: Particle Identification using energy loss [15]

2.3.3 Time Of Flight (TOF)

The TOF in ALICE is used for particle Identification up to higher p_T (> 1 GeV/c) range than that by TPC by measuring the particle velocity from their time of flight measurement [9, 10]. To measure time of flight, it needs a start time t_0 and a stop time t. Therefore, the velocity of the particle is given by, v= l/(t-t_0) or β = l/c(t-t_0) , l is the known track length. Knowing the momentum p of the particle from TPC, one can determine its mass and thus one can identify the particle by :$m = p\sqrt{\frac{t^2}{l^2} - 1} = p\sqrt{\frac{1}{\beta^2} - 1}$, t is the time of flight. The start time is provided by T0 detector or it can be estimated using the particle arrival times at the TOF detector. TOF provides PID upto 2.5 GeV/c for pion and kaon, and upto 4 GeV/c for protons which TPC alone cannot do. TOF in ALICE is a large area Multi-gap Resistive Plate Chamber located just around TRD. Gas detector is the only choice to cover a large area of about 141 m^2. The mass resolution has three contributions: $\delta m/m = \delta p/p, \delta m/m = (E/m)^2\delta l/l$, and $\delta m/m = (E/m)^2\delta t/t$. For large momentum, only the errors in time of flight and track length dominate. Therefore, the time resolution must be good. The MRPC used here has a time resolution ≈ 80 ps , better than that of the Scintillators (≈100 ps). Fig 2.7 shows the distribution of β with momentum. The number of standard deviation in time of flight difference $n\sigma = \frac{t-t_0}{\delta t}$ is used to identify particles, where δt is intrinsic time resolution and t and t_0 are start and stop time respectively. The inner and outer radii are 370 cm and 399 cm from the beam axis respectively and it covers a full azimuth in mid rapidity $|\eta|$ <0.9 . The overall time resolution of TOF is given by, $\sigma_{TOF} = \sqrt{\sigma^2_{intrinsic} + \sigma^2_{t0}}$, where last term is the resolution in initial time from T0 detector.

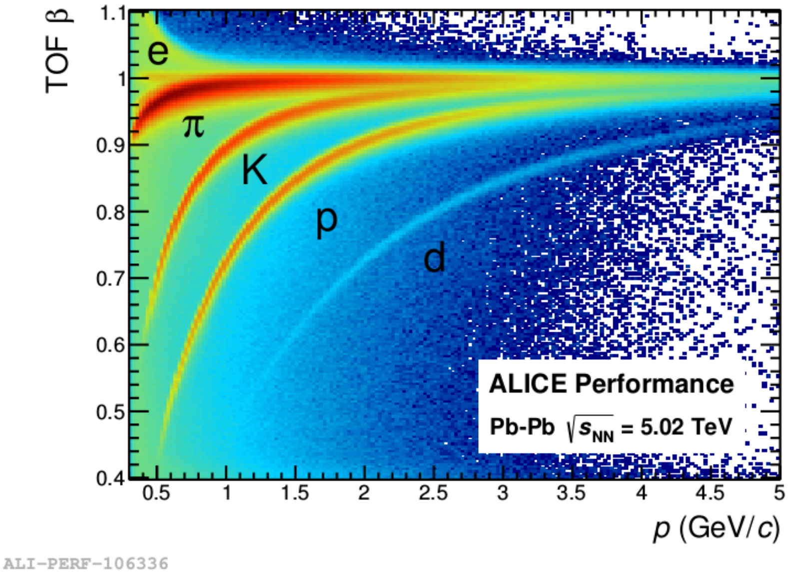

Figure 2.7: ALICE Time-Of-Flight technique [15]

2.3.4 Transition Radiation Detector

A relativistic charged particle passing through an inhomogeneous medium, particularly the boundary between materials with different electrical properties, emits radiation proportional to its energy [1]. This allows particle types to be distinguished from each other. This is called transition radiation. TRD is the main detector for electron detection of momentum above 1 GeV/c and discrimination of electrons from hadrons. By measuring the specific energy loss dE/dx in the TPC, electrons can be identified below 1 GeV/c. ALICE-TRD is part of the ALICE central barrel with a coverage of full ϕ and -0.84 $\leq \eta \leq$ 0.84. It is placed at a radial distance from 290 cm to 368 cm from the beam axis. The TRD consists of a radiator and drift chamber operated with a mixture of Xe/CO2(85/15) [14]. Electrons can be distinguished from other charged particles by producing transition radiation and having a higher dE/dx due to the relativistic rise of the ionisation energy loss.

2.4 The Forward detectors

The forward detectors are Photon Multiplicity Detector (PMD), Forward Multiplicity Detector (FMD), Cherenkov detector T0, Scintillator detector V0 and Zero Degree Calorimeter [11]. Their main purpose is to provide Level-0 trigger and multiplicity information in forward/backward region. FMD, T0 and V0 are located on both sides of Interaction Point.

2.4.1 T0 detector

The two T0 detectors -T0A and T0C, consisting of Cherenkov radiators are placed on the opposite sides of the Interaction Point (IP). T0C is placed at 70 cm from the IP and T0A is placed at 360 cm from the IP. The main goal of T0 is to supply fast timing signals for the L0 trigger, to give a wake-up call for TRD and to provide start time or collision time for TOF detector for particle identification. T0 covers $2.9 \leq |\eta| \leq 3.3$ and $4.5 \leq |\eta| \leq 5$ on both sides of IP. The timing resolution of T0 is better than 50 ps. The first trigger function is very important to discriminate beam–gas interactions. With this time resolution ±1.5 cm accuracy in vertex determination is obtained. If the vertex position lies within the pre–defined values, an L0 trigger signal known as dT0–vertex will be generated. The T0 signal must correspond to the real time of the collision and it has to be independent of the vertex position. Cherenkov detectors with quartz radiators are chosen because fast scintillators may not survive for long under heavy dose of radiation and quartz is radiation hard. Also, it has very fast light emission compared to other fast scintillators.

2.4.2 V0 detector

It is the basic detector to estimate centrality of a collision. The centrality is obtained from the deposited energy in the V0 detectors. This deposited energy is directy proportional to the number of primary particles produced in the collision i.e. to the centrality. Two scintillating V0 detectors - V0A and V0C are placed at a distance of 340 cm and 90 cm from the IP respectively on both sides of IP having pseudo-rapidity coverages V0A ($2.8 < \eta < 5.1$) and V0C ($-3.7 < \eta < -1.7$). V0 mainly provides online L0 centrality trigger. It supplies minimum bias trigger for central barrel detectors in p-p and heavy-ion collisions. Minimum bias trigger requires the condition of at least one particle hit on V0A, V0C and both V0A and V0C. The trigger efficiency would be more with only V0A or V0C but due to background of interaction of beam with the residual gas of beam pipe, it is not advantageous. From the time of flight information of the particles detected by each V0, it can distinguish the background particles from the particles coming from actual collisions as shown in Fig. 2.8. There is a difference of about 6 ns between real events and events associated to beam gas interactions. The mean number of hits are 10-20 for rings of V0C and little smaller for V0A. The charged particles emitted inside the acceptance angles of the V0A and V0C rings are about 1000-1600 and 1400-1800 respectively. To identify a beam-beam collision, the event should occur on both V0A and V0C at the expected time, i.e. 11 ns after the collision on V0A and 3 ns after

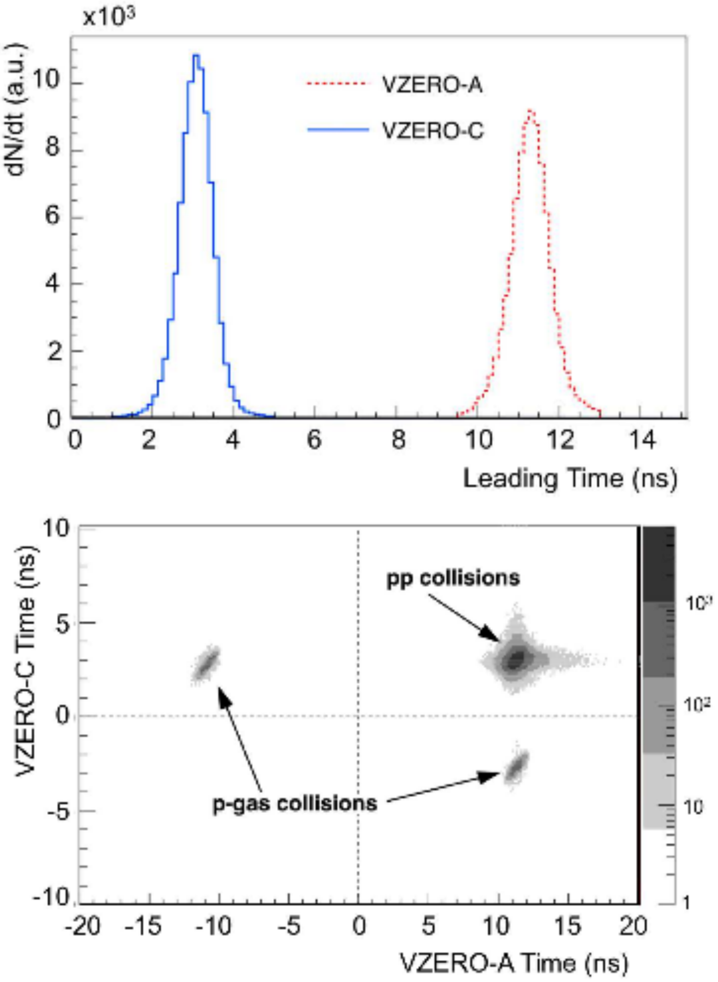

Figure 2.8: Distinguishing real events from beam gas interaction using V0 detector [12]

the collision on V0C. The V0 provides centrality measurement based on the energy deposited in the scintillators. The relation between the total charge collected inside a V0 ring and the number of primary charged particles emitted into the corresponding pseudorapidity range is extracted. In 2009 and 2010 p-p data taking periods, the ALICE minimum bias(MB) trigger required a hit in the SPD or in either of the V0 arrays. Later, (2011 and 2012), the trigger required hits in both V0 arrays and any other detector triggering due to the increase in the LHC luminosity and beam background for p-p collision. In Pb–Pb collisions, it requires at least two of the following conditions: (a) two hits in the outer layer of the SPD, (b) a signal in V0A (c) a signal in V0C. At the

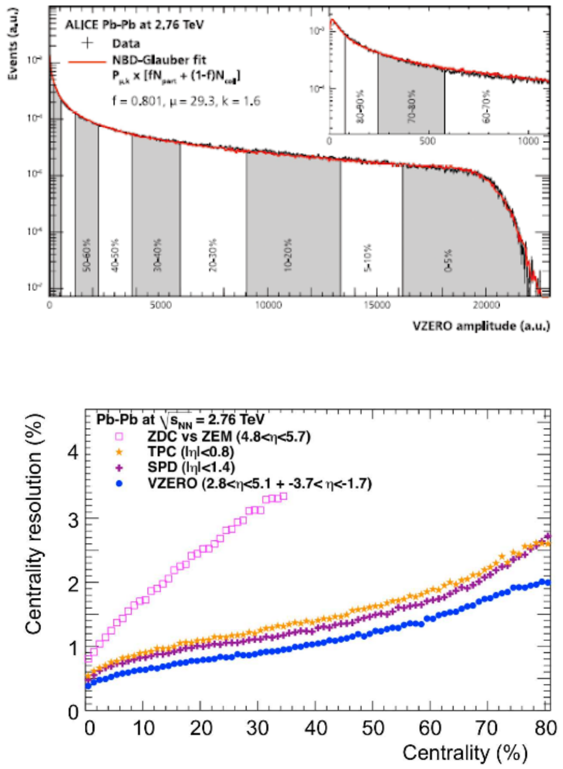

Figure 2.9: Centrality estimation using V0

end of 2010 Pb–Pb data taking period, the MB trigger was restricted to the coincidence between SPD & both V0s as the luminosity increased.

2.4.3 Zero Degree Calorimeter

When two nuclei collide, they can overlap fully or partially. In peripheral collision, a small portion of the nuclei overlap, therefore only a few nucleons participate in that collision and most of the nucleons just fly apart along the beam direction without participating. These are called spectator nucleons [13]. ZDC is the farthest detector from the IP which collects these spectator nucleons. These spectators deposit their energy in ZDC. For central collisions, the deposited energy is very small, whereas, for peripheral collisions, the energy deposited is large. Therefore, the centrality of a collision can be estimated by ZDC. It consists of two proton calorimeters (ZP) to detect protons and two neutron calorimeters (ZN) to detect neutrons, placed 115 meters away from the IP on both sides along the beam line. Hence, they are called Zero Degree Calorimeters (ZDC).

2.4.4 Triggers:

The data from all the underground ALICE detectors are transmitted to the Data Acquisition farm near the surface over optical fibers using the Detector Data Links (DDLs). There are two types of computers there. The Local Data Concentrators (LDCs) or the first layer of computers receives and formats the data and send it to the Global Data Collectors (GDCs) or second group of computers after data is accepted by the High Level Trigger (HLT). GDCs put all the things together to create the so-called events which are then stored on local disks (the Transient Data Storage - TDS) in files encoded using the AliROOT format. The data files are finally transferred to the CERN Computing Centre and are ready to be published on the Grid.

ALICE experiment uses four online systems to control, read out and monitor different sub-detectors: trigger system, Detector Control System (DCS), High Level Trigger(HLT) and Data AcQuisition (DAQ). The Experiment Control System(ECS) organizes the operations controlled by these four systems.

The trigger system (hardware trigger) selects events of particular interest while rejecting the others. A sub-detector is called trigger detector when it participates in the generation of a trigger decision, whereas it is called a readout detector when it takes part in the readout of data. In the same run, a sub-detector can be both triggering and readout detector. The trigger system receives triggers from many triggering detectors, makes decisions and selections, and then sends the final trigger decisions to readout detectors. ALICE provides three level trigger system - Level-0 (L0), Level-1 (L1) and Level-2 (L2) triggers. In some readout detectors, trigger decision has to be sent in $1.2\mu s$ after the collision which is very fast for some triggering detectors. A L1 trigger is defined for those requiring longer time than L0 triggers (6.5 μs after L0). ACORDE, TOF, HMPID, PHOS, V0, T0, muon spectrometer produces L0 trigger. TRD produces L1 trigger for electrons of high momentum. EMCal provides L0 and L1 triggers. The final L2 takes into account the past-future protection whose aim is to make sure that the selected events for readout are not damaged by pile-up. The past-future protection requirement of the TPC is the largest with $\pm 88\ \mu s$ due to the long drift time.

2.4.5 ALICE Offline analysis:

After reconstruction, the events are called Event Summary Data (ESD) which contain all information about an event and its tracks like trigger type, vertex, centrality, multiplicity and track by track PID from various detectors. But, ESD files are of huge volume and not efficient to handle.Therefore, the data files are compressed to Analysis Object Data (AOD) which are derived from ESD by filtering. Tracks which pass some sets of cuts are stored and rest are deleted from AOD. Thus AOD contains only the physics related data and is efficient to handle, though analysis can be done using both AOD and ESD.

Bibliography

[1] LHC -The Guide, https://home.cern/resources/brochure/cern/lhc-guide

[2] https://alice-wiki.gsi.de/foswiki/bin/view/Main/Research

[3] The CERN Large Hadron Collider : Accelerator and Experiments, Volume 1, Breskin, Amos (ed.) and Voss, Rudiger (ed.) (CERN), 2009.

[4] The ALICE experiment at the CERN LHC, K. Aamodt et al., [ALICE Col- laboration], J. Instrum. 3, S08002 (2008).

[5] ALICE Inner Tracking System (ITS): Technical Design Report, CERN- LHCC-99-012, http://edms.cern.ch/file/398932/1.

[6] https://alice-collaboration.web.cern.ch/node/34999

[7] ALICE Time Projection Chamber: Technical Design Report, CERN- LHCC-2000-001, http://cdsweb.cern.ch/record/451098.

[8] Røed, Ketil & Ullaland, K. & Helstrup, Haavard & Natås, T. (2021).

[9] ALICE Time-Of-Flight system (TOF): Technical Design Re- port, CERN- LHCC-2000-012, http://cdsweb.cern.ch/record/430132.

[10] ALICE Time-Of-Flight system (TOF): addendum to the technical design report, CERN-LHCC- 2002-016, http://cdsweb.cern.ch/record/545834.

[11] ALICE forward detectors: FMD, T0 and V0: Technical Design Report, CERN-LHCC-2004-025, http://cdsweb.cern.ch/record/781854.

[12] E. Abbas *et al.* [ALICE], JINST **8** (2013), P10016 doi:10.1088/1748-0221/8/10/P10016 [arXiv:1306.3130 [nucl-ex]].

[13] ALICE Zero-Degree Calorimeter (ZDC): Technical Design Report, CERN- LHCC-99-005, http://cdsweb.cern.ch/record/381433.

[14] L. Lijiao, CERN-THESIS-2011-356.

[15] ALICE Collaboration: ”Performance of the ALICE Experiment at the CERN LHC” Int. J. Mod. Phys. A 29, 1430044 (2014) .

Chapter 3

Multiplicity and pseudo-rapidity density distributions of charged particles produced in p-p, p-A and A-A collisions at RHIC & LHC energies

3.1 Introduction

Multiplicity and pseudorapidity (η) density distributions of charged particles along with the transverse momentum (p_T) spectra constitute some of the basic observables for understanding the particle production mechanisms in high-energy elementary particle and in heavy-ion collisions [1–4]. The dependence of these distributions on the colliding particle species, collision energy, and collision centrality have been extensively discussed in the literature [5–10]. In proton-proton (p-p) collisions, these distributions provide precise calibration of particle production models such as PYTHIA [11] and HERWIG [12], which are used to make predictions of various searches including those of physics beyond the standard model. These measurements play an important role in the study of heavy-ion collisions at ultra-relativistic energies in which short-lived systems consisting of nuclear matter at extreme conditions of temperature and energy density are created. There is evidence that this matter undergoes a phase transition from a confined state to a de-confined state of quark-gluon plasma (QGP) [13,14]. A comparison of the charged particle distributions in p-p, p–A, and A–A collisions are essential to characterize the formation of QGP and understand the particle production mechanisms.

The measured charged-particle multiplicity and p_T distributions are dominated by the final state interactions and the state of matter at freeze-out. Nonetheless, these distributions are also sensitive to the initial stages of the collision. At small Bjorken-x (expressed as $x = \frac{p_T}{\sqrt{s}}e^{-y} \approx \frac{p_T}{\sqrt{s}}e^{-\eta}$, y being the rapidity), the gluon density of the parton distribution functions (PDF) of the proton grows and is expected to reach a saturation domain [15–17]. So the particle productions at high collision energies and at forward rapidities are characterized by a large number of gluons [18–23]. With present day theoretical understandings and available results from the deep inelastic scattering (DIS) experiments at HERA [24,25], it becomes possible to study the expected growth and saturation of gluon density at high collision energies. The measurements of produced charged particle multiplicity, p_T, and η distributions are typically restricted to the mid-rapidity region. Such restrictions arise in part because of favorable kinematic conditions at the mid-rapidity and largely because of experimental limitations at forward rapidities. Understanding the particle production dynamics, including effects of nuclear stopping, color transparency, jet quenching, and long range correlations, requires the measurement of particle production in full pseudorapidity ranges. However, the energy-momentum conservation dictates that the particle production must vanish at or beyond the beam rapidity. It is thus of interest to consider pseudorapidity ansatz that assumes vanishing density at such large rapidities. These may then be compared to production models and may, in principle, be used to estimate the total charged-particle production in p-p and A–A collisions. The precision achievable with such extrapolations is obviously limited by the quality of the ansatz but it can be tested with existing p-p and A–A collision models. However, no specific or widely accepted pseudorapidity/rapidity model is currently available in the literature to carry out such extrapolations. In this work, we exploit the large body of available experimental data measured in high-energy p-p, p–A, and A–A collisions to examine and compare the merits of three ansatze towards a phenomenological description of the pseudorapidity density as well as the extrapolation and integration of the measured densities to estimate the total charged-particle production with beam energy. Our analysis is based on data collected from a variety of collision systems and for collision energies ranging from a few GeV to the top LHC energy. These distributions, at close to beam rapidities, are used to study the limiting fragmentation of particle production [26–28]. Multiplicities and pseudorapidity densities at the mid-rapidity at CERN SPS (Super Proton Synchrotron) and RHIC (Relativistic Heavy Ion Collider) energies have been observed to be proportional to the number of participating nucleons (N_{part}) [29,30]. But at higher energies of the CERN Large Hadron Collider (LHC), the N_{part} scaling has been observed to be broken [31,32]. One of the main reasons for this scale breaking is the enhancement in gluon productions at high energies (low Bjorken-x) [16, 17, 33]. The chapter is organised as follows, in sec. 2, we examine the measured charged particle multiplicity, and pseudorapidity distributions, $dN_{ch}/d\eta$, observed in p-p, p–A, and A–A collisions across a wide range of beam energies and compare them with results from the selected event generators. In sec. 3, we parameterize these $dN_{ch}/d\eta$ distributions using three different ansatze to obtain a satisfactory model that one can integrate over the full pseudorapidity range spanned by the particle production. Such an extrapolation requires that we examine, in sec. 4, the measured distributions in the vicinity of the beam rapidity and study the applicability of the notion of limiting fragmentation. In sec. 5, we use the favoured ansatz to estimate the total number of charged particles produced per N_{part} as a function of the collision energy and centrality. We inspect whether the charged particle production scales with Npart irrespective of the collision energy. Using the parameterization of the pseudorapidity density distributions, we give predictions for these distributions as well as total charged particle multiplicities at lower collision energies of the future experiments at FAIR (Facility for Anti-proton and Ion Research) at GSI, Germany and NICA (Nuclotron-based Ion Collider fAcility) at JINR, Russia. Additionally, we extend the charged particle multiplicity density at $\eta = 0$ for the proposed HE-LHC (High-Energy LHC) and FCC (Future Circular Collider) at CERN. Finally, in sec. 6, we explore whether selected initial condition scenarios can be meaningfully constrained by measured particle multiplicity distributions. The study has been summarized in sec. 7.

3.2 Charged-particle multiplicity distributions

In this section, we present the charged particle multiplicity density at mid-rapidity and the pseudorapidity distributions from the available experimental data for p-p, p–p, d–Au, p–Pb, Au–Au, and Pb–Pb collisions. These data are compared to calculations from event generators. For p-p and p–$\bar{p}$ collisions, the multiplicities are calculated with PYTHIA (Perugia tune) [11], whereas those for A–A collisions are computed with UrQMD [34–37], AMPT [38–40], EPOS (we have used EPOS-LHC v3.4) [41–43], and THERMINATOR [46]. UrQMD (Ultrarelativistic Quantum Molecular Dynamics) is a microscopic transport model based on the covariant propagation of all produced hadrons in combination with stochastic binary scatterings, color string formation, and resonance decay. It has been widely used to simulate the production of different particles, particle flow and fluctuations. AMPT (A Multi-Phase Transport) models the initial stage of A–A collisions in terms of partonic interactions. It converts the produced partons into hadrons and includes a hadronic interactions stage [38–40]. AMPT calculations have been carried out with the string melting (SM) option, which involves a fully partonic QGP phase that hadronizes through quark coalescence. EPOS is a hybrid event generator describing A–A as well as p-p collisions in terms of a core (high density) and corona (low density) components [41,43]. It describes the evolution of the core component with a viscous hydrodynamical model while collisions within the corona are computed with Gribov-Regge (GR) theory and perturbative QCD [41,42]. The core/corona approach is known to successfully reproduce the measured collision centrality evolution of several observables, including relative particle abundance ratios, p_T distributions, and anisotropic flow [41–45]. THERMINATOR (THERMal heavy IoN generator) is a statistical hadronization model commonly used to estimate the relative abundances of particles species produced in relativistic heavy-ion collisions. It enables arbitrary implementations of the shape of the freeze-out hyper surface and the expansion velocity field. The multiplicities were computed including Hanbury Brown and Twiss (HBT) effect and 3+1 dimensional profiles [46].

3.2.1 Charged-particle multiplicity density at mid-rapidity

The charged-particle multiplicity density at mid-rapidity $dN_{ch}/d\eta|_{\eta=0}$ has been reported for different colliding systems, collision centralities and collision energies. The average number of participants ($< Npart >$) characterizes the collision centrality and colliding system.

In Fig 3.1, we present a compilation of the measurements of scaled charged particle multiplicity density at mid-rapidity, $(2/< N_{part} >)dN_{ch}/d\eta|_{\eta=0}$, as a function of collision energy in p-p [47–49], p–$\bar{p}$ [50,51], Au–Au [5,52–57], Pb–Pb [58–60], d–Au [61], and p–Pb [62–64] collisions measured at Fermilab, RHIC, and LHC energies. Results from p-p and $p\bar{p}$ collisions are for non-single diffractive

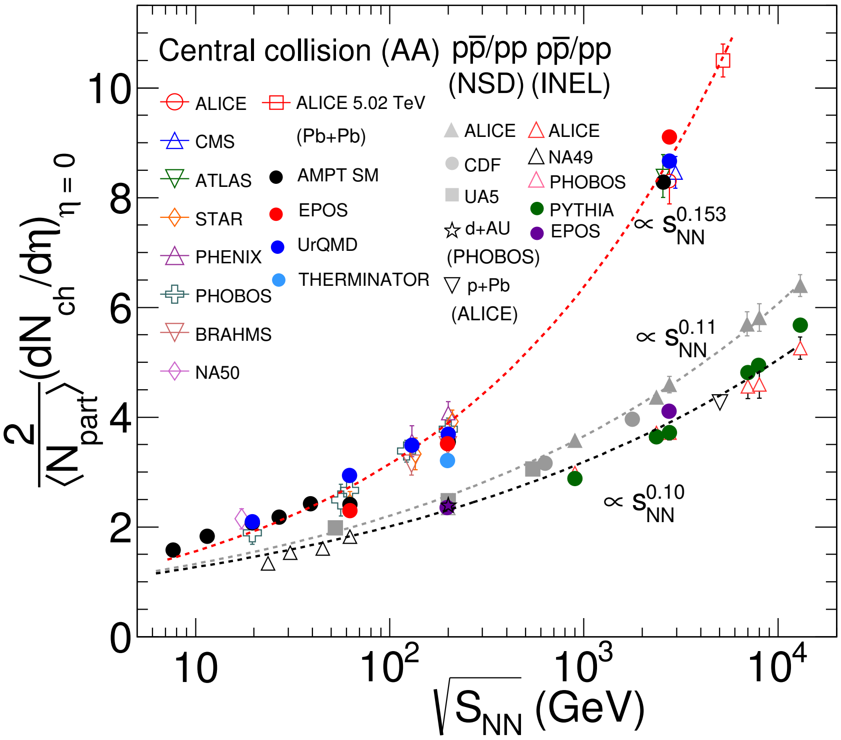

Figure 3.1: Compilation of measurements of the beam-energy dependence of charged- particle multiplicity density at mid-rapidity, scaled by the average number of participating nucleon pair ($< Npart > /2$). Data from p-p, p–$\bar{p}$, d–Au, p–Pb, Au–Au, and Pb–Pb collisions are parameterized with power-law fits (dash-lines) and compared to calculations from event generators.

(NSD) as well as inelastic (INEL) collisions, whereas those from Au–Au and Pb–Pb collisions correspond to most central collisions. The multiplicity densities measured in p-p ($p\bar{p}$) and A–A collisions exhibit rather different dependence as a function of collision energy. These dependencies can be characterised with power-law fits performed separately for A–A , NSD p-p, and INEL p-p (p–$\bar{p}$) collisions. We find that the $\sqrt{s}$ dependence of the multiplicity density of p-p (p–$\bar{p}$) collisions are well matched by power laws of the form $(s_{NN})^{\alpha}$ with exponent $\alpha = 0.10$ and $\alpha = 0.11$ for INEL and NSD collisions, respectively. In contrast, the multiplicity densities observed in A–A collisions exhibit a steeper dependence on the beam energy and are best described with a power law exponent $\alpha = 0.153$. Additionally, we find that the dependencies of the multiplicity densities measured in d–Au and p–Pb collisions are similar to those observed in p-p collisions. Comparing the results from different models and data shown in Fig 3.1, we note that for the p–p collision system, PYTHIA predictions are in good agreement with INEL data for beam energies $\sqrt{s_{NN}} \geq 100$ GeV. In the case of A–A systems, one finds that AMPT SM and UrQMD predictions are in good agreement with data over the entire $\sqrt{s_{NN}}$ range considered in this work. We additionally find that EPOS predictions are also in reasonable agreement with data from both p–p and A–A systems over a wide range of beam energies. However, the single THERMINATOR prediction considered at $\sqrt{s_{NN}} =$ 200 GeV is found to considerably underestimate the measured charged-particle density. Overall, PYTHIA , EPOS, AMPT, and UrQMD are found to reproduce reasonably well the observed $\sqrt{s_{NN}}$ power law behavior even though they are based on rather different interaction and transport models. The $\sqrt{s_{NN}}$ evolution of the $\frac{2}{<N_{part}>}\frac{dN_{ch}}{d\eta}$, an integrated observable, is not a strong discriminant of these models and their underlying particle production mechanisms. Although historically important, however, the measurements of the scaled charge particle density at central rapidity provide only a rather limited amount of information about the specific particle creation and transport mechanisms involved in p-p and A–A collisions [10]. Additional insight into these mechanisms, however, may be gained from charged-particle pseudorapidity distributions.

3.2.2 Pseudorapidity distributions

The upper panel of Fig 3.2 displays $dN_{ch}/d\eta$ distributions measured in p-p collisions at energies ranging from 0.9 to 13 TeV [47–50] and $p - \bar{p}$ collisions at 0.2 TeV [51] (open symbols), while the lower panel presents the pseudorapidity distributions of charged hadrons measured in the 6% most central Au–Au collisions in the range $19.6 \leq \sqrt{s_{NN}} \leq 200$ GeV [5,54–57,61],and top 5% central Pb–Pb collisions at 2.76 TeV [58,60]. Focussing our attention to the upper panel of Fig 3.2, we note that only the UA5 data cover a wide enough pseudorapidity range capable of revealing the full shape of the η distribution measured in p-p collisions while the measurements reported by the

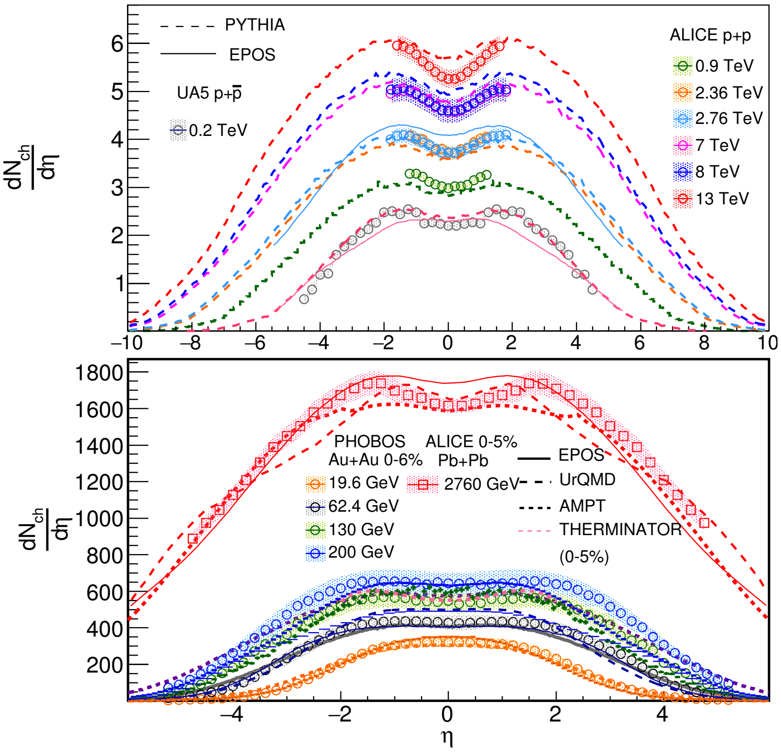

Figure 3.2: Comparison of selected experimental $dN_{ch}/d\eta$ distributions of measured in p-p and $p-\bar{p}$ collisions (upper panel) and Au–Au and Pb–Pb collisions (lower panel) with calculations performed with the PYTHIA, AMPT, UrQMD, EPOS and THERMINATOR models.

ALICE collaboration are limited to the central rapidity region in p-p collisions. One nonetheless observes that the particle density produced in p-p ($p-\bar{p}$) collisions rises monotonically, as expected, with beam energy. One also notes that the measured pseudorapidity distributions all feature a dip, centered at $\eta = 0$, whose depth and width increases with rising $\sqrt{s}$. The presence of this dip is in part associated with partial transparency and limited stopping power of the colliding protons (or anti-protons) [73]. The dip may also result, in part, from the measurement being reported as a function of pseudorapidity. A boost invariant rapidity distribution would indeed yield a broad dip in pseudorapidity owing to the presence of mass term in the denominator of $y- > \eta$ transformation Jacobian. The pseudorapidity distributions measured in p-p ($p-\bar{p}$) collisions are compared with the Monte Carlo calculations performed with PYTHIA 6.4 [11] (dash lines) and EPOS [44] (solid lines) event generators. One observes that both PYTHIA and EPOS approximately reproduce the magnitude and η dependence of the distributions: both models indeed capture the essential features of the measured distributions, including the presence of the widening and deepening dip, centered at $\eta = 0$, with increasing $\sqrt{s_{NN}}$. However, PYTHIA appears to be in better agreement with the data than EPOS at 0.2, 2.76, and 8 TeV. In particular, it may be observed that EPOS does not reproduce the dip structure seen in $(p - \bar{p})$ data at 0.2 TeV.

Let us now examine the pseudorapidity distributions reported by the PHOBOS and ALICE collaborations shown in the lower panel of Fig 3.2. The PHOBOS data cover the range -5.4 $\leq \eta \leq$ 5.4 whereas those of the ALICE experiment span the range -5.0 $\leq \eta \leq$ 5.5. One finds that the pseudorapidity distribution observed at $\sqrt{s_{NN}} = 19.6$ GeV features an approximate Gaussian shape peaked at $\eta = 0$, while distributions observed at higher beam-energies are much broader and features the dip structures qualitatively similar to those observed in p-p collisions. However, the dip structures observed in A–A collisions are typically shallower and wider than those observed in p-p collisions.

The experimental data are compared to calculations based on the UrQMD, AMPT, EPOS, and THERMINATOR models shown as solid lines in Fig 3.2. The calculations were performed within p_T ranges reproducing the experimental conditions of the PHOBOS and ALICE experiments. Overall, we note that all four models qualitatively reproduce the observed distributions. However, we also note that best agreement with the measured pseudorapidity density distributions is obtained with the EPOS model at beam energies $\sqrt{s_{NN}} \leq 200$ GeV, while at 2.76 TeV, none of the models reproduce the observed distributions quantitatively. Overall, all four models considered manage to capture the general trend of the observed data, including the produced particle density and its dependence on pseudorapidity, but none of them perfectly reproduce the shape of the measured distributions. EPOS arguably works very well given that it matches not only the amplitude and breadth of the distributions but it also produces a dip near $\eta = 0$, albeit with insufficient depth.

EPOS predictions are $\approx 5\%$ lower at RHIC energies and approximately $\approx 2\%$ higher at 2.76 TeV. AMPT and UrQMD, on the other hand, seem to reproduce the measured densities rather well at mid-rapidity, across the entire $\sqrt{s_{NN}}$ range presented in Fig.3.2, but fail to reproduce the overall shape at higher η values. THERMINATOR, on the other hand, is doing rather poorly at $\sqrt{s_{NN}} =$ 200 GeV.

3.3 Parameterization of the pseudorapidity distributions

Although the PHOBOS and ALICE data presented in the lower panel of Fig 3.2 cover large ranges of pseudorapidity, they do not capture the full range of particle production involved at the top RHIC & LHC energies. In fact, most reported measurements of charged-particle pseudorapidity distributions are limited to somewhat narrow ranges of pseudorapidity and do not account for the full region of particle production. For instance, the measured distributions reported by the ALICE collaboration for Pb-Pb collisions cover a fairly wide range, $|\eta| < 5.5$, but this range is quite narrow relative to the beam rapidity ($y_{beam} \approx 9.0$). One may then wonder how much particle production actually takes place at forward/backward rapidities? Can the stark differences among the $\sqrt{s_{NN}}$ dependence of the multiplicity densities observed in p-p and A–A collisions result from an overall increase in the produced multiplicity per participant pair or does it result simply from a shift in the particle production towards the central rapidity, due possibly to a larger stopping in A–A collisions?

Very few experiments are equipped to cover the entire pseudorapidity range required to answer these questions unambiguously. In the absence of such measurements, we seek to parameterize the measured η distributions to obtain sensible extrapolations at forward/backward rapidities that may be used to estimate the total charged-particle production. In the transverse direction, extrapolation of the measured particle densities, $\frac{1}{p_T}\frac{dN}{dp_T}$ to zero and infinite p_T is relatively straightforward because the cross-section must vanish at these limits [72]. Evidently, models used to integrate p_T spectra are not constrained outside of the fiducial p_T acceptance, but the fact that the cross-section vanishes at null and infinite pT significantly constrains the shape of p_T distributions. Uncertainties as to the exact shape of the p_T distribution outside of the fiducial acceptance thus yield systematic uncertainties on the integral of the distributions. We seek to use the same concept towards extrapolating at forward and backward rapidities beyond the fiducial pseudorapidity acceptance. The pseudorapidity density must obviously vanish at suitably large values of $|\eta|$ but extrapolation beyond the measurement acceptance does require assumptions about the overall shape of the distributions. In this work, we explore three fitting functions to fit and extrapolate measured yields beyond their fiducial ranges. These functions can then be integrated numerically over the entire range of particle production to obtain (extrapolated) total produced particle multiplicities. The analysis of the shapes of the pseudorapidity distributions is based on the distributions presented in Fig 3.2. We first note that the pseudorapidity density distributions produced in symmetric collisions (e.g., p-p and A–A) are symmetric about $\eta = 0$, but distributions of the pA collisions feature a pronounced forward/backward asymmetry, with an excess of particles being produced in the nucleus direction. We further note that the shape of the pseudorapidity distributions may be characterized by one broad peak with approximate Gaussian shape or two peaks of approximately Gaussian shape separated by a trough. For simplicity, we thus consider three basic shapes defined according to:

$$\frac{dN_{ch}}{d\eta} = \frac{c\sqrt{1 - 1/(\alpha \cosh \eta)^2}}{1 + e^{(\eta - \beta)/a}} \tag{3.1}$$

$$\frac{dN_{ch}}{d\eta} = A_1 e^{-\frac{(\eta-\mu_1)^2}{2\sigma_1^2}} + A_2 e^{-\frac{(\eta-\mu_2)^2}{2\sigma_2^2}} \tag{3.2}$$

$$\frac{dN_{ch}}{d\eta} = A_1 e^{-\frac{\eta^2}{2\sigma_1^2}} - A_2 e^{-\frac{\eta^2}{2\sigma_2^2}} \tag{3.3}$$

Equation (1) is motivated by observed symmetric trapezoidal functions with a plateau around mid-rapidity [55]. It was used by the PHOBOS collaboration to model their measurements and extract the produced total particle multiplicity. Although Eq. (1) adequately reproduces some of the measured distributions, its built-in symmetry about $\eta = 0$ limits its applicability to the symmetric collision systems exclusively. Equations (2) and (3) involve sum and differences of two Gaussian distributions, respectively. Equation (1) features four parameters (c, α, β, a), while Equation (2) involves six parameters $(A_1, \mu_1, \sigma_1, A_2, \mu_2, \sigma_2)$. Equation (3) features five parameters $(A_1, \mu, \sigma_1, A_2, \sigma_2)$ but reduces to four for symmetric collisions, which are characterized by $\mu = 0$. Figure 3.3 shows schematic diagrams of $dN_{ch}/d\eta$ distributions obtained for p-p, p–A, and A–A collisions obtained with the ansatze embodied by Eqs. 1-3. The red and blue lines and associated

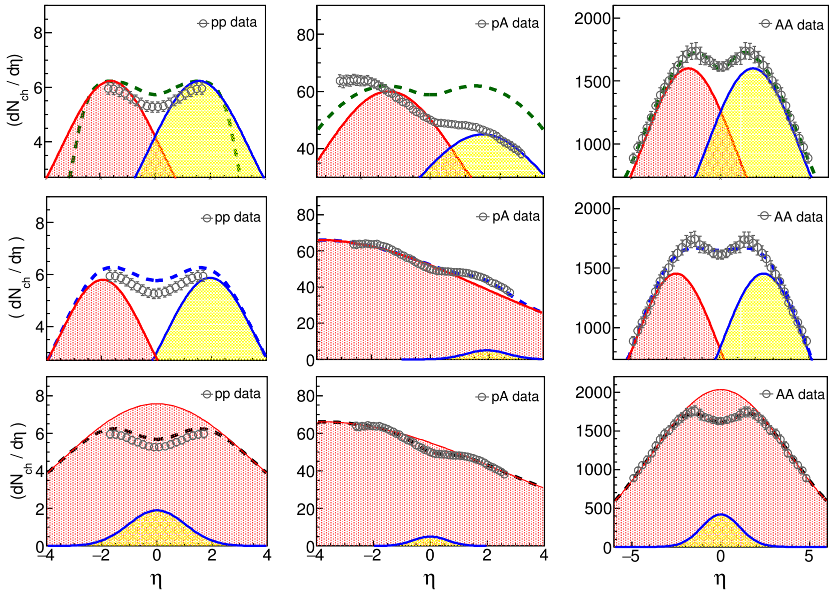

Figure 3.3: Schematic representation of $dN_{ch}/d\eta$ distributions of p-p, p–A, and A– A collisions using three different ansatze. The distributions shown as dotted lines are parameterized with three fit functions: symmetic trapezoidal (upper panels), sum of two Gaussian distributions (middle panels), and difference of two Gaussian distributions (lower panels).

shaded areas schematically represent the contributions from nucleon participants originating from either incoming nuclei. In the middle row panel, the blue dash line corresponds to the sum of both contributions. The shape of the distribution is here determined by the relative contributions of the incoming nuclei as well as the degree of nuclear stopping achieved in the collisions. In the bottom panel row, the relative contributions and stopping are modeled with a difference of two Gaussians as per Eq.(3) and illustrated with the black dash line. In the upper panel, the trapezoidal ansatz sums contributions from both the incoming nuclei and is thus not easy to visualize. In each case, the overlap region can be visualized as a measure of the dip at $\eta = 0$ for overall distribution. If the overlap region decreases, then the dip is pronounced and if the overlap region increases, the overall distribution becomes flat.

The three functions are used to fit the available experimental data displayed in Fig 3.4 – 3.6. The

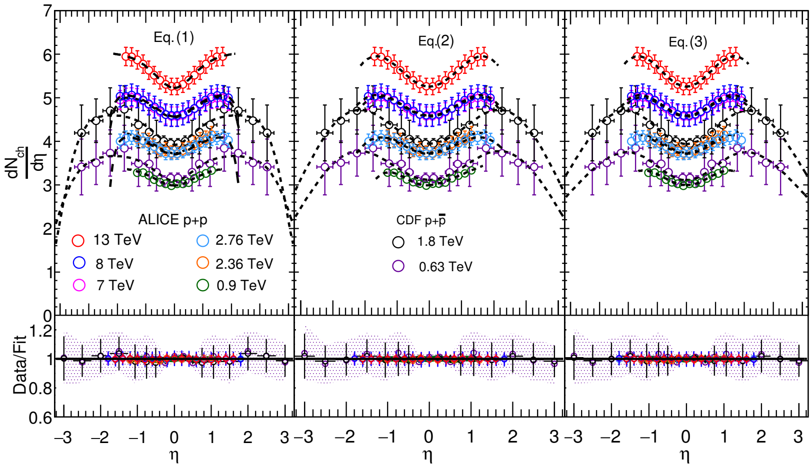

Figure 3.4: Beam energy dependence of charged particle pseudorapidity densitydistributions measured in minimum bias p-p collisions by the ALICE collaboration [47–49] and in $p-\bar{p}$ collisions by the CDF collaboration [50]. Dashed lines show best fitsobtained with Eqs. (1-3)

parameter μ of Eq. (3) is set to zero for symmetric collisions but left unconstrained for asymmetric systems. Fits to the pseudorapidity distributions measured in p-p and $p-\bar{p}$ collisions are displayed in Fig 3.4; those to Cu–Cu, Au–Au, and Pb–Pb collisions data are shown in Fig 3.5; whereas those

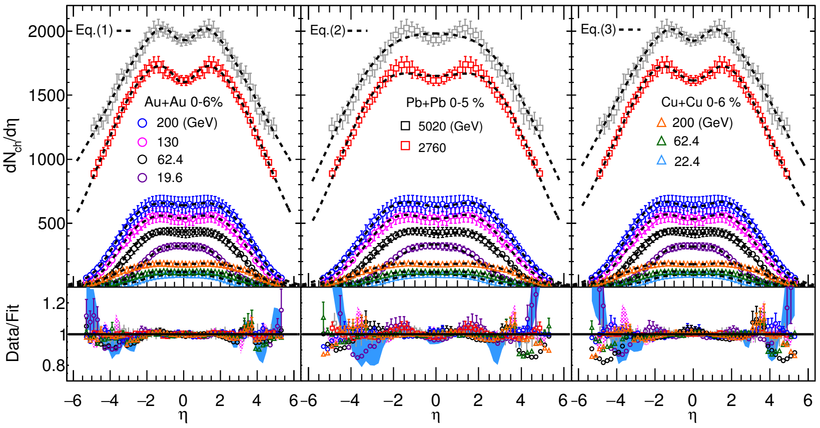

Figure 3.5: Beam energy dependence of charged particle pseudorapidity densitydistributions measured in central Cu–Cu and Au–Au collisions by the PHOBOScollaboration [54–57] and in Pb–Pb collisions by the ALICE collaboration [58]. Dashedlines show best fits obtained with Eqs. (1,2,3) from left to right panels respectively.

to asymmetric systems, d–Au and p–Pb collisions, are presented in Fig 3.6. The upper panels of each figure display experimental data and fits obtained with the three functions in distinct panels horizontally, while the lower panels of the figure show ratios of the measured data to the fits. The fits were carried out with the ROOT least square minimization function [65]. Data uncertainties included in the fits were set as quadratic sums of statistical and systematic errors reported by the experiments. The goodness of fit is reported in terms of χ^2 per degrees of freedom (χ^2/NDF) in Tab. 1. We find that the three functions fit the p-p data relatively well with χ^2/NDF typically smaller than 3. However, best fits are achieved with Eqs. (1) and (3). Similarly, we find that all three functions provide reasonably sensible parameterizations of the Au–Au, Pb–Pb, and Cu–Cu data presented in Fig 3.5. We note, however, that Eq. (1) yields fits with smaller deviations from the data, on average, in the central rapidity region. We also find that Eq. (2) does not fully reproduce the dip structure observed at central rapidity in high-energy datasets. As anticipated, fits with Eq. (1) fail to describe pseudorapidity density distributions measured for asymmetric systems but Eqs. (2,3) produce reasonable fits. Note, however,that deviations in excess of 5% are

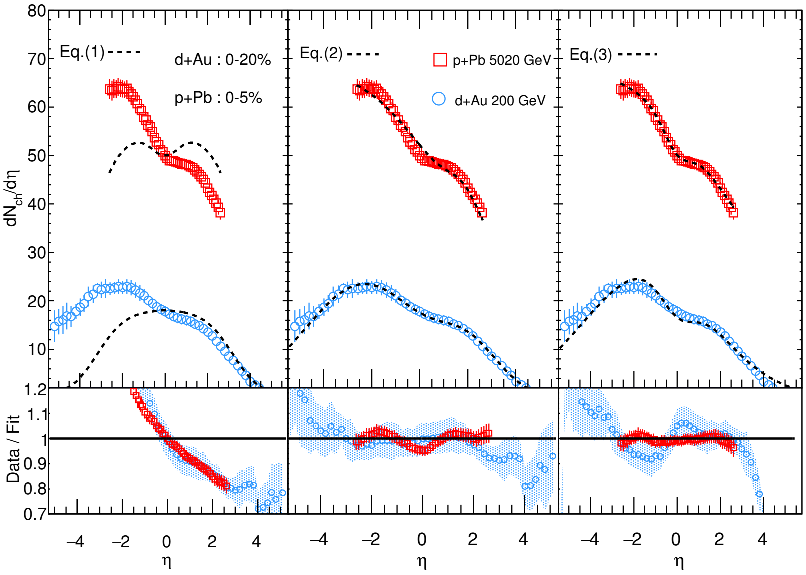

Figure 3.6: Beam energy dependence of charged particle pseudorapidity densitydistributions measured in minimum bias d–Au and p–Pb collisions measured by thePHOBOS collaboration [61] and the ATLAS collaboration [62]. Dashed lines showbest fits obtained with Eqs. (1-3).

observed at $|\eta| > 3.2$ with these models. Irrespective of the system size, centrality and collision energy, Eq. 3 can be used for forward η ranges up to the beam rapidity (where experimental measurement has severe limitations) to estimate the total number of produced charge particles. Altogether, we conclude that Eq. (3) provides the best descriptions of the pseudorapidity density distributions, regardless of collision system size and energy considered in this work.

3.4 Multiplicity distributions at large η: limiting fragmentation

Fits with Eqs. (1-3) of pseudorapidity distributions measured in Pb-Pb collisions at 2.76 & 5.02 TeV, discussed in the previous section, successfully model the data but are under constrained at large rapidities. In this section, we use the notion of limiting fragmentation to provide constraints on the shape of these distributions at large rapidity. In high-energy hadronic collisions, the limiting fragmentation [26–28, 67] concept stipulates that pseudorapidity densities reach a fixed or

System	Centrality	$\sqrt{s_{NN}}$	$\chi^2/NDF(Eq.1)$	$\chi^2/NDF(Eq.2)$	$\chi^2/NDF(Eq.3)$
pp	MB	900	1.056	0.552	0.826
pp		2360	0.691	1.367	0.742
pp		2760	2.670	14.805	1.495
pp		7000	0.458	14.805	1.495
pp		8000	1.103	9.320	0.157
pp		13000	0.416	1.312	0.0145
p-$\bar{p}$		630	2.355	2.636	2.144
p-$\bar{p}$		1800	0.986	0.184	0.155
CuCu	(0-6%)	22.4	1.1806	1.503	1.026
CuCu		62.4	0.802	0.778	0.766
CuCu		200	0.877	1.095	1.185
AuAu		19.6	0.596	0.725	0.592
AuAu		62.4	2.184	2.074	0.412
AuAu		130	1.889	2.176	0.179
AuAu		200	1.103	0.262	0.419
PbPb	(0-5%)	2760	1.813	1.562	0.943
PbPb		5020	1.319	4.216	1.462
dAu	top 5%	200	No Fit	2.149	3.57
pPb	mult class	5020	No Fit	3.299	2.118

Table 3.1: χ^2 / NDF of the fits of data presented in Figs. 4-6 with Eqs. (1-3). MB denotes minimum bias distribution.

universal curve close to the beam rapidity (y_{beam}). This implies that the particle production in the rest frame of one of the colliding hadrons is (approximately) independent of the collision center-of-mass energy. Many explanations have been suggested to interpret this behavior, including gluon saturation in the color glass condensate (CGC) framework [18–20, 66]. Indeed, parton distribution functions measured in deep inelastic scattering show that, at very high collision energies, gluons densities largely dominate those of quarks. This suggests that the medium produced in these collisions mostly consists of gluons. With increasing collision energy, the gluon density increases, eventually leading to saturation.

In the previous section, we found that Eq. (3) provides the best fit to the experimental data considered in Fig 3.4 – 3.6. But the fits remain poorly constrained at large rapidities, i.e., at rapidities in excess of $|\eta| > 3.5$. In this context, we investigate whether the notion of limiting fragmentation can further constrain our modeling of the particle density distributions.

Recent studies of limiting fragmentation have shown that Glauber-inspired models of particle production in heavy-ion collisions generally fail to reproduce limiting fragmentation [68,69] behaviour, especially at LHC energies. These studies indicate that the particle production is a function of the combination of N_{part} and number of collisions (N_{coll}), as the ratio between the two depends non-trivially on the collision energy. Hence, if the nuclei-sized domains are uncorrelated, one generically expects limiting fragmentation to be broken, which is also true in Color Glass type models. In Ref. [68], the authors have argued that the wounded parton models, provided the nucleon size and parton density vary predominantly with Bjorken-x, could in principle reproduce both multiplicity dependence with energy and limiting fragmentation. The different calculations can be verified by studying the limiting fragmentation behaviour of particle production by re-plotting the the pseudorapidity density distributions measured in central Cu–Cu, Au–Au, Xe-Xe and Pb–Pb collisions at RHIC and LHC energies as a function of shifted rapidities, η - y_{beam}. The upper panel of Fig 3.7 shows the pseudorapidity distributions for central collisions at different colliding energies as a function of $\eta-$ y_{beam} for Xe–Xe [31] and Pb–Pb [32] systems at the LHC, and Au–Au collisions at the RHIC energies. We observe that the distributions tend to converge towards a single curve close to $\eta \approx 0$. This convergence is observed to be dependent on the system size. This is already quite remarkable considering that the distributions correspond to systems with rather different number of participants and collision energies. Accounting for the system sizes, i.e., scaling (dividing) the pseudo-rapidity densities by their respective number of participant pairs, $< Npart > /2$, we obtain the distributions shown in the lower panel of Fig 3.7. We observe that the scaled distributions obtained from Xe–Xe, Au–Au, and Pb–Pb collisions at several energies closely overlap and more or less follow a universal limiting fragmentation behavior near $\eta-$ $y_{beam} = 0$.

We further test the notion of limiting fragmentation with fits of the data presented in Fig 3.7 with Eqs. (1-3). Fits of the different data sets, presented in the figure, indeed merge together near

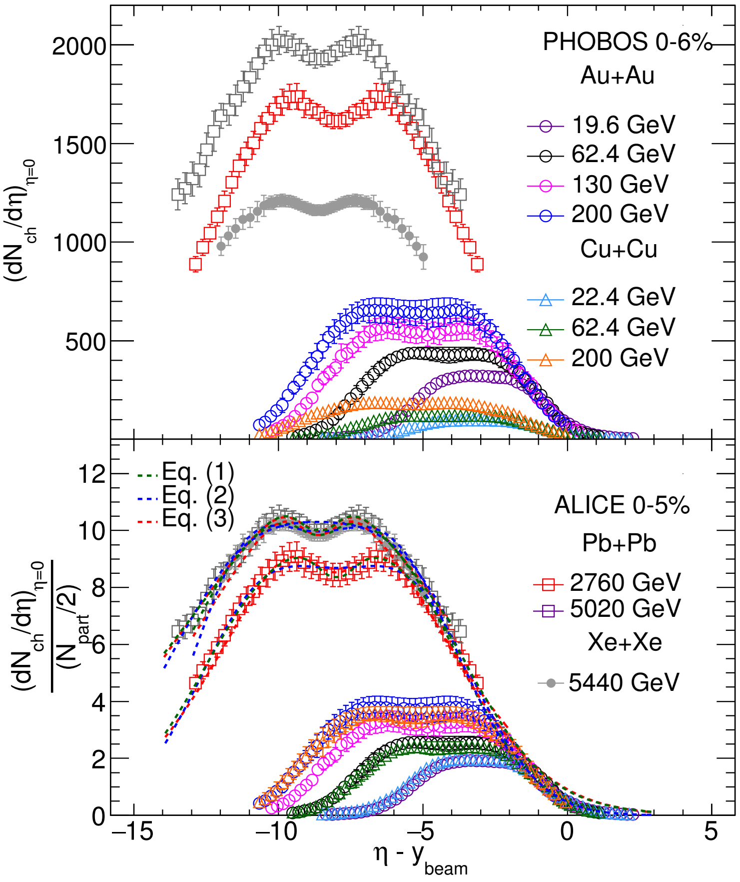

Figure 3.7: Limiting fragmentation behavior for Au–Au, Cu–Cu, Xe-Xe and Pb–Pb collisions at large η ranges, plotted as a function of $\eta -\ y_{beam}$. The y-axis in the lower panel is scaled by the number of participating nucleons pair.

the beam rapidity. In order to further validate the different ansatze, the fits were performed by restricting the fit regions and then extrapolating to higher η. This is verified for Xe-Xe collision (at $\sqrt{s_{NN}}$ = 5.44 TeV) and Pb-Pb collisions (at both $\sqrt{s_{NN}}$ =2.76 TeV and $\sqrt{s_{NN}}$ = 5.02 TeV), by fitting the experimental data in the ranges (i) $|\eta| \leq 2.0$ and (ii) -2 < η - y_{beam} < 3. We find that the extrapolations of these fits in the beam rapidity are in near perfect agreement, with a maximum mutual difference of 1%. We also verified that integrals of the fits, yielding total charged-particle multiplicity, differ by less than 5%. Additionally, we further checked the validity of the limiting fragmentation hypothesis by considering fits to the two hybrid datasets. These hybrid datesets were constructed by joining data points from LHC energies in the range -13 $< \eta$ - $y_{beam} <$ -4 (where experimental data are available), with $< Npart >$ scaled values from the STAR 200 GeV data points in the range -2 $< \eta$ - $y_{beam} <$ 2. Fits of the two hybrid sets were then performed and we verified that their integrals matched those of constrained fits to LHC only data with maximum deviations of 3.5%. We thus conclude that, within the precision afforded with the LHC data, one verifies that (1) the limiting fragmentation hypothesis is approximately valid at the LHC and (2) one can then exploit the hypothesis to constrain the LHC data at large rapidity. Using this limiting fragmentation hypothesis, and extrapolating fitting functions to the beam rapidity, it is thus possible to estimate, with reasonable accuracy, the total charge particles (N_{ch}^{total}) production at LHC energies and compare with values obtained at RHIC energies. We discuss the extraction of N_{ch}^{total} in detail in the next section.

3.5 Total charged-particle multiplicity

We proceed to determine the total charged-particle multiplicity, N_{ch}, produced in Cu–Cu, Au–Au, and Pb–Pb collisions by integration of the fitted pseudorapidity densities, constrained by limiting fragmentation, over the full range of particle production. Figure 3.8 presents $< N_{part} >$ dependence of the values of N_{ch} scaled by $< N_{part} > /2$ for Pb-Pb and Au-Au collisions at 2.76 TeV and 200 GeV respectively. Experimental data points reported by the ALICE [70] and PHOBOS [71] collaborations are shown with red and blue dash curves, respectively. Total charged-particle production values are obtained by integration of the fitted Eq. (1-3) in the range - $y_{beam} \leq \eta \leq y_{beam}$. Values obtained with Eqs. (1), (2), and (3) are shown with solid red, blue and green points, respectively. We find that the scaled values of N_{ch} (red triangles and red circles) obtained by integration of Eq. (3) are consistent, within uncertainties (represented by shaded bands), with those reported by the PHOBOS and ALICE collaborations. Only the N_{ch} values obtained at the

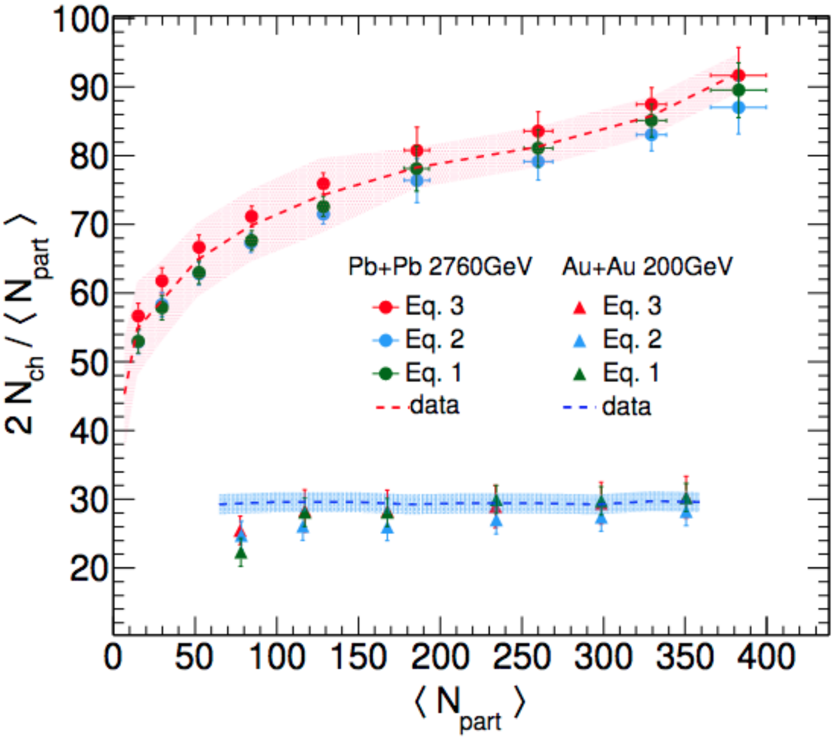

Figure 3.8: Total charge particle multiplicity scaled by the number of participant pair, $< N_{part} >$ /2, as a function of $< N_{part} >$ based on Eqs. (1-3). Red and blue dash lines correspond to data reported by the ALICE and PHOBOS collaboration based on measured charge particle multiplicity measured in the range $|\eta| \leq 5.5$ and extrapolated to - $y_{beam} \leq \eta \leq y_{beam}$. The shaded bands represent error bars correspond to the correlated systematic uncertainties reported by the experiments [70,71].

lowest $< N_{part} >$ appreciably underestimate the PHOBOS data.

Scaled values of N_{ch} obtained by integration of Eq.(1) follow a similar trend while those obtained with Eq.(2) tend to systematically underestimate the values reported by PHOBOS. Overall, we find that the best agreement with PHOBOS data is achieved using Eq.(3), with deviations of the order of 0.5% compared to 1% with the other two equations. Hereafter, we use the differences of the three fit extractions as an estimate of the systematic errors associated with the extrapolation procedure based on fits of Eq.(3) to obtain the total charged-particle multiplicities.

We now proceed to use fits of the measured pseudorapidity distributions with Eq.(3) to extract values of Nch for several colliding systems, collision energies, and collision centralities. Results are shown in Fig 3.9 as a function of $< N_{part} >$ in p-p collisions at 19.6 GeV, 200 GeV and 2.76 TeV, Au–Au collisions at 19.6, 62.4, 130, and 200 GeV, Cu–Cu collisions at 22.4, 62.4 and 200 GeV, d–Au collisions at 200 GeV, Pb–Pb collisions at 2.76 and 5.02 TeV, and p–Pb collisions at 5.02 TeV. We observe that the integrated multiplicities generally exhibit a power law dependence

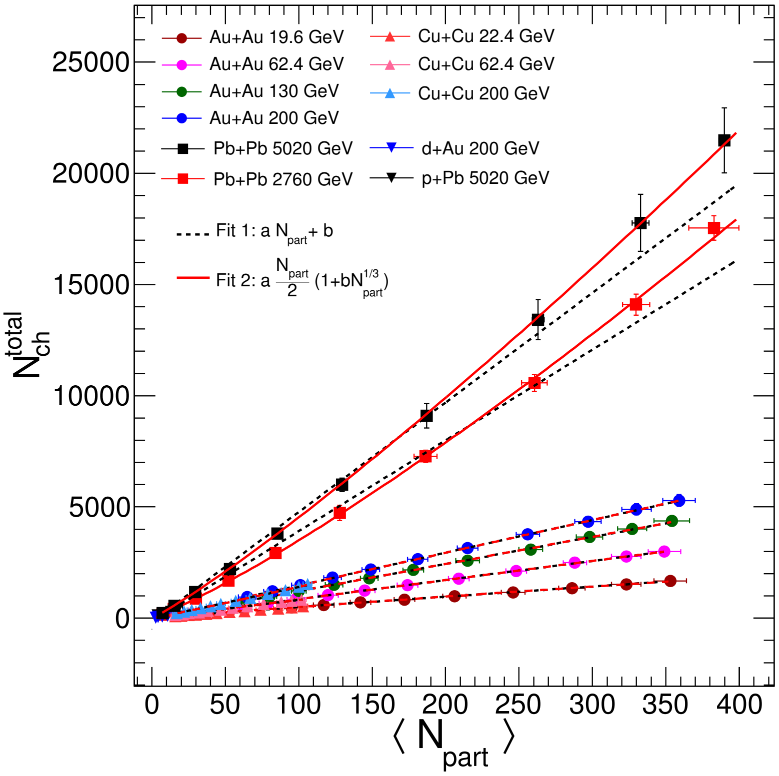

Figure 3.9: Centrality dependence of the total charged-particle multiplicity, estimated from integrals of Eq. (3) across the range - $y_{beam} \leq \eta \leq y_{beam}$, in p-p, d–Au, p–Pb, Cu–Cu, Au–Au, and Pb–Pb collisions at RHIC and LHC energies.

on the average number of participants. Additionally, while the integrated multiplicities obviously increase with the system size and collision energy, they otherwise appear, upon first inspection, to feature a similar power-law dependence on N_{part}.

We further examine the N_{ch} dependence on N_{part} by considering parameterizations of this dependence with (a) a linear function $aN_{part} + b$, and (b) a power law $aN_{part}/2(1 + bN_{part}^{1/3})$, shown in Fig.3.9 with black dashed and red solid lines, respectively. We find that the power-law parameterization provides a better description of the evolution of N_{ch}^{total} with N_{part}. Notably, the linear fit fails to describe the evolution of N_{ch}^{total} with N_{part} at LHC energies. Deviations are observed for peripheral collisions with both parameterizations. Moreover, both the linear and power law functions provide a rather poor description of the computed multiplicities in the case of p–Pb collisions. In order to further examine the evolution of N_{ch}^{total} with N_{part}, we plot the centrality dependence of the total charged particle multiplicities scaled by the number of participant pair in Fig 3.10. We observe that for Cu–Cu and Au–Au collisions at RHIC energies, scaled values of $N_{ch}^{total}/(< N_{part} > /2)$ are essentially independent of the collision centrality, whereas $(dN_{ch}/d\eta)|_{\eta=0}/(< N_{part} > /2)$, plotted in Fig 3.11, displays a monotonic rise with N_{part} in these

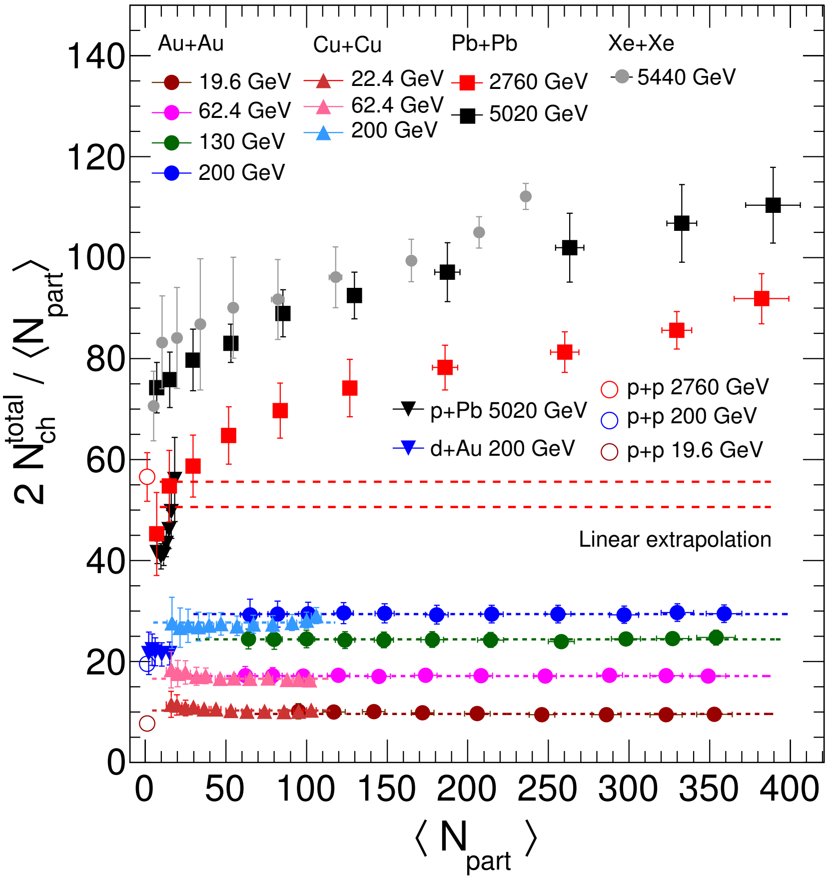

Figure 3.10: Centrality dependence of total charged multiplicity per participant pair in p-p, d–Au, p–Pb, Cu–Cu, Au–Au, and Pb–Pb collisions at RHIC and LHC energies [5,58,59]

collision systems. This implies that the shape of the η density distribution changes with centrality and becomes more peaked with increasing centrality. In contrast, we find that, at LHC energies, both $N_{ch}^{total}/(< N_{part} > /2)$ (Fig 3.10) and $(dN_{ch}/d\eta)|_{\eta=0}/(< N_{part} > /2)$ (Fig 3.11) display monotonic increase with N_{part}. For LHC collisions, the ratio $N_{ch}/(< N_{part} > /2)$ shows a growth, compatible with a power-law behavior. A similar behavior is observed for p–Pb collisions at 5.02 TeV (Fig 3.10).

The observed violation of participant scaling at LHC energies is in sharp contrast to the near

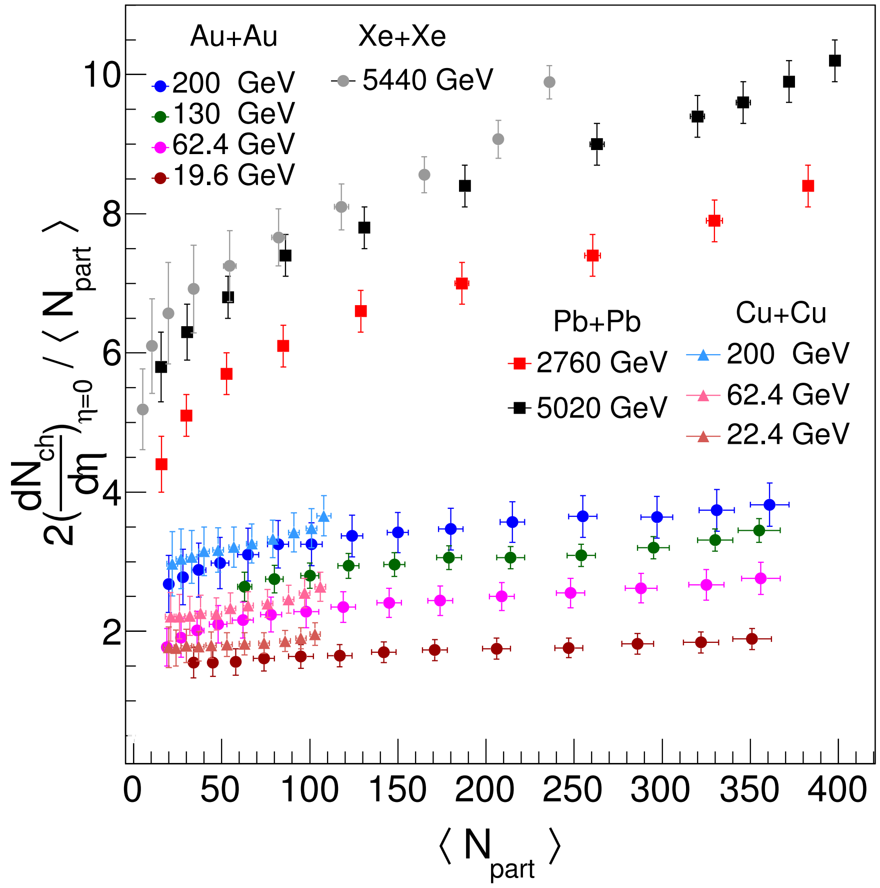

Figure 3.11: Centrality dependence of charged-particle multiplicity density at mid- rapidity in Cu–Cu, Au–Au, Pb–Pb and Xe-Xe collisions at RHIC and LHC energies.

perfect scaling observed at RHIC energies. Furthermore, a scaling violation is observed for both charged-particle multiplicity density at mid-rapidity as well as the total number of charged particles. The causes of these violations can be manifold. First, the increase in beam energy by more than one order of magnitude from RHIC to LHC energies makes the typical Bjorken-x at LHC much lower compared to that at RHIC. At RHIC energies, a transverse mass, m_T, of 1 GeV corresponds to x $\sim 10^{-2}$ at y = 0, whereas at LHC it corresponds to x $\sim 10^{-4}$. Bjorken-x values are even lower at large η. The gluon density is expected to grow and reach saturation with lowering x [74]. At the LHC, one gets to the small x domain where gluon productions dominates thereby producing large number of additional particles with no relation to the number of participants. This is consistent with the CGC formalism of the initial state of the colliding nuclei.

Alternatively, particle production at high energy may be described in terms of a two component model involving soft and hard components, $\sigma_{total} = \sigma_{soft} + \sigma_{hard}$, in which σ_{soft} represents the cross-section for soft particle production and is proportional to N_{part}, whereas σ_{hard}, the cross-section for high-p_T particle production, is proportional to the number of inelastic nucleon-nucleon collisions (N_{coll}). A significant increase of σ_{hard} from RHIC to LHC, relative to σ_{soft} could then possibly explain the observed departure from N_{part} scaling.

3.5.1 Extrapolation of particle multiplicities to lower beam energies

We use the power law obtained in the previous section to "predict" the total charged- particle production as a function of the number of participants at the FAIR and NICA facilities, expected to become online in 2025. To calculate these predictions, we first remark that the shape of the N_{part} dependence of the central rapidity particle density for RHIC energies is essentially invariant with respect to $\sqrt{s_{NN}}$. To illustrate this approximate invariance, we plot multiplicity densities scaled to the corresponding multiplicity density at $\sqrt{s_{NN}} = 200$ GeV as a function of $< N_{part} >$ for several collision systems and energies in Fig 3.12. The scaling factors were determined as the ratio of multiplicity density at central rapidity measured at different beam energies $\sqrt{s_{NN}}$ to the multiplicity density observed at central rapidity in $\sqrt{s_{NN}} = 200$ GeV Au–Au collisions. These are listed for each collision system and energy in the upper panel of the figure. The scaled densities are compared to the CGC initial condition motivated fit (discussed in the next section) to the data at $\sqrt{s_{NN}} = 200$ GeV, shown as a blue dash line.

We observe from Fig 3.12 that the overlap of the data points is reasonable at energies lower than $\sqrt{s_{NN}} = 200$ GeV, which makes it possible to predict the particle densities at lower collision energies. The scaling factors are plotted as a function of $\sqrt{s_{NN}}$ in the lower panel of the figure and fitted with a polynomial shown by the red dash line. We extract the coefficients a and b, and use these to obtain scaling factors for NICA and FAIR energies. These scaling factors are used to obtain predictions of collision centrality evolution of the central particle density per participant, $dN_{ch}/d\eta|_{\eta=0}/ < N_{part} > /2$. This is shown in Fig 3.13 as a function of N_{part}.

3.5.2 Extrapolation of particle multiplicities to higher beam energies

The High-Energy Large Hadron Collider (HE-LHC) [75] and the FCC [76] accelerators proposed at CERN will achieve unprecedented large collision energies for p-p as well as heavy-ions. The expected energies for Pb-Pb collisions are 11 TeV and 39 TeV for HE-LHC and FCC, respectively. It is thus imperative to make predictions for the number of produced charged particles at such high energies. The scaling technique used to extrapolate the particle multiplicities for collision energies lower than $\sqrt{s_{NN}} = 200$ GeV is not appropriate for extending to higher energies as the approximate N_{part} scaling is broken (as per Figure 3.11). The indication of the scale breaking for multiplicity density at mid-rapidity is also evident by a closer look to upper panel of Fig 3.12 at $\sqrt{s_{NN}} = 2760$ GeV and $\sqrt{s_{NN}} = 5020$ GeV for $N_{part} > 300$. But using the power-law dependence of beam energy (Fig 3.1) for AA collisions at top 5% centrality ($= 0.77\ s_{NN}^{0.153\pm0.002}$), we can predict the charged

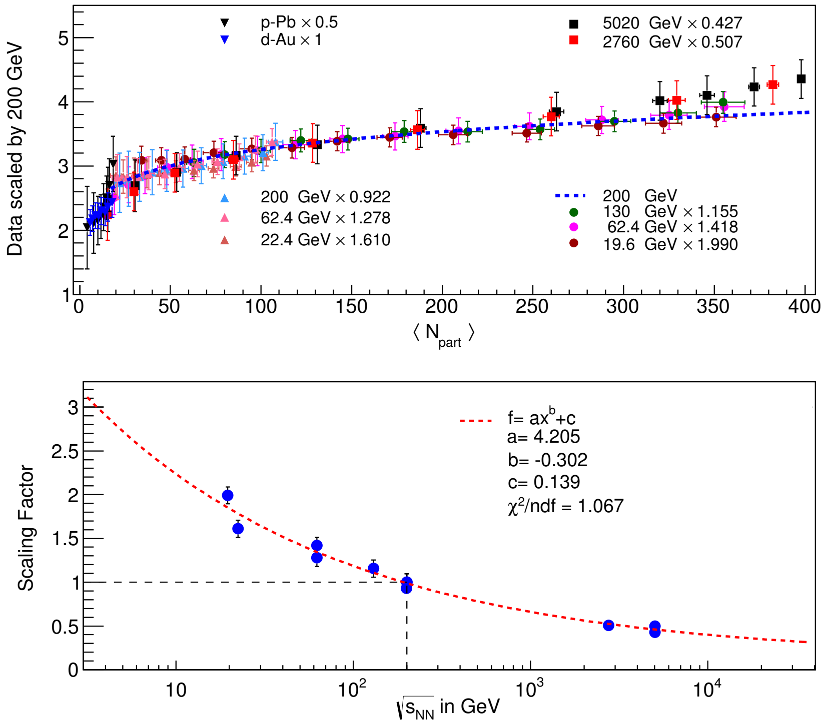

Figure 3.12: (Upper) Centrality dependence of charged-particle multiplicity density scaled to that of AuAu collisions at $\sqrt{s_{NN}}$ = 200 GeV. (Lower) Scaling factors for charged-particle multiplicity density to the data at 200 GeV.

particle multiplicity densities at mid-rapidity for Pb–Pb collisions at 11 TeV and 39 TeV. The extrapolation gives $(2/N_{part})dN_{ch}/d\eta|_{\eta=0}$ as 13.279±0.504 and 19.559 ± 0.845, respectively for top central collisions. Taking these values into account, the charged particle multiplicity density at $\eta = 0$ are $\approx 2456 \pm 93$ and $\approx 3618 \pm 156$ for 11 TeV and 39 TeV, respectively. As these higher energies probe more low-x region, one should be careful by considering the present knowledge of gluon saturation picture, which could limit the particle production in these energies and push the multiplicity towards a lower value than expected from these extrapolation.

3.6 Multiplicity density from initial condition motivated models

The collision centrality dependence of the ratio $2N_{ch}/ < N_{part} >$ is expected to be somewhat sensitive to the initial state conditions of heavy-ion collisions [79, 80]. The measured evolution of

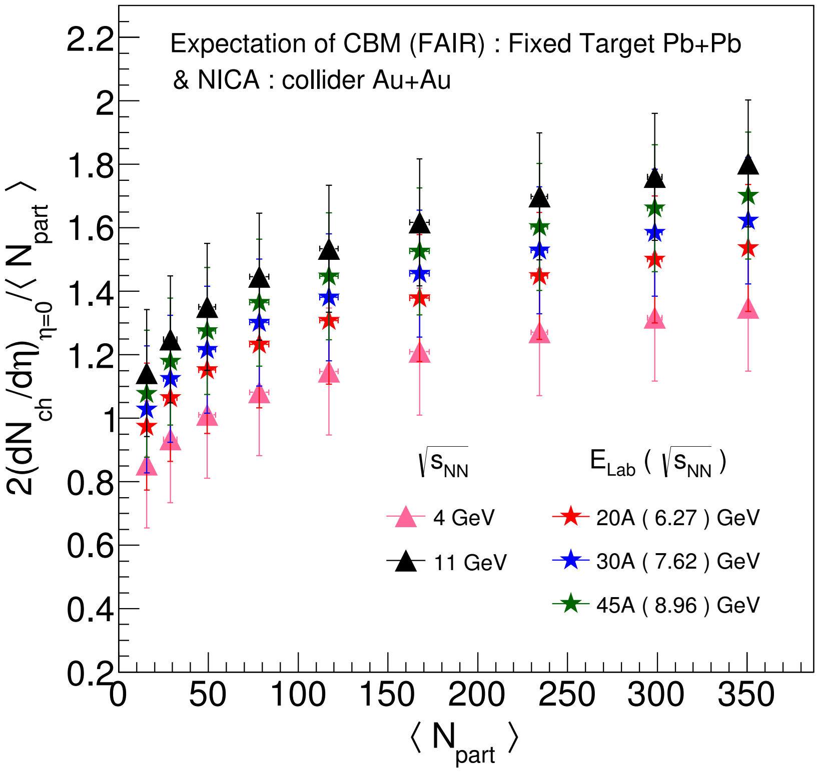

Figure 3.13: Expected evolution of charged-particle multiplicity density with centrality for CBM (FAIR) energies.

charged-particle multiplicity distributions vs. collision centrality, presented in Fig 3.14 for selected collision systems, may thus be used to contrast the predictions obtained with different models. We focus our discussion on the Glauber [52,53] and color glass condensate [79, 80] models.

Within the Glauber model, a soft/hard two-component model is used to parameterize the particle production as a function of collision centrality according to

$$\frac{dN_{ch}}{d\eta}|_{AA} = n_{pp}[(1-x)\frac{N_{part}}{2} + xN_{coll}] \tag{3.4}$$

where N_{part} and N_{coll} represent the number of soft and hard scatterings, respectively, and n_{pp} denotes the average number of produced charged particles per unit pseudorapidity in p-p collisions.

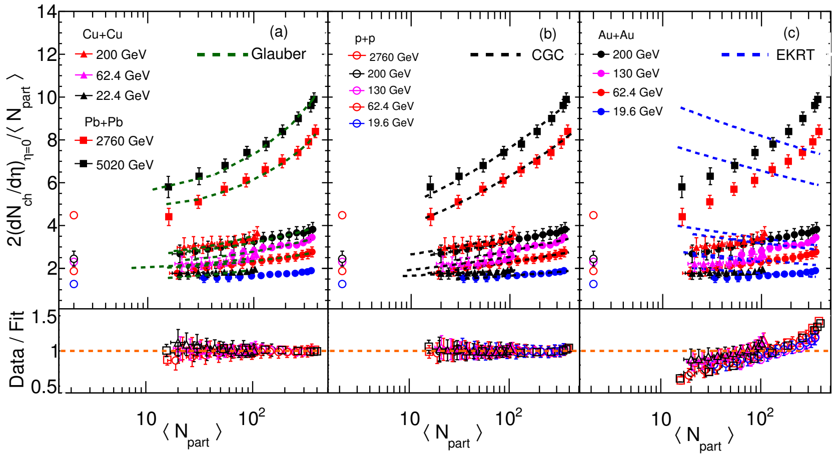

Figure 3.14: Parameterization of the N_{part} dependence of charged-particle multiplicity density per participant pair for symmetric collision systems fitted with initial conditions according to (a) Glauber, (b) CGC, and (c) EKRT models.

The variable x, representing the fraction of the hard collisions, is here considered as a fit parameter. The fit results of hard scattering component x, is within the range of 0.10 to 0.16 and in agreement with previous measurements. Panel (a) of Fig 3.14 displays fits (green dash lines) of data from Cu–Cu, Au–Au, and Pb–Pb collisions across a wide span of beam energies. To carry out the fits, we evaluated values of n_{pp} vs. $\sqrt{s}$ based on the parameterization, $n_{pp} \propto s_{NN}^{0.11}$, presented for (NSD) p–p collisions in Fig 3.1.

In the context of the Color Glass Condensate model, one expects that small x gluons overlap and recombine thereby reducing the overall number of gluons and the number of hadrons they hadronize into. The charged-particle density is hence modeled according to [19]:

$$\frac{dN_{ch}}{d\eta} \approx N_{part}^{\alpha}(\sqrt{s_{NN}})^{\gamma} \tag{3.5}$$

where α and γ are free parameters. Fits based on this model are shown in Fig 3.14 (b). By contrast, models based on final state gluon saturation, e.g., EKRT [77], predict a decreasing trend in charged-particle multiplicities per participant nucleon with increasing collision centrality according to

$$\frac{dN_{ch}}{d\eta} = C\frac{2}{3}1.16(\frac{N_{part}}{2})^{0.92}(\sqrt{s_{NN}})^{0.4} \tag{3.6}$$

where C is the only free parameter. While the Glauber and CGC initial conditions parameterizations shown in panels (a) and (b) provide excellent agreement with measured data, one finds fits based on Eq. (6), presented in Fig 3.14 (c) are in stark disagreement with the data, owing evidently to the fixed N_{part} power smaller than unity.

We extend this study to d–Au and p–Pb collision systems in Fig 3.15 using the parameterizations (4-6). We find that, in these two systems, the soft/hard two-component model and the EKRT Eq. (6) provide a relatively poor representation of the data. Overall then, we conclude the CGC

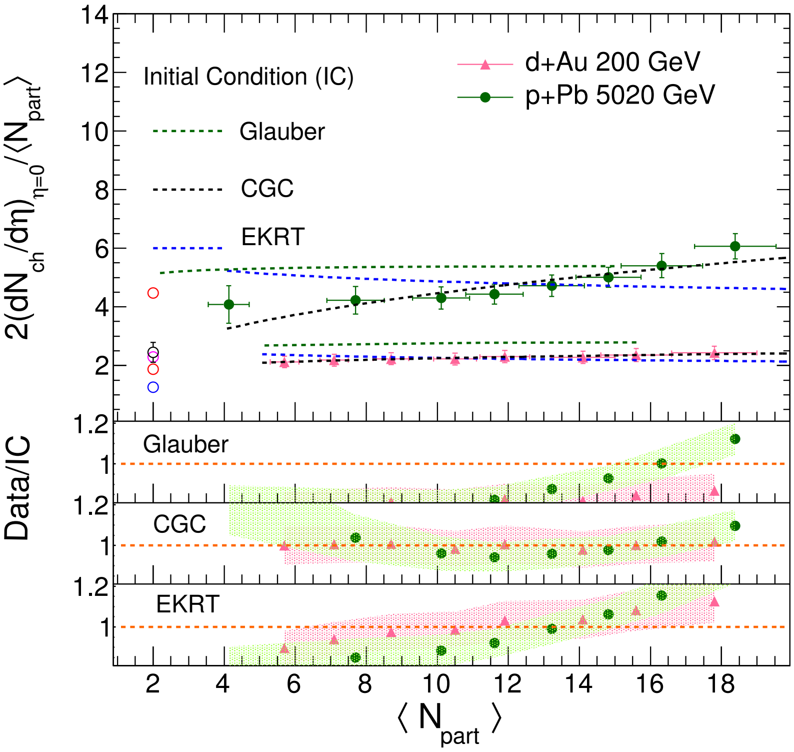

Figure 3.15: d+Au and p+Pb asymmetric collisions fitted with different initial conditions according to Glauber, CGC and EKRT models.

inspired parameterization, Eq. (5), provides a suitable description of the evolution of the charged-particle multiplicity density with N_{part} in both symmetric and asymmetric collision systems. However, we note that recent event-by-event calculations carried out using next- to-leading order EKRT model [78], with saturation for soft particle production and viscous hydrodynamics for the space-time evolution of the produced matter, can well describe the multiplicity density discussed above. In addition, the recent theoretical development on initial conditions known as TRENTO [81, 82] initial conditions also provides a successful description of the densities (as well as several other observables) in p–p, p–Pb, Au–Au, and Pb–Pb collisions both at RHIC and LHC energies.

3.7 Summary

We have presented a comprehensive study of the multiplicity and pseudorapidity distributions of the charged particles produced in p–p, p–Pb, d–Au, Cu–Cu, Au–Au, and Pb–Pb collisions at energies ranging from a few GeV to several TeV, corresponding to the available experimental data at RHIC and LHC. The experimental data have been compared to calculations of selected event generators, including PYTHIA, EPOS, AMPT, UrQMD, and THERMINATOR, which feature different physics model assumptions. We find these event generators qualitatively reproduce the observed particle densities at $|\eta| = 0$. However, none are able to satisfactorily explain the measured distributions over a broad range of pseudorapidities. With the goal of extrapolating the measured data to the forward rapidities and thereby to estimate the total charged particle production in various collision systems, and to obtain the dependence on the collision energy, we have studied three different functional forms to describe the experimental data on the pseudorapidity distributions. Among these functional forms, the difference of two Gaussian distributions, Eq. (3), is found to best reproduce the measured the multiplicity densities observed in different collision systems and collision energies.

Furthermore, we used Eq. (3) to estimate the total charged-particle production and study the evolution of multiplicity density at central rapidity ($dN_{ch}/d\eta/ < N_{part} > /2|_{\eta=0}$) as a function of collision centrality and collision energy. At beam energies $\sqrt{s_{NN}} \leq 200$ GeV, the charged-particle rapidity density exhibits a modest increase with $< N_{part} >$ while the total charge production is approximately independent of the collision centrality. In contrast, at LHC energies, both the particle density at mid-rapidity and the total charge particle production exhibit a rapid increase with $< N_{part} >$. We thus conclude that there is a qualitative change in the particle production mechanism at LHC relative to that at RHIC. At RHIC energies, the multiplicity density at mid-rapidity increases with $< N_{part} >$ while the total particle production per participant remains fixed. That implies the pseudorapidity distribution narrows with increasing N_{part} thereby yielding a larger central rapidity density albeit with a fixed integral. At the LHC, by contrast, both the central rapidity density and the total charged-particle production per $< N_{part} >$ increase with $< N_{part} >$. One then has entered a different regime of particle production in which both the central rapidity and total multiplicities per participant monotonically increase with $< N_{part} >$.

We found that the limiting fragmentation hypothesis holds at the TeV energy scale and thus can be used to approximately constrain the shape of $dN/d\eta$ distributions and their integrals over the full range of particle production. In addition, we have studied the charged-particle multiplicity productions considering different initial conditions. We observe that CGC like initial condition is best suited to describe the published data for both symmetric and asymmetric type of collisions. We have extended the particle production studies to the lower collision energies corresponding to those of upcoming accelerator facilities of FAIR at GSI, Darmstadt and NICA at JINR Dubna. We have extrapolated the charged particle multiplicity densities at $\eta = 0$ for expected heavy-ion collisions at the proposed HE-LHC and FCC at CERN.

Bibliography

[1] A. Biallas, M. Bleszynski, and W. Czyz, Nucl. Phys. B 111, 461 (1976).

[2] J. D. Bjorken, Phys. Rev. D 27, 140 (1983).

[3] D. Kharzeev and M. Nardi, Phys. Lett. B 507, 121 (2001).

[4] J.F. Grosse-Oetringhaus and K. Reygers, J. Phys. G: Nucl. Part. Phys. 37, 083001 (2010).

[5] B. Alver et al. [PHOBOS Collaboration],Phys. Rev. C 83 (2011) 024913.

[6] L. Adamczyk et al. (STAR Collaboration) Phys. Rev. C 96, 044904 (2017).

[7] A. Toia et al. (ALICE Collaboration) J. Phys. G 38, 124007 (2011).

[8] R. Sahoo, A. N. Mishra, N. K. Behera and B. K. Nandi, Adv. high-energy Phys. 2015, 612390 (2015).

[9] E. K. G. Sarkisyan, A. N. Mishra, R. Sahoo and A. S. Sakharov, Phys. Rev. D 93, 054046 (2016).

[10] S. Basu, T.K. Nayak, K. Datta, Phys. Rev. C 93, 064902 (2016).

[11] Torbjorn Sjostrand, Stephen Mrenna, and Peter Skands, J. High Energy Phys. 05, 026 (2006).

[12] G.Corcella et. al. Jour. High Ener. Physics. 01 (2001)010.

[13] J. Adams et al. (STAR Collaboration) Nucl. Phys. A 757, 102 (2005).

[14] U. W. Heinz and M. Jacob, arXiv:nucl-th/0002042 [nucl-th].

[15] L. McLerran, J. Dunlop, D. Morrison, R. Venugopalan, Nucl. Phys. A 854 (2011) 1.

[16] E. Iancu, K. Itakura, L. McLerran, Nucl. Phys. A 708 (2002) 327.

[17] E. Iancu, L. McLerran, Phys. Lett. B 510 (2001) 145.

[18] Jamal Jalilian-Marian Phys. Rev. C 70, 027902 (2004).

[19] D. Kharzeev and E. Levin, Phys. Lett. B 523, 79 (2001).

[20] K. Dusling and R. Venugopalan, Phys. Rev. Lett. 108 (2012) 262001.

[21] F.O. Duraes, A.V. Giannini, V.p. Goucalves and F.S. Navarra, Phys. Rev. C 94, 024917 (2016).

[22] T. Lappi, H. Mantysaari, Nucl. Phys. A 926, 186 (2014).

[23] A. H. Rezaeian, Phys. Lett. B 727, 218 (2013).

[24] M. Derrick et al. (ZEUS Collaboration) Phys. Lett. B 345 (1995) 576.

[25] C. Adlof et al. (H1 Collaboration), Phys. Lett. B 520 (2001) 183.

[26] J. Benecke, T. T. Chou, C. N. Yang and E. Yen, Phys. Rev. 188, 2159 (1969).

[27] R. Beckmann, S. Raha, N. Stelte, R.M. Weiner, Phys. Lett. B105, 411 (1981).

[28] F. Gelis, A.N. Stasto, R. Venugopalan, Eur. Phys. J. C 48, 489 (2006).

[29] B. Alver et al. (PHOBOS Collaboration) Phys. Rev. C 94, 024903 (2016).

[30] G. Torrieri, EPJ Web of Conferences, 04002 (2011).

[31] S. Acharya et al. (ALICE Collaboration) arXiv:1805.04432 [nucl-ex].

[32] J. Adam et al. (ALICE Collaboration) Phys. Lett B 772, 567 (2017).

[33] L. D. McLerran, Raju Venugopalan, Phys. Rev. D 49 (1994) 2233.

[34] M. Bleicher et al.,, Phys. Lett. B 435, 9 (1998).

[35] M. Bleicher, S. Jeon, V. Koch, Phys. Rev. C 62, 061902(R) (2000)

[36] S. Haussler, H. Stocker and M. Bleicher, Phys. Rev. C 73, 021901(R) (2006).

[37] A. Chatterjee, S. Chatterjee, T. K. Nayak, N. R. Sahoo, J. Phys. G: Nucl. Phys. J. Phys. 43, 125103 (2016)

[38] Z.-W. Lin et al. Phys. Rev. C 72, 064901 (2005).

[39] Z.-W. Lin et al., Phys. Rev. C 64, 011902 (2001).

[40] B. Zhang et al., Phys. Rev. C 61, 067901 (2000).

[41] A.G. Knospe et al. Phys. Rev. C 93, 014911 (2016).

[42] K. Werner et al., Phys. Rev. C 89, 064903 (2014).

[43] K. Werner, Phys. Rev. Lett. 98, 152301 (2007).

[44] K. Werner et al., Phys. Rev. C 82, 044904 (2010).

[45] M. Nahrgang et al., Phys. Rev. C 90, 024907 (2014).

[46] M. Chojnacki, A. Kisiel, W. Florkowski and W. Broniowski, Comput. Phys. Commun. 183 (2012) 746.

[47] K. Aamodt et al. [ALICE Collaboration], Eur. Phys. J. C 68 (2010) 89.

[48] J. Adam et al. [ALICE Collaboration], Eur. Phys. J. C 77 (2017) no.1, 33.

[49] J. Adam et al. [ALICE Collaboration], Phys. Lett. B 753 (2016) 319.

[50] F. Abe et al. [CDF Collaboration], Phys. Rev. D 41 (1990) 2330.

[51] K. Alpgard et al. [UA5 Collaboration] Phys. Lett.B 112 (1982) 183, G. J. Alner et al. [UA5 Collaboration] Phys. Rept.154 (1987) 247.

[52] B. I. Abelev et al. [STAR Collaboration], Phys. Rev. C 79 (2009) 034909.

[53] B. Alver et al. [PHOBOS Collaboration], Phys. Rev. Lett. 102 (2009) 142301.

[54] B. B. Back et al. [PHOBOS Collaboration], Phys. Rev. C 74 (2006) 021901.

[55] B. Alver et al. [PHOBOS Collaboration], Phys. Rev. C 83 (2011) 024913

[56] B. B. Back et al. [PHOBOS Collaboration], Phys. Rev. Lett. 87 (2001) 102303

[57] B. B. Back et al. [PHOBOS Collaboration], Phys. Rev. Lett. 91 (2003) 052303

[58] E. Abbas et al. [ALICE Collaboration], Phys. Lett. B 726 (2013) 610.

[59] J. Adam et al. [ALICE Collaboration], Phys. Lett. B 772 (2017) 567.

[60] J. Adam et al. [ALICE Collaboration], Phys. Rev. Lett. 116 (2016) 222302.

[61] B. B. Back et al. [PHOBOS Collaboration], Phys. Rev. C 72 (2005) 031901

[62] G. Aad et al. [ATLAS Collaboration], Eur. Phys. J. C 76 (2016) no.4, 199

[63] B. Abelev et al. [ALICE Collaboration], Phys. Rev. Lett. 110 (2013) no.3, 032301

[64] J. Adam et al. [ALICE Collaboration], Phys. Rev. C 91 (2015) no.6, 064905.

[65] R. Brun and F. Rademakers, Nucl. Inst. and Meth. in Phys. Res. A 389 (1997) 81.

[66] A. Krasnitz and R. Venugopalan, Nucl. Phys. A 698 (2002) 209.

[67] B. Kellers, G. Wolschin, Prog. Theor. Exp. Phys. 2019 (2019) 053D03.

[68] K. J. Goncalves, A. V. Giannini, D. D. Chinellato and G. Torrieri, Phys. Rev. C 100 (2019) 054901.

[69] P. Sahoo, P. Pareek, S. K. Tiwari and R. Sahoo, Phys. Rev. C 99 (2019) 044906.

[70] J. Adam et al. [ALICE Collaboration], ‘Phys. Lett. B 754 (2016), 373.

[71] B. B. Back et al. [PHOBOS], Phys. Rev. C 74 (2006), 021902.

[72] V. Khachatryan et al.[CMS Collaboration] Jour. High Ene. Phys. 1002 (2010) 041.

[73] G. Wolschin, Phys. Rev. C 91, 014905 (2015).

[74] L. A. Harland-Lang, A. D. Martin, P. Motylinski, and R.S. Thorne, Eur.Phys.J. C 75 (2015) no.5, 204

[75] A. Abada et al. [FCC Collaboration], Eur. Phys. J. Special Topics 228 (2019) 1109.

[76] A. Dainese et al. PoS HardProbes2018 (2019) 005 (e-Print: 1901.10952 [hep-ph]).

[77] K. J. Eskola, K. Kajantie, P. V. Ruuskanen, and K.Tuominen, Nucl. Phys. B 570, 379 (2000).

[78] K. J. Eskola, H. Niemi and R. Paatelainen, Nucl. and Part. Phys. Proc., 276-278 (2016) 161.

[79] J.L. Albacete, C. Marquet, Progress in Particle and Nuclear Physics 76, 1 (2014).

[80] J. L. Albacete, A. Dumitru, Y. Nara, J. Phys.: Conf. Ser. 316, 012011 (2011).

[81] J. Scott Moreland, Jonah E. Bernhard, and Steffen A. Bass, Phys. Rev. C 92 (2015) 011901.

[82] C. Shen et al. Comput. Phys. Commun. 199 (2016) 61.

Chapter 4

Two-particle correlation in ALICE: Analysis details and results

4.1 Analysis Details:

In the analysis presented in this thesis, two particle correlation function is constructed using pion and proton as trigger particles in the transverse momentum range ($2 < p_T < 4$) GeV/c and charged hadrons as associated particles in the range ($1 < p_T < 4$) GeV/c produced in Pb-Pb collisions at $\sqrt{s_{NN}} = 5.02$ TeV. Pions and protons are identified using TPC and TOF detectors. Efficiency and purity factors are estimated using Monte-Carlo simulation to correct the correlation functions and a closure test has been performed to check the reliability of the estimated correction factors. After that, the near-side yield is calculated as a function of centrality with the statistical and systematic uncertainties and compared with the model calculations.

4.1.1 Data sample

There are two types of data files in ALICE - ESD (Event Summary Data) and AOD (Analysis Object Data). The ESD contains the events consisting of information from all the subdetectors. The AOD contains subset of ESD information that have been selected for analysis. System: Pb-Pb $\sqrt{s_{NN}} = 5.02$ TeV

Total number of events analysed: $\sim$ 400M

Data: LHC15o , pass1, AOD194

MC: LHc16g1 HIJING,AOD188

4.1.2 Event selection

The primary task of an trigger is to select the beam collision events and reject the interactions of the beam with residual gas in the beam pipe. In this analysis, kINT7 trigger is used which is a minimum bias trigger that requires hit in both the V0A and V0C detectors. The interaction point is set up at (0,0,0) and the point at which the actual collision occurs between the two beams is called the vertex of the event. The length of the interaction diamond is 10 cm i.e. ±10 cm around the nominal interaction point along the beam direction. The z-component of vertex shows a gaussian distribution around z=0 whereas, the x and y-components show sharp delta distribution around 0. Z-vertex cut $|V_Z| < 7$ cm has been used in this analysis to minimize the edge effect. To study the multiplicity dependence of per triggered yield, a selection is used to divide the events into event classes 0-10%, 10-20%, 20-40%, 40-60% and 60-80% , where 0-10% means the multiplicity corresponding to 10% of the total events. As discussed earlier, centrality is estimated from the multiplicity distribution obtained from V0 detector (V0A+V0C). For systematic study, $|V_Z| < 5$ cm and $|V_Z| < 9$ cm have been used.

4.1.3 Track selection

This analysis is performed on AOD dataset mentioned above with the Filter Bit 768 (means that the global tracks with TPC+ITS with requirement of one point in SPD is satisfied) as default. A Filter Bit defines a set of cuts that the tracks must satisfy which is used mainly to select primary particles with uniform azimuthal angle distribution (ϕ). It includes cuts like the detector requirements for a track to pass through, distance of closest approach (DCA) of a reconstructed track to the primary vertex, number of points in TPC among others. For systematics error, filter bit 96 (global tracks with stricter DCA) and filter bit 1 (tracks passing through TPC only) are used. Additional cuts used are $|\eta|$ <0.8, p_T >0.2 GeV/c. Pions and Protons with $2 < p_T <$ 4 GeV/c have been identified using TPC and TOF as trigger particles and unidentifid charged hadrons with $1.0 < p_T < p_{T,trig}$ GeV/c are selected as associated particles. In many of the Run-2 data a large fraction of the recorded events has more than one collision within the TPC readout time. Hence, removal of events with pileup results in a dramatic loss of statistics. Cleanup should therefore be based on track selection cuts, i.e. the tracks coming from the pileup collisions should be removed and only the ones from the collision that fired the trigger should be kept. So, a track-based out-of-bunch pileup cut is used to reject tracks from the pile up events. A track is accepted if it passes the ITS refit condition and if it has points on the ITS layers 0 or 1 and it requires a matching hit on TOF.

There are two types of pile up. In the "Same Bunch" pile up, two or more collisions occur in the same bunch crossing and in "Out of Bunch" pile up, one or more collisions occur in bunch crossings which is different from the one that triggered the acquisition. The detectors are affected differently depending on their readout time. Integration time of SPD $\sim$ 300 ns, TOF $\sim$ 0.5 μs, SSD $\sim$ 1 us and other detectors have much larger integration time. SPD (the first two layers of ITS) hit requirement allows to remove out-of-bunch pileup from the neighbouring bunches outside the SPD readout time (300 ns) , but it does not help within SPD integration time window. Time information of TOF allows (for tracks matched to the TOF) to identify the bunch crossing in which the particle was produced.

Track parameters	Cut values
p_T	> 0.2 GeV/c
$\lvert\eta\rvert$	< 0.8
DCA to primary vertex DCA_{xy} (DCA_z)	$<$ 2.4 cm (3.2 cm)
ITS refit	Yes
TPC refit	Yes

4.1.4 Particle identification

Trigger particles with 2< p_T <4 GeV/c are identified using TPC and TOF. It is based on a combined "number of sigmas (nσ)" method, where σ is the standard deviation from Bethe-Bloch of dE/dx energy loss signal of a track in TPC or the time-of-flight deviation of a track from its expected arrival time in TOF.

$N_{\sigma,TPC,\pi,p} = (< dE/dx > |_{\pi,p,expec} - < dE/dx > |_{track}) \ / \ \sigma$ & $N_{\sigma,TOF,\pi,p} = (< t_{TOF} > |_{\pi,p,expec} - < t_{TOF} > |_{track}) \ / \ \sigma$ So, the combined $N\sigma$ is $N^2_{\sigma,PID} = N^2_{\sigma,TPC} + N^2_{\sigma,TOF}$. For a particular species, tracks within the 2σ circular cut is assigned with an identity of that particular species.

For identifying tracks, if a track is recognized by PID $n\sigma$ cut as three different particles (i.e.pion, kaon and protons), comparison is made among the three and only the track with smallest $n\sigma$ is chosen as the trigger particle. Tracks are ensured to have not been double counted. For systematic error estimation, the cut is changed to $N_{\sigma,PID}$ <3.

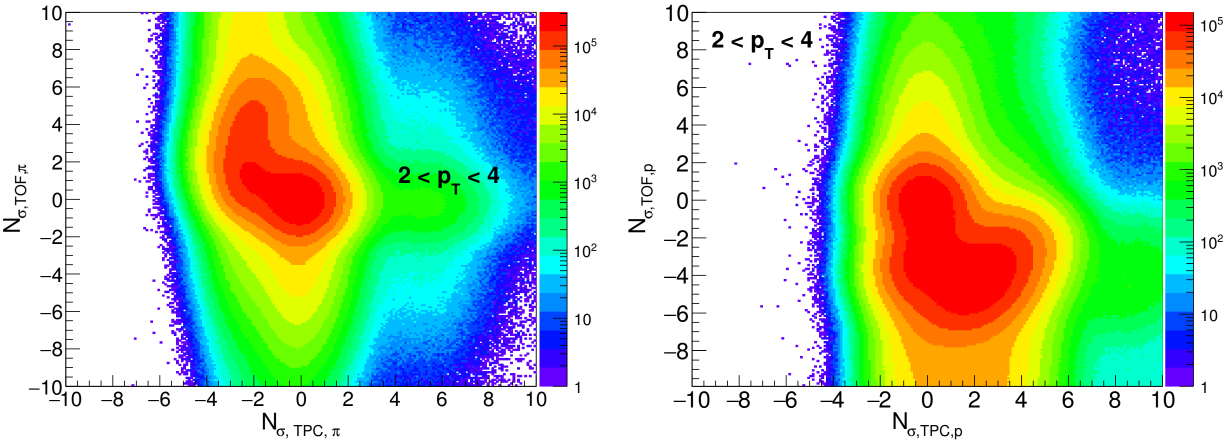

Figure 4.1: Particle Identification using $n\sigma$ method

4.1.5 Correlation function

Two particle correlation between pairs of trigger and associated hadrons in $\Delta\eta$-$\Delta\phi$ space is defined as, $C(\Delta\eta, \Delta\phi) = \frac{1}{N_{trig}}\frac{d^2N_{assoc}}{d\Delta\eta d\Delta\phi} = \alpha\frac{S(\Delta\eta,\Delta\phi)}{B(\Delta\eta,\Delta\phi)}$, where α is the normalization factor, N_{assoc} is the number of particles associated with N_{trig} number of trigger particles for a particular event, $\Delta\eta$=$\eta_{trig} - \eta_{assoc}$ and $\Delta\phi$=$\phi_{trig} - \phi_{assoc}$. p_T ordering ($p_{T,asso} < p_{T,trig}$) has been used to avoid double counting in case of overlapping p_T region of triggers and associated particles. It also ensures $p_{T,trig}$ as the possible leading particle. The signal S$(\Delta\eta, \Delta\phi) = \frac{1}{N_{trig}}\frac{d^2N_{same}}{d\Delta\eta d\Delta\phi}$ is constructed by taking triggers and associated particles from the same event and the background B$(\Delta\eta, \Delta\phi) = \frac{d^2N_{mixed}}{d\Delta\eta d\Delta\phi}$ is constructed by taking triggers from one event and associated particles from other events of similar multiplicity and Z-vertex classes of triggers. The same event contains true physics correlation as well as correlation due to the finite detector acceptance. The second component comes due to the finite acceptance of the detector in η and peak at $\eta \approx 0$ as the probability of reconstructing pairs in small $\Delta\eta$ is maximum. B$(\Delta\eta, \Delta\phi)$, by construction, should not contain any physics correlation. So, to remove the detector acceptance effect, mixed event method is used. The procedure is as follows. For events to be mixed and to form a mixed event, the Z-vertex of bin width 2 cm and multiplicity of variable bin width are chosen. A pool is created of such mixed events as a function of centrality and Z-vertex. The maximum number of events in a pool can be 1000 and it can have a maximum of 50000 tracks. Whenever a real event appears, the pool is updated with the tracks. The pool is ready when it contains 10% of the maximum number of tracks, or has at least 5 events in it. When the new event pushes the number of tracks higher than the limit, the oldest event are deleted. In mixed event, correlations due to physics effects are removed by construction, although correlations due to detector acceptance are still present. We divide the Signal by mixed event to extract the true physics correlation. The mixed event correlation or background is normalized with α = B(0,0) such that B(0,0) is unity, as it has maximum detector acceptance. The same event and mixed event correlations are shown in Fig.4.2. By dividing the same event with the mixed event, the true correlation functions are constructed as shown in Fig.4.3 and Fig.4.4. Depending on detector resolution, track density, charge of track, momentum, magnetic field, if two tracks come close to each other where their angular separation is less than the spatial resolution of TPC, then they cannot be identified as two distinct tracks. The probability of counting them as a single track instead of a pair is higher in small $\Delta\eta$,$\Delta\phi$. Thus the probalility of losing that pair in correlation function is also higher in that region resulting in an artificial dip at $\Delta\eta \approx 0$,$\Delta\phi \approx 0$. This is called track merging and it is corrected by applying a two-track efficiency cut on both same event and mixed event. Only the track pairs separated by $|\Delta\eta| > 0.02$ and $|\Delta\phi^*| > 0.02$ are taken to correct for the track merging effect, where $|\Delta\phi^*$, the azimuthal separation between two tracks in at the same radius r within detector volume, is given by, $|\Delta\phi^*| = |\Delta\phi| - q_1 * B * Sin^{-1}(0.075 * r/p_{T,1}) + q_2 * B * Sin^{-1}(0.075 * r/p_{T,2})$, r varies from 0.8 m to 2.5 m in steps of 1 cm. After track merging correction, a dip arises in $\Delta\eta, \Delta\phi$=0,0 due to track removal in this region. So, the mixed event normalization need to be modified. The background is normalized by a factor α such that it is unity at the away side region ($\Delta\eta$ =0,$\Delta\phi = \pi$).

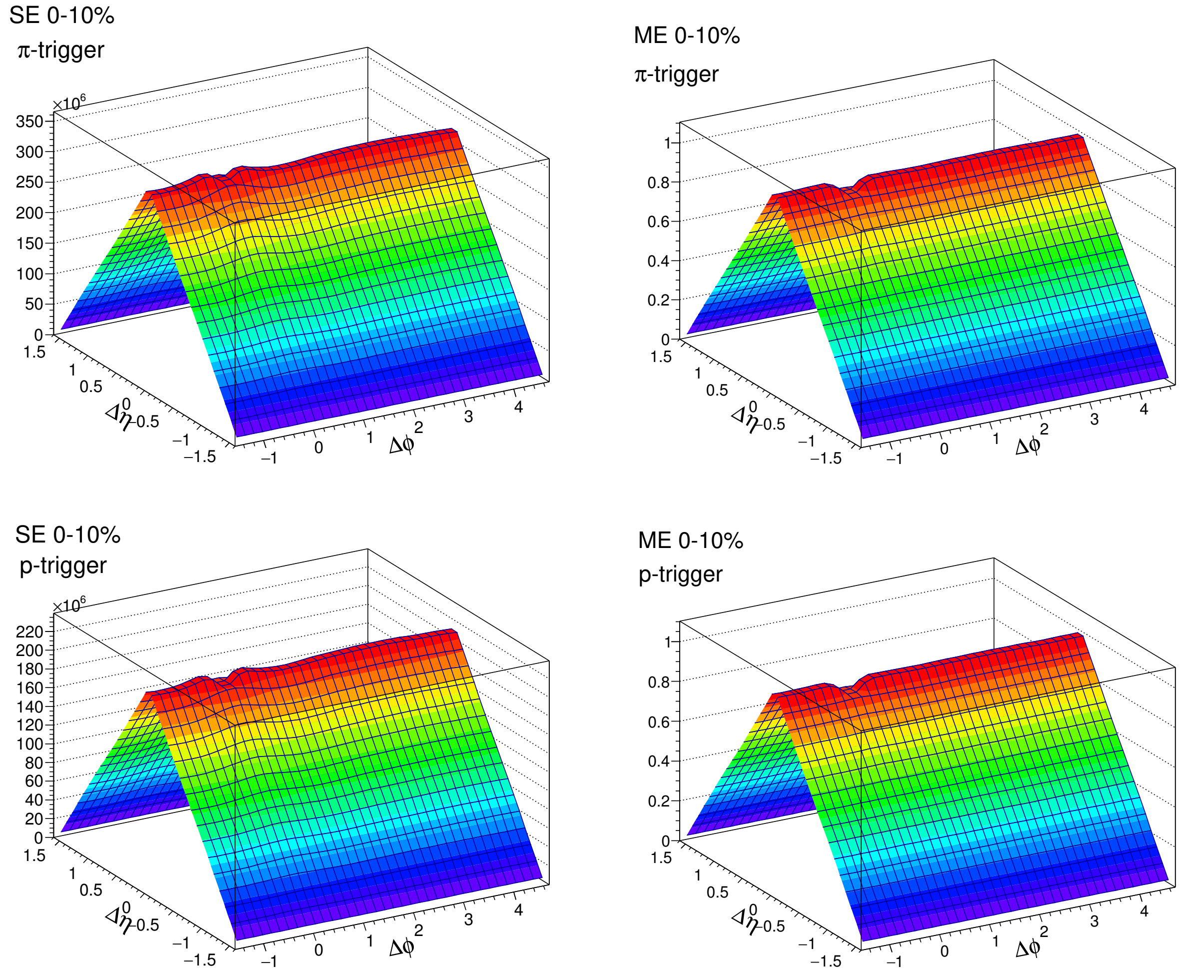

SE 0-10% π-trigger

ME 0-10% π-trigger

SE 0-10% p-trigger

ME 0-10% p-trigger

Figure 4.2: Same Event (SE) and Mixed Event (ME) correlation functions with pions and protons used as trigger for 0-10% centrality in Pb-Pb collision at $\sqrt{s_{NN}} = 5.02$ TeV. The Z-axis represents the number of particles associated to the trigger particle.

4.2 Corrections

The mixed event technique corrects for the pair acceptance partially due to the finite reconstruction efficiency of the detector. The measured correlation functions are not the actual ones because of many factors. A detector cannot detect all the particles incident on it because of the detector geometry, momentum of the tracks etc. Low momentum tracks bend more, thus they cannot reach the outer part of TPC and the high momentum tracks bend less, so they can be affected by the dead areas of TPC, thereby resulting a detector efficiency < 1 . Also, in real data, we cannot recognize

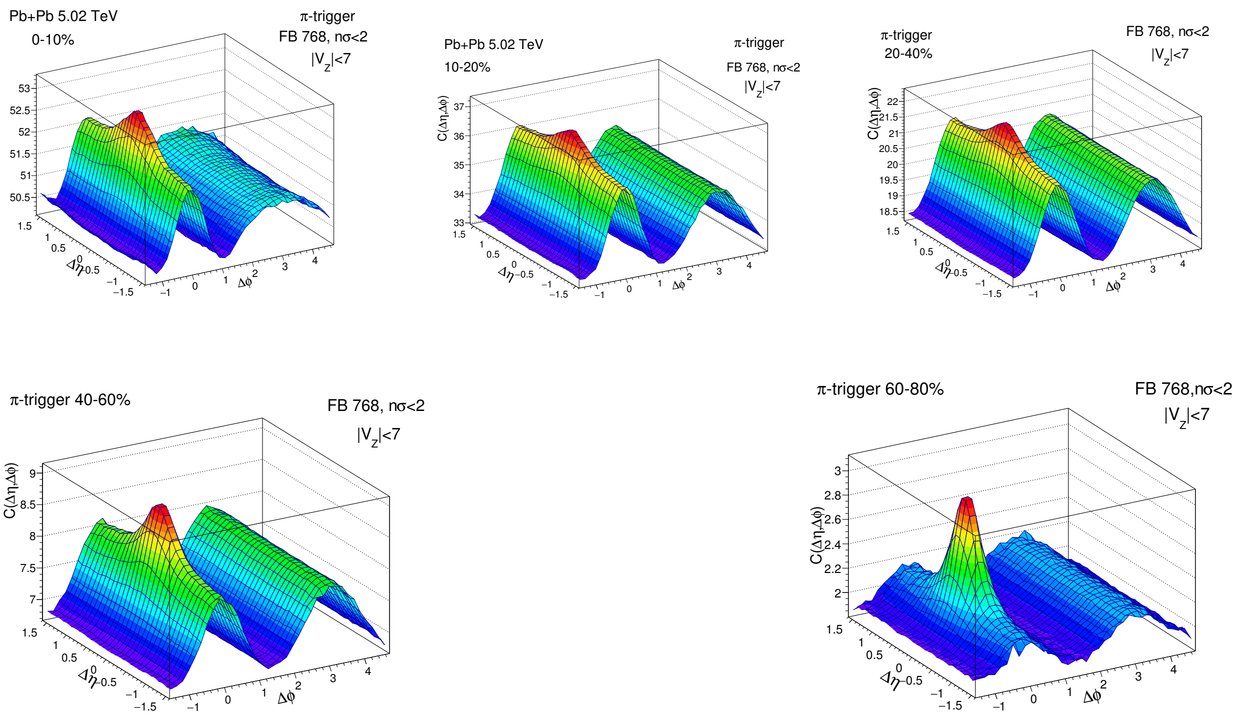

Figure 4.3: Pion triggered correlation function (efficiency corrected) for five centrality classes. The Z-axis represents the per triggered associated yields after mixed event correction.

a track as a pure primary track which is needed in the analysis. Apart from that, a track identified as pion or proton may not be a pure pion or proton due the particle identification procedure. A kaon can also be misidentified as a pion or proton. Therefore, its purity should be determined. Also, the particle identification procedure itself cannot be 100% efficient. So, it is needed to take all these factors into consideration. On the other hand, in Monte carlo simulation, all the particles have pre-defined different particle identification codes which helps to separate them from each other accurately, also they can be identified as primary or secondary particles accurately. Therefore, to correct for this, same analysis procedure is performed on the Monte-Carlo data, where the particles generated by an event generator have been reconstructed by passing through the simulated detector response (detector geometry and electronics read-out) and compared with the true Monte-Carlo particles where no detector response is present. The reconstructed events are similar to the actual collisions in ALICE. Ratio of these two (reconstructed and true MC events)

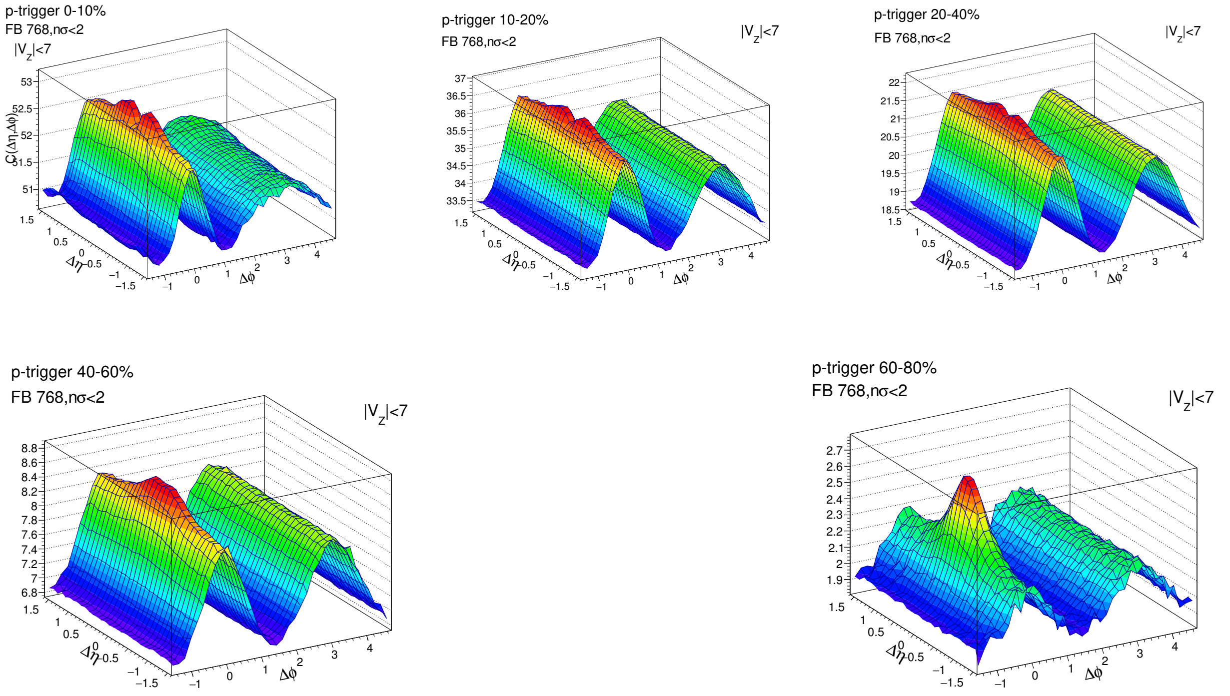

Figure 4.4: Proton triggered correlation function (efficiency corrected) for five centrality classes. The Z-axis represents the per triggered associated yields after mixed event correction

gives the reconstruction efficiency. The efficiencies are calculated as a function of η, p_T, and V_Z.

4.2.1 Tracking efficiency

The tracking efficiency measures the fraction of the number of tracks a detector can reconstruct out of all the particles incident on it. MC-particle identification code of the particles is checked for each case. Tracking efficiency of charged hadrons is defined as, $\epsilon_{tracking,h} = \frac{Number\ of\ accepted\ reconstructed\ primaries\ after\ passing\ through\ detector}{Number\ of\ generated\ primaries}$

Tracking efficiency of identified particles is defined as,

$$\epsilon_{tracking,\pi,p} = \frac{Number\ of\ all\ reconstructed\ primary\ \pi,p\ after\ passing\ through\ detector}{Number\ of\ generated\ primary\ \pi,p}$$

Fig.4.5 shows the tracking efficiencies of hadrons, pions and protons as a function of p_T, η, V_Z.

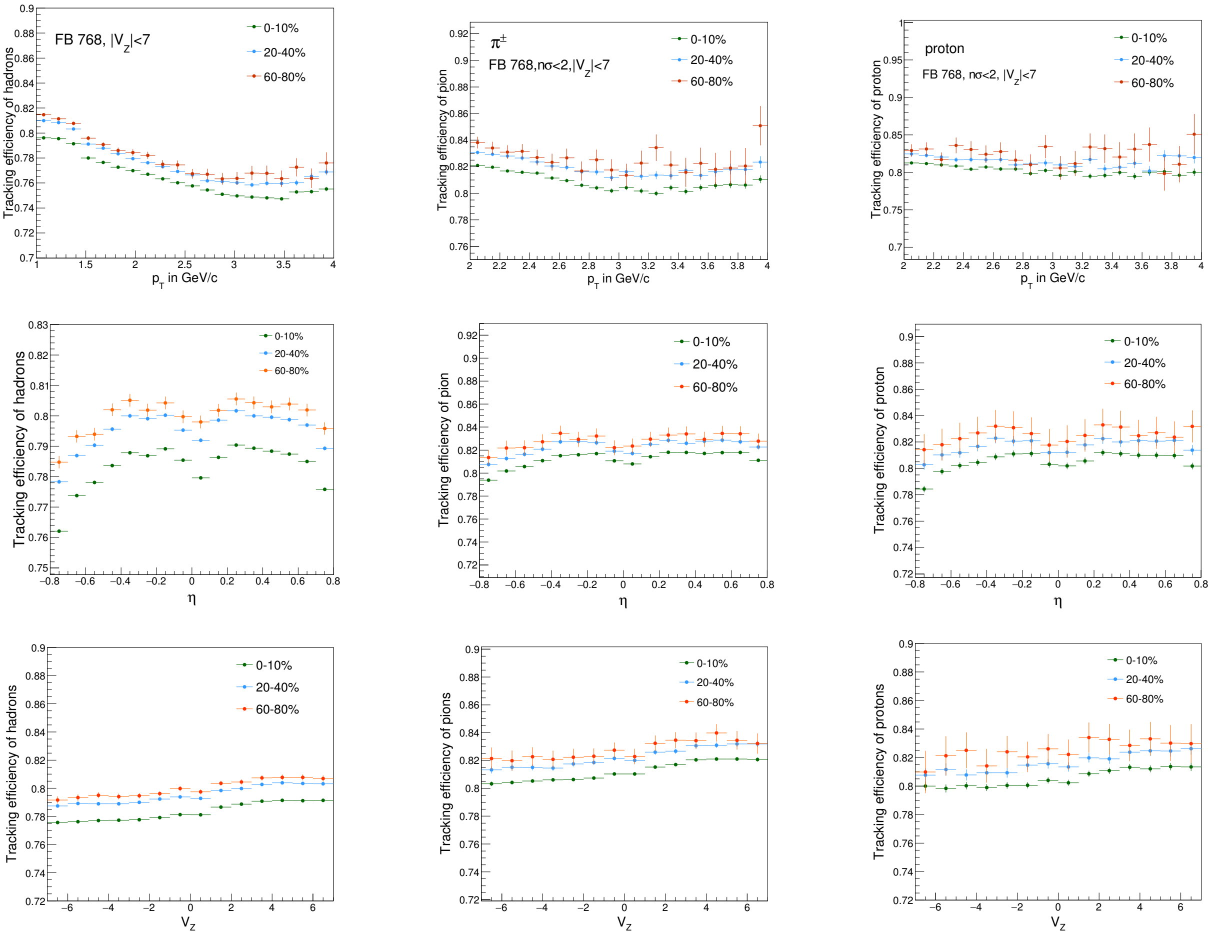

Figure 4.5: Tracking efficiency of hadrons, pions and protons as a function of p_T, η, V_Z with default cuts.

Tracking efficiency is mostly flat with V_Z and p_T, though it slightly decreases with p_T for charged hadrons. The efficiency is marginally lower in the central region of the detector compared to its outer edges. This can be due to less number of TPC clusters. Number of tracks satisfying the selection criteria is relatively less in the central region than the outer edges of the detector. However, there is no significant centrality dependence of this factor.

4.2.2 Contamination

The fraction of the non-primary particles in the sample of accepted primary tracks (from the weak decay of another particle or from the interaction with the material of the detector) is called the

Contamination and defined as, Contamination from secondary hadrons,

$$C_h = \frac{Number\ of\ reconstructed\ secondaries}{Number\ of\ reconstructed\ primaries{+}secondaries}$$

Contamination from secondary identified particles,

$$C_{\pi,p} = \frac{Number\ of\ reconstructed\ secondary\ \pi{,}p}{Number\ of\ reconstructed\ primary\ \pi{,}p{+}secondary\ \pi{,}p}$$

Fig.4.6 shows the contamination from secondary hadrons, pions and protons as a function of p_T, η, V_Z. Contamination in the sample have been estimated by checking at the MC generated level. The contamination is seen to decrease with increase in p_T, whereas, it is almost flat with η and V_Z. The factors are almost independent of centrality.

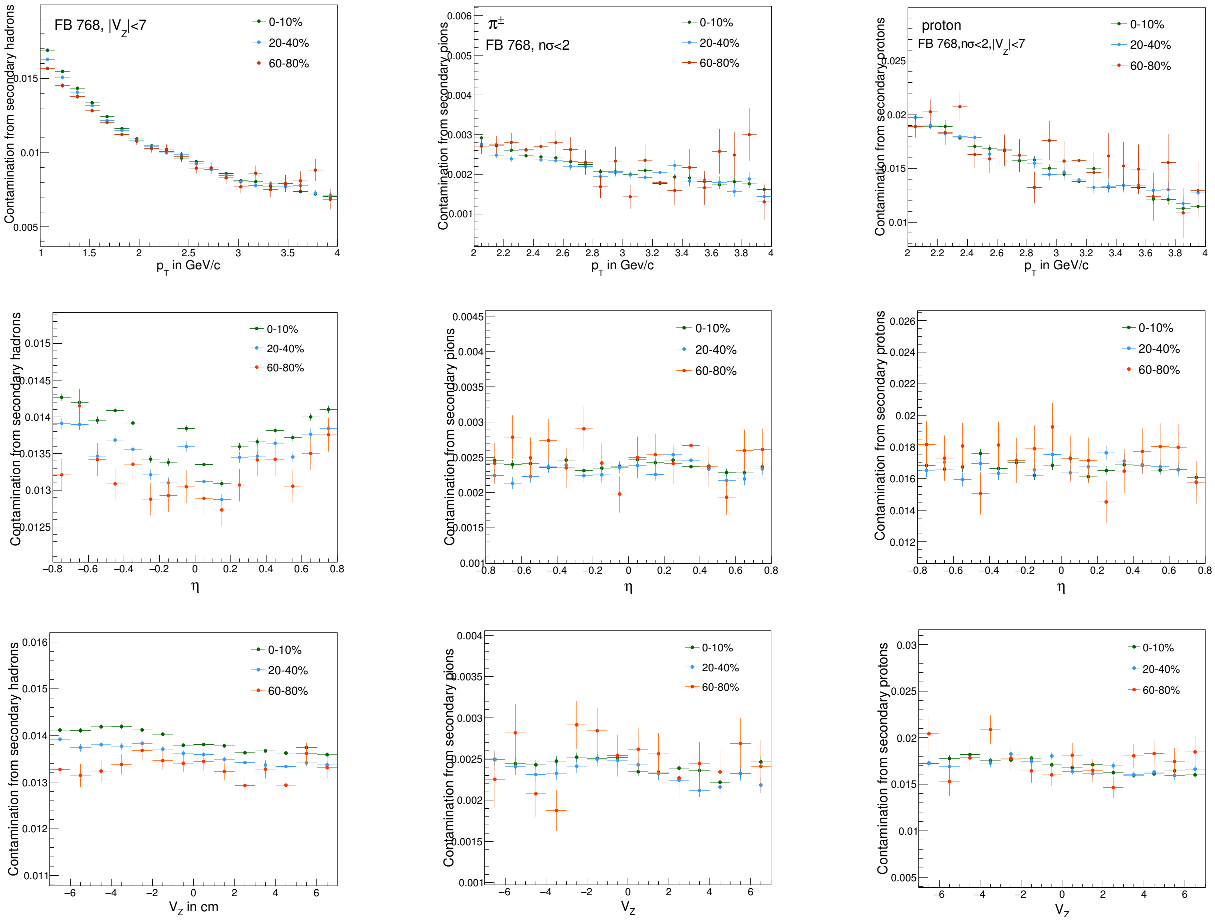

Figure 4.6: Secondary contamination factors of hadrons, pions and protons as a function of p_T, η, V_Z with default cuts

4.2.3 PID efficiency

How much efficiently the PID procedure can identify the tracks is given by the Particle Identification (PID) efficiency. PID efficiency is defined as, $\epsilon_{PID} = \frac{Number\ of\ reco\ primaries\ after\ n\sigma\ cut}{Number\ of\ reco\ primaries\ without\ n\sigma\ cut}$

Total efficiency $\epsilon_{Tot} = \epsilon_{PID} * \epsilon_{tracking} = \frac{Number\ of\ reco\ primaries\ after\ n\sigma\ cut}{Number\ of\ generated\ primaries}$

Fig.4.7 and Fig.4.8 show the PID efficiency and total efficiency of identified particles respectively with respect to η, p_T & V_Z. PID efficiency and total efficiency are seen to be almost flat with p_T and V_Z, however, there is a dip in the efficiency values around η=0 which can be due to the absence of some modules in TOF during the data taking.

4.2.4 Purity

In the particle identification process, some particles will be misidentified as different species and this will affect the purity of the sample. Suppose, we want to detect the actual number of "A" particle from a sample which consists of all "A" like particles. The purity P is defined as, $P = \frac{Number\ of\ true\ A{-}particles\ in\ the\ A{-}like\ sample(n\sigma<2)}{Number\ of\ all\ particles\ in\ A{-}like\ sample(n\sigma<2)}$

Purity of pion and proton with p_T have been shown in Fig.4.9. The purity of pions is almost same ($> 94\%$) for all p_T, whereas, the purity of protons drops from 95% to 60% as it approaches $p_T =$ 4 GeV/c. The drop in proton purity is under further investigation. The purity is independent of centrality. If the PID eficiency increases, the purity decreases and vice versa. The best possible PID efficiency to Purity ratio is to be chosen.

4.2.5 Correction Factor

The correction factor for the unidentified associate particles is, $f_{assoc} = \frac{1-C_h}{\epsilon_{tracking,h}}$ and for identified trigger particles is- $f_{trig} = \frac{1-C_{\pi,p}}{\epsilon_{tracking,\pi,p}} * \frac{Purity}{\epsilon_{PID}}$

where, C_h & ϵ_h are the contamination factors and tracking efficiency for charged hadrons, $C_{\pi,p}$ &

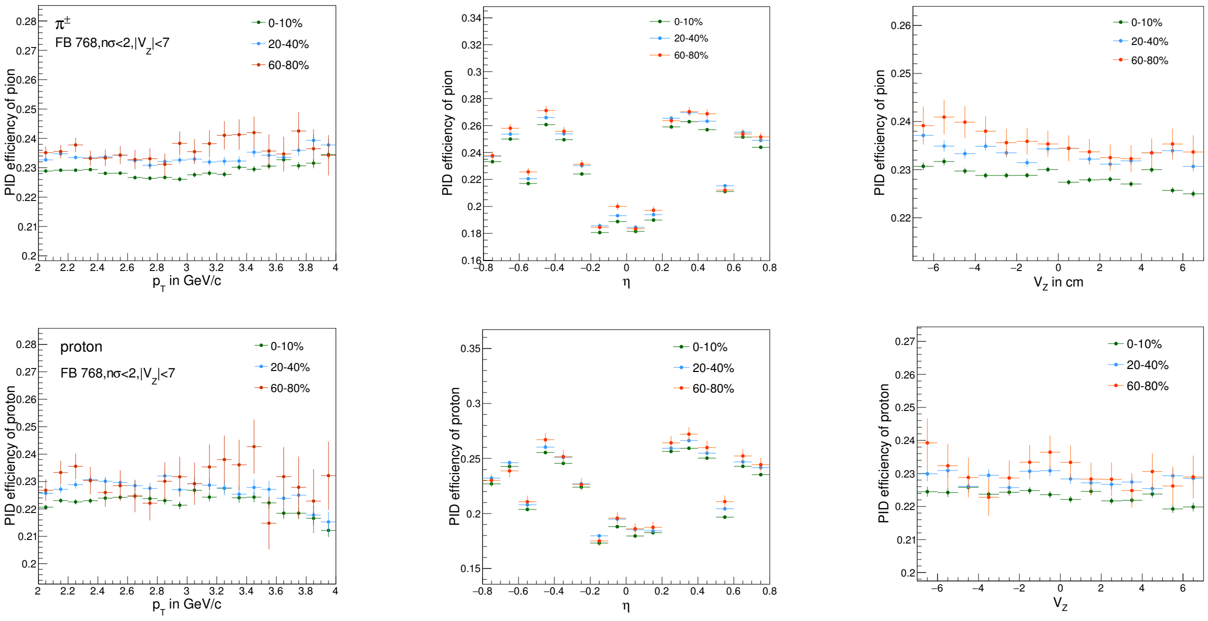

Figure 4.7: PID efficiency of pions and protons as a function of p_T, η, V_Z with default cuts

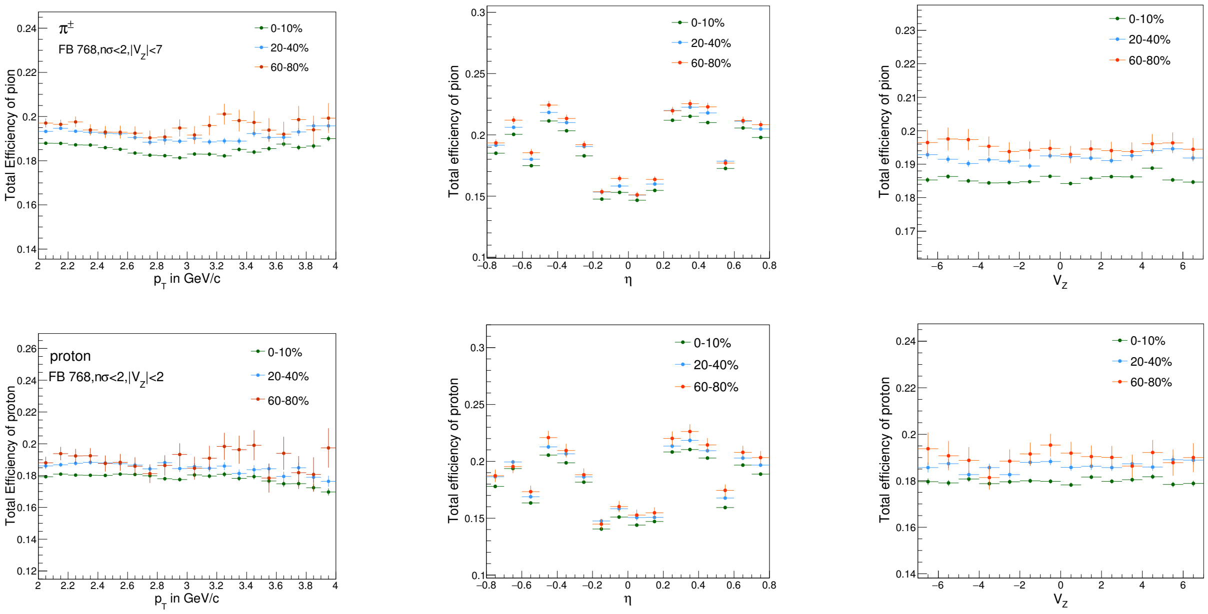

Figure 4.8: Total efficiency of pions and protons as a function of p_T, η, V_Z with default cuts

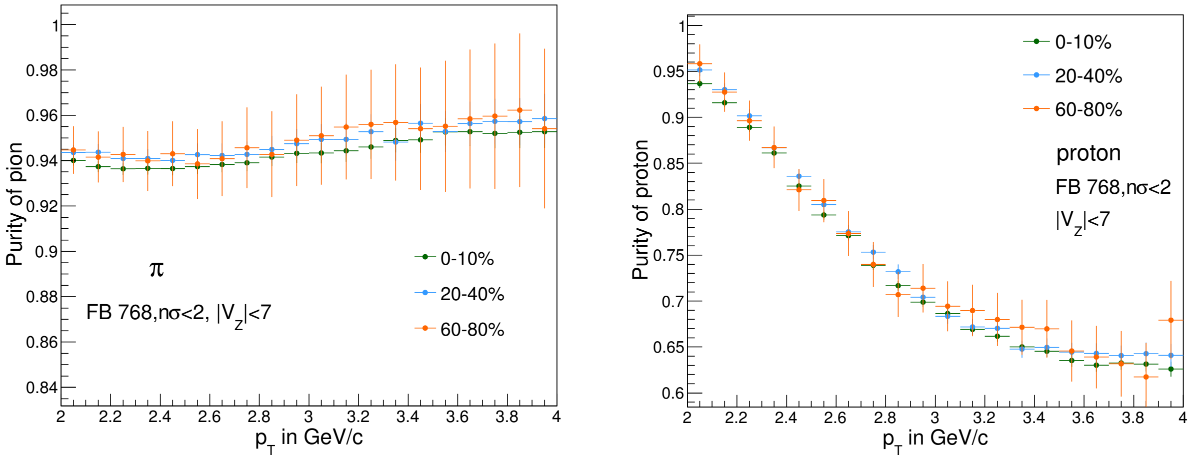

Figure 4.9: Purity of pions and protons as a function of p_T, η, V_Z with default cuts

$\epsilon_{\pi,p}$ are the corresponding factors for pions and protons, and ϵ_{PID} is the PID efficiency. Correcting the measured correlation with the final correction factor will give the true correlation function. Correction factors are shown in Fig 4.10. The correction factors are applied on the correlation function η, p_T, V_Z binwise. The correction factors are estimated in single particle level separately for triggers and associateds and applied in the correlation as the product of these two.

4.3 MC Closure test

To verify the reliability of the correction factors and its extraction procedure, a closure test is performed. The correlation functions from the reconstructed MC tracks have been weighted with the correction factors and compared with the correlation functions from the True MC particles without any detector effect. If the extracted correction factors and the correction procedure are proper, then the ratio of the corrected reco-level correlation function and truth level correlation function should give unity. The $\Delta\phi$ projection of the Truth and Reco (corrected) correlation function for 0-10% for pion and proton triggered correlation is shown in Fig. 4.11 and the ratio between truth and reco for pion and proton for all centralities are shown in Fig.4.12 and Fig.4.13

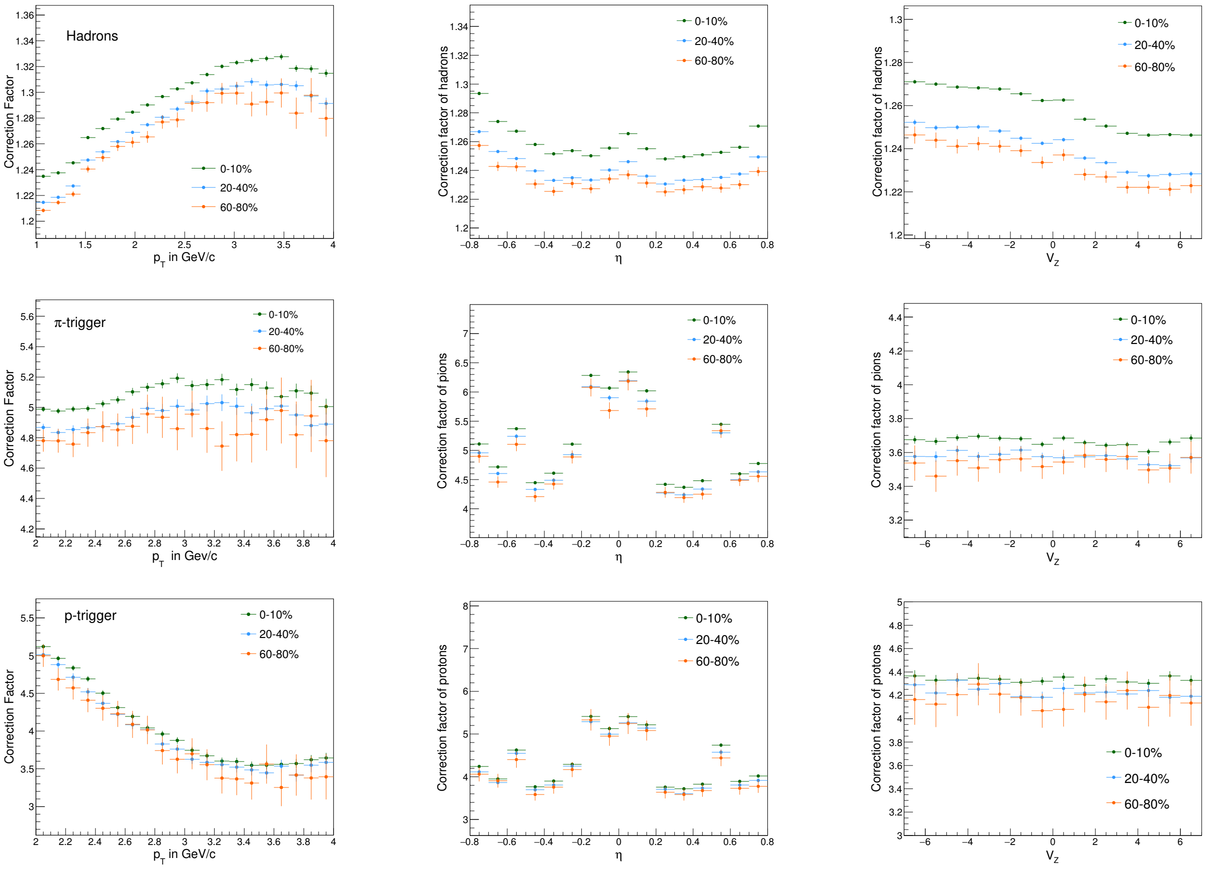

Figure 4.10: Correction factors for pions, hadrons and protons as a function of p_T, η, V_Z with default cuts

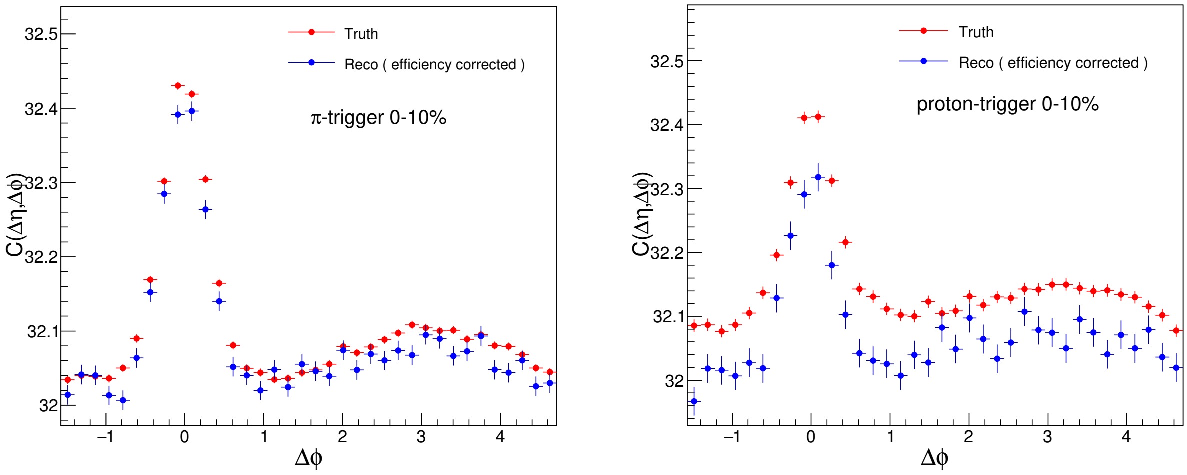

Figure 4.11: $\Delta\phi$ projection of Truth and Reco (Efficiency corrected) Pion & proton triggered correlation function for 0-10%

respectively. The figures show negligible deviation from unity, therefore validating the correction procedure.

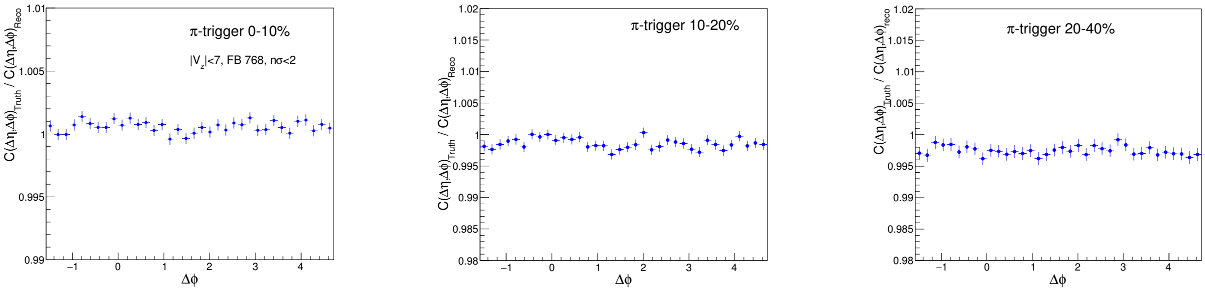

The near-side yields have been extracted from the MC-Truth and compared with the yields from efficiency corrected MC-Reco. Their ratios are shown in Fig.4.14 which further validates the reliability of the correction factors and the correction procedure.

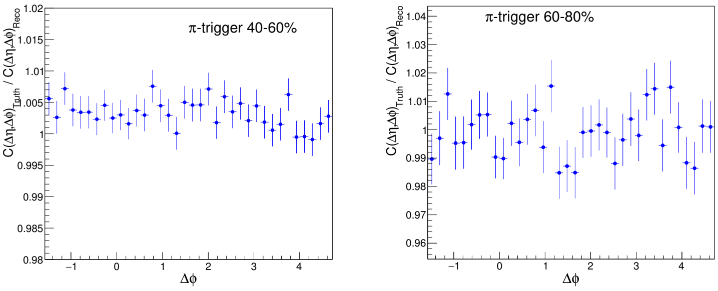

Figure 4.12: Ratio of reconstructed correlation function with all corrections applied to the true correaltion function at the MC level with pion triggers

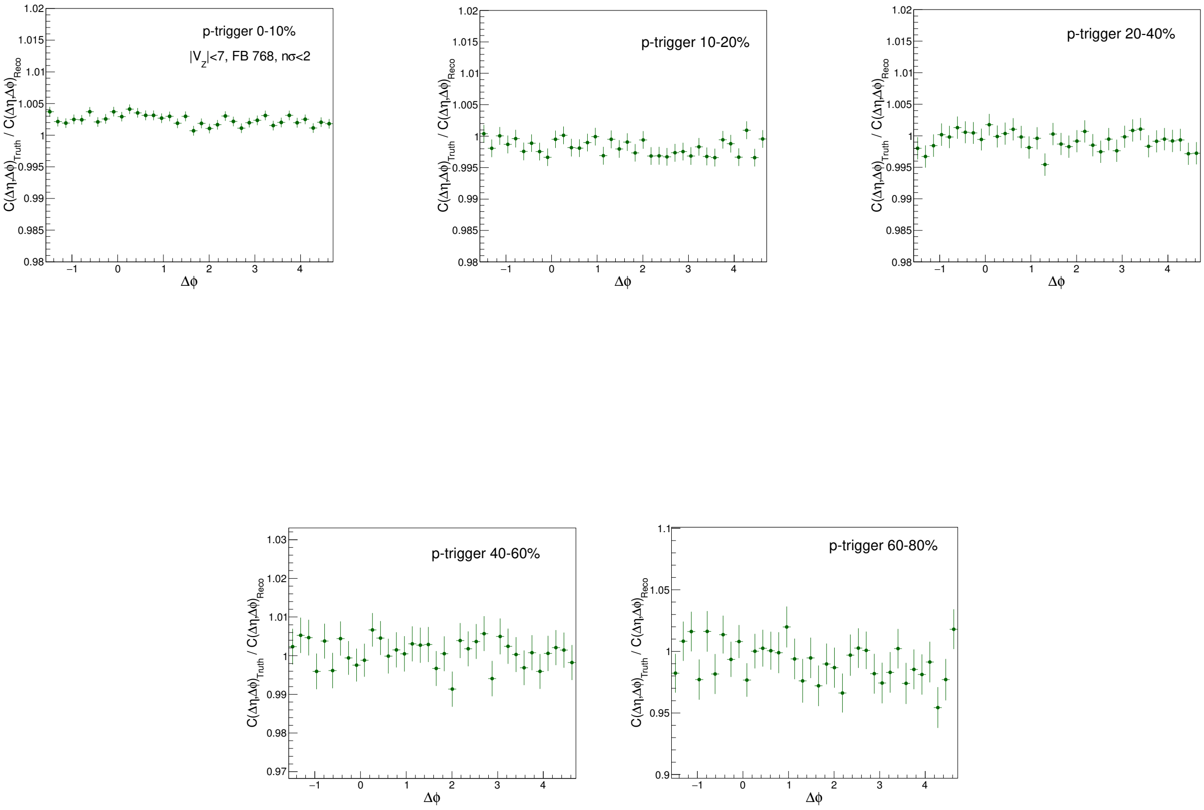

Figure 4.13: Ratio of reconstructed correlation function with all corrections applied to the true correaltion function at the MC level with proton triggers

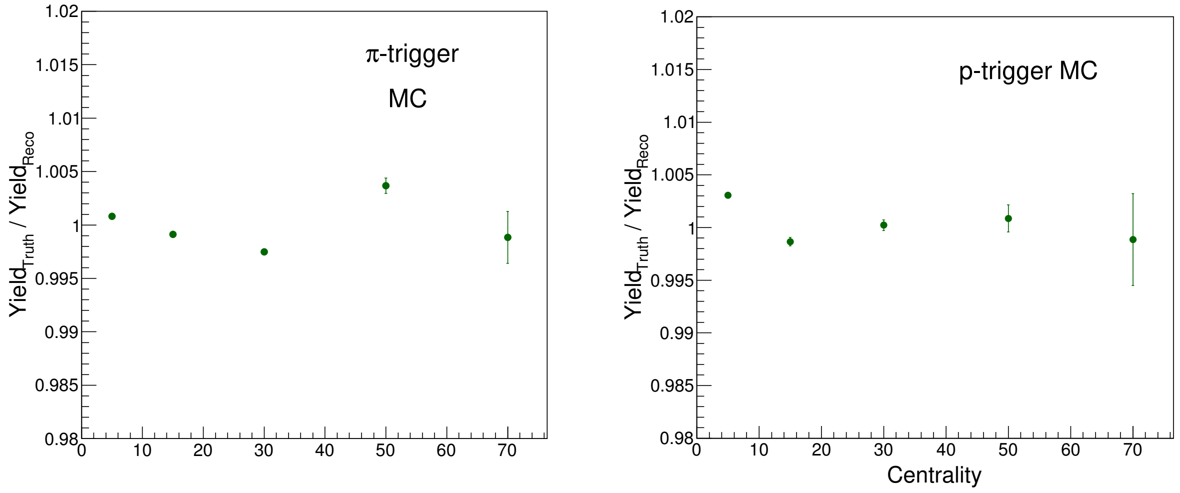

Figure 4.14: Ratio of the yields from the MC-Truth to the yields from efficiency corrected MC-Reco

4.4 Yield determination

The aim of this analysis is to measure the yield of the near side peak ($-\pi/2 < \Delta\phi < \pi/2$) as a function of centrality. To get the yield under the near side peak, the flow contributions need to be subtracted. The near side peak is located around $\Delta\eta, \Delta\phi \approx$0,0. The large $|\Delta\eta| > 1.2$ region represents the bulk/ridge region due to long range correlation. This region is subtracted from the peak ($|\Delta\eta| < 1.2$) to extract the jet-yield for each centrality, assuming the flow modulation contributions to be $|\Delta\eta|$ independent. Beside the collective flow contributions subtraction, this also removes the pedestal caused by the uncorrelated background. The correlation functions projected along $\Delta\phi$ for bulk and jet-peak region are shown in Figure 4.15.

ZYAM (Zero Yield At Minimum) bin counting method is used to calculate the near side yield ($-\pi/2 < \Delta\phi < \pi/2$). After subtracting the long range correlation from the short range one, the yield should be zero at minimum i.e. the baseline (away side) is expected to be at zero. But probably due to the mismatch between the actual detector efficiency and the exracted simulated detector efficiency, a small residual baseline is present. This is estimated by fitting the nearly flat away side region with a zero-degree polynomial. This non-zero fit value is then subtracted from every bin content to make the minimum at zero. The projection of the bulk subtracted correlation function before & after the baseline subtraction is shown in the Fig. 4.16 and Fig. 4.17. The final yield is the summation of all bin contents multiplied with the bin width from $\Delta\phi = -\pi/2$ to $\pi/2$. The yields as a function of centrality for pion and proton triggers and their ratios are shown in Fig.4.18.

Furthermore, the bulk subtracted 1-D $\Delta\phi$ projection is fitted with a Gaussian function to extract the yield by integrating the region between $-\pi/2 < \Delta\phi < \pi/2$. The fitted plots are shown in Fig.4.19. The difference between these two procedures will go into systematic error.

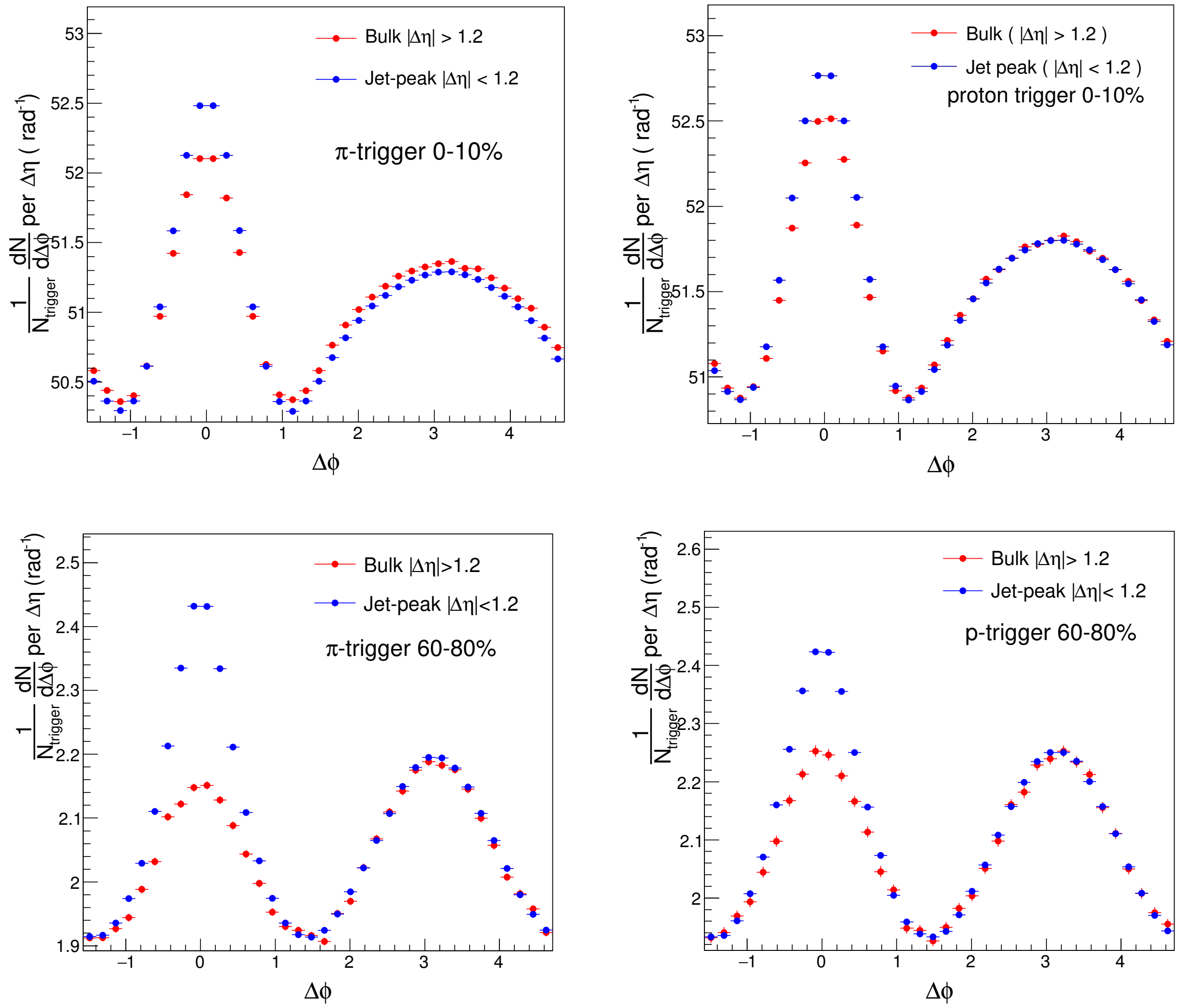

Figure 4.15: $\Delta\phi$ projection of Jet and Bulk region of pion and proton triggered correlation function for 0-10% centrality

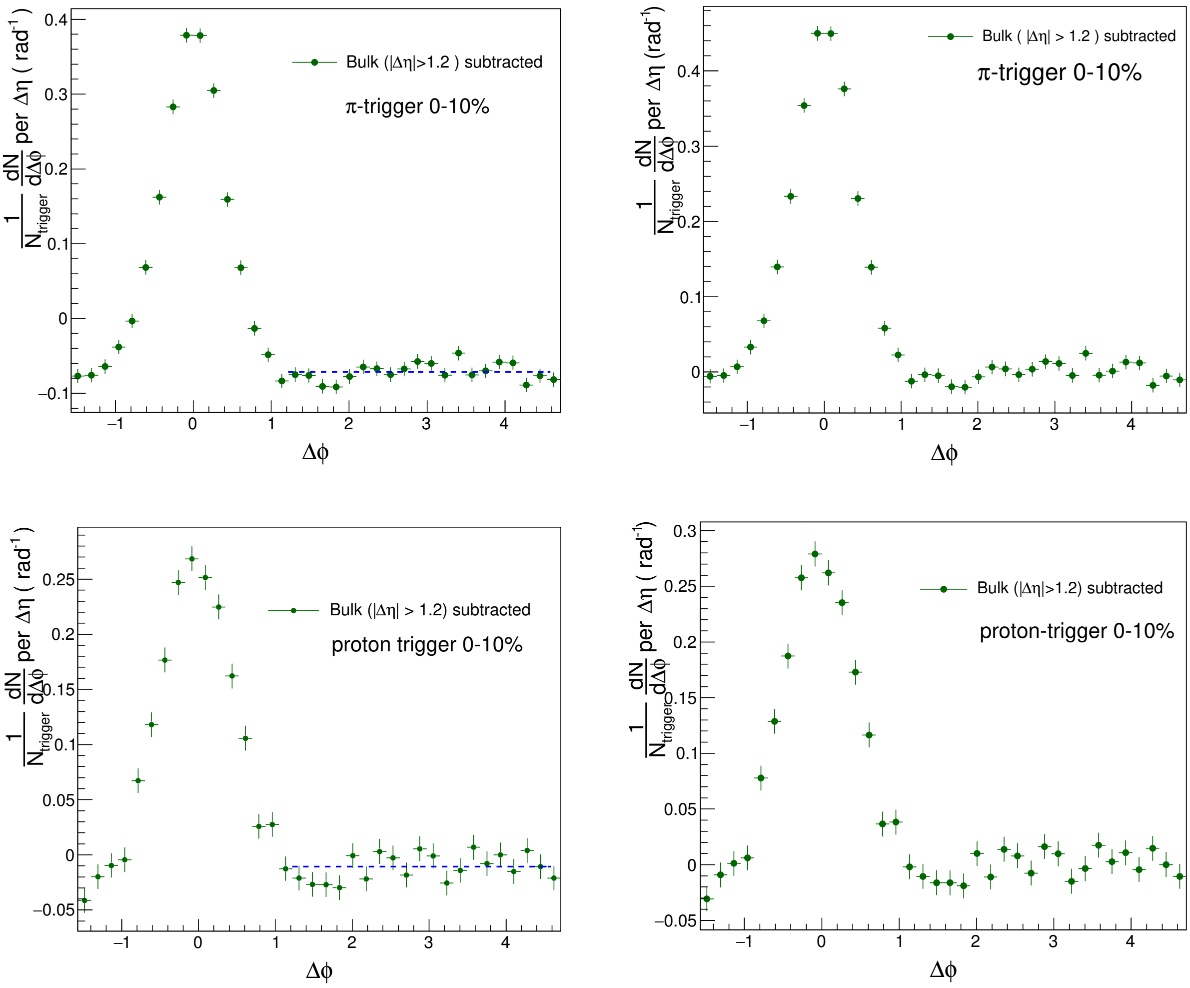

Figure 4.16: $\Delta\phi$ projection of Bulk subtracted jet region of pion and proton triggered correlation function for 0-10% centrality before (left panel) and after baseline subtraction (right panel)

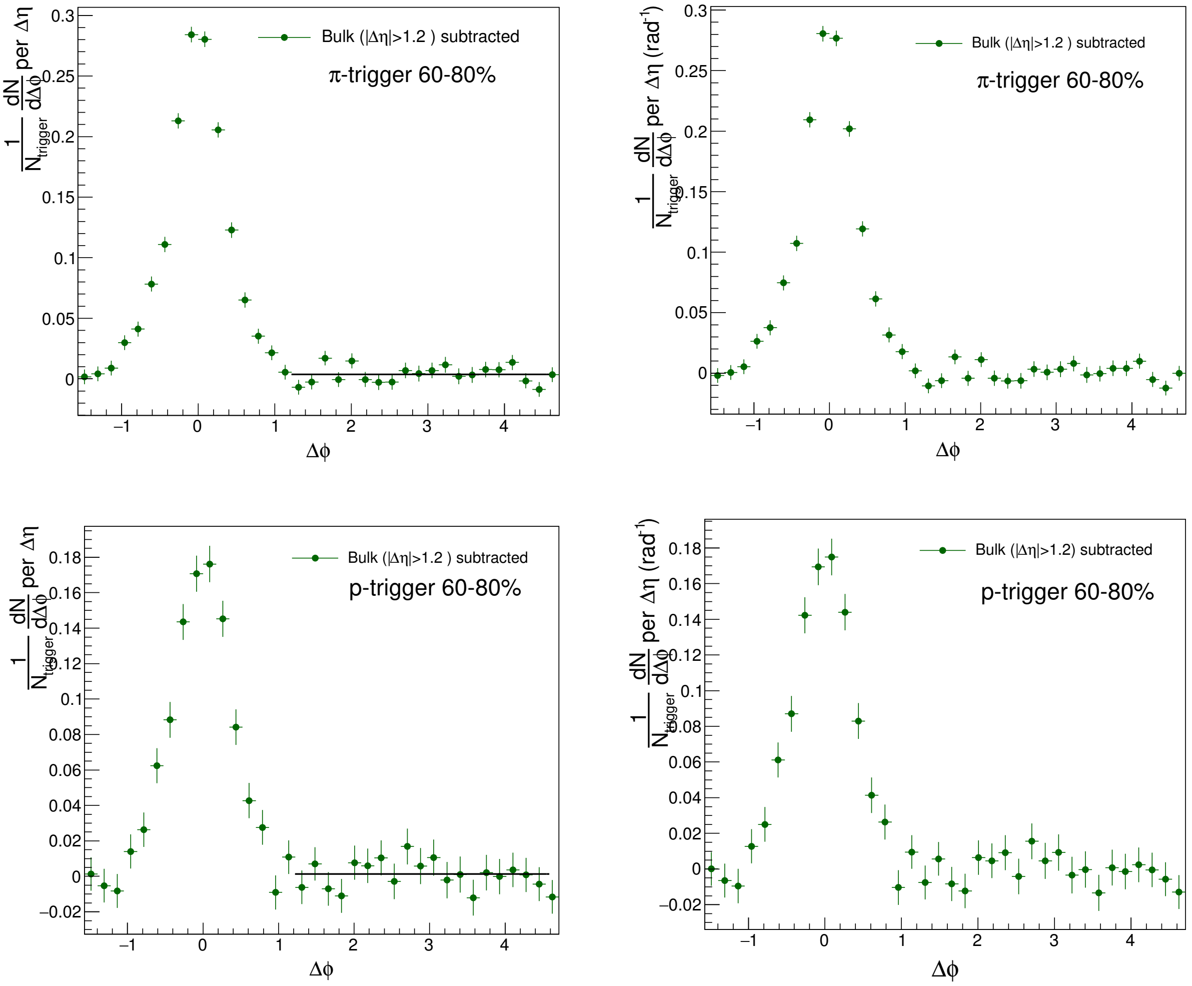

Figure 4.17: $\Delta\phi$ projection of Bulk subtracted jet region of pion and proton triggered correlation function for 60-80% centrality before (left panel) and after baseline subtraction (right panel)

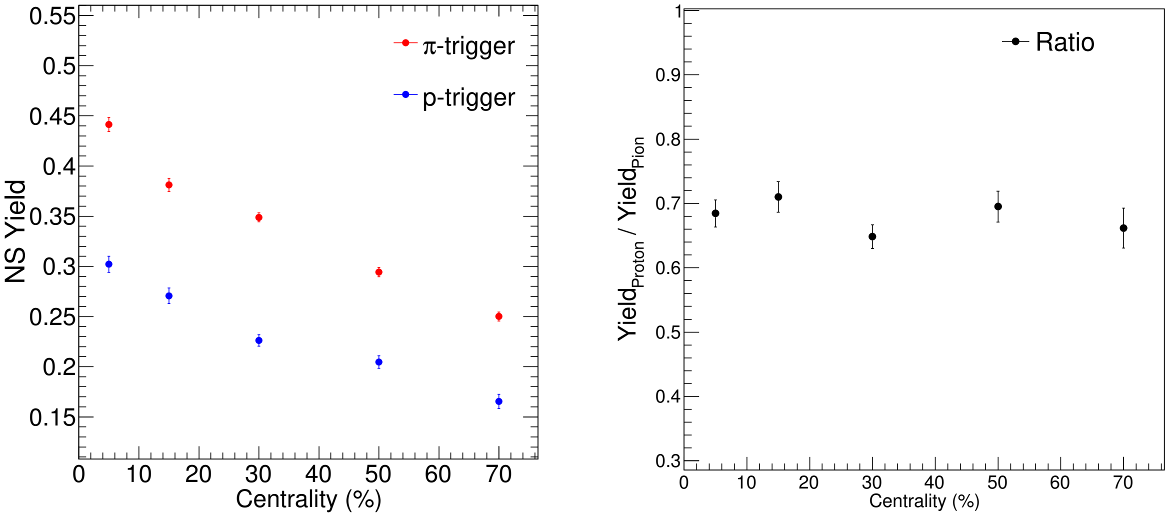

Figure 4.18: Near-side (NS) yield for pion and proton triggered correlation function and their ratio for Pb-Pb collision at $\sqrt{s_{NN}}$ =5.02 TeV with centrality (errors are statistical only)

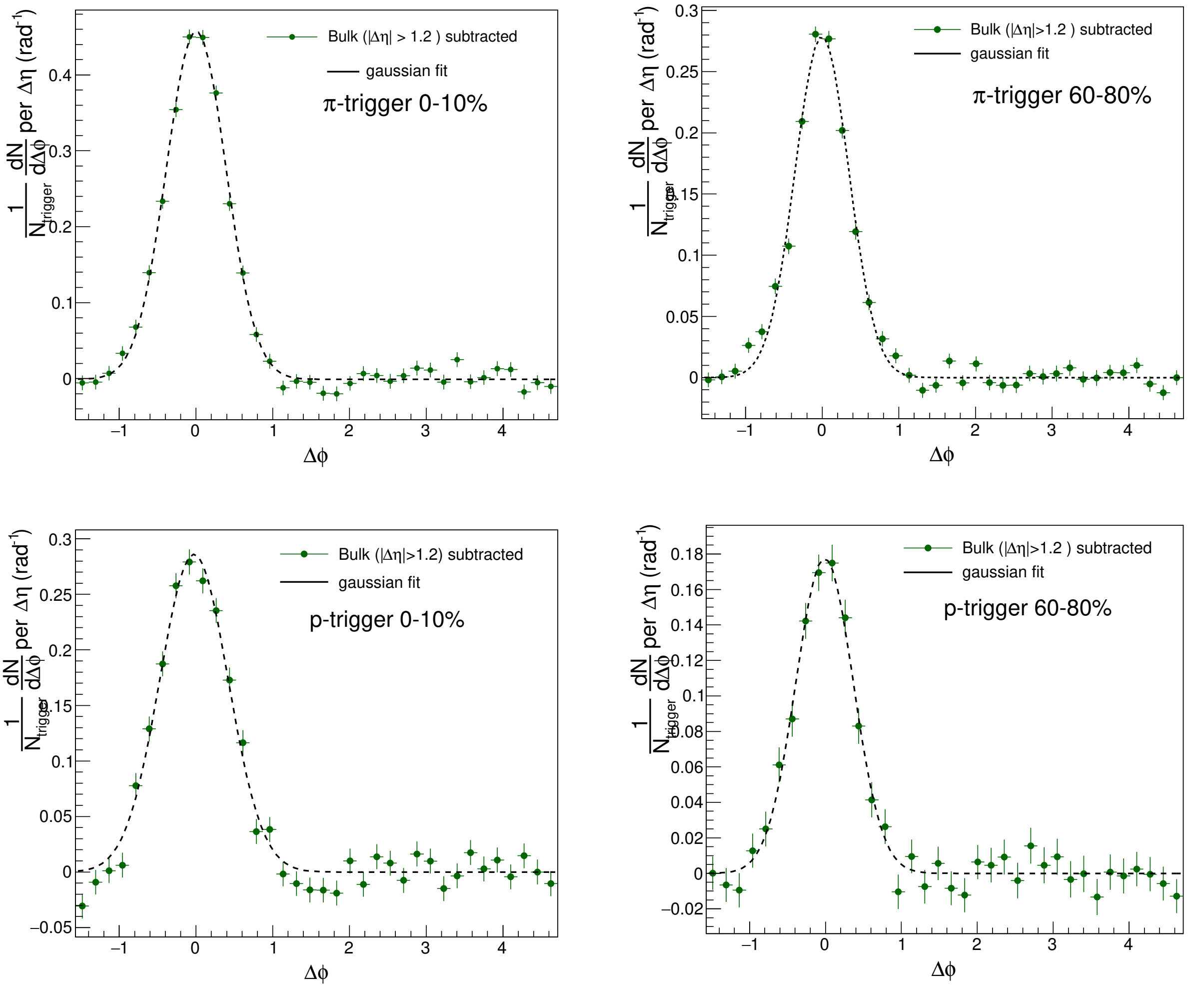

Figure 4.19: Pion and proton triggered correlation functions fitted with a Gaussian function

4.5 Systematic error estimation

The systematics study has been performed on the efficiency corrected correlation functions by varying different cuts and repeating the analysis. When a cut is varied to check the systematic variation, corresponding efficiency and correction factor have been extracted to estimate its systematic error.

4.5.1 Track cuts variation

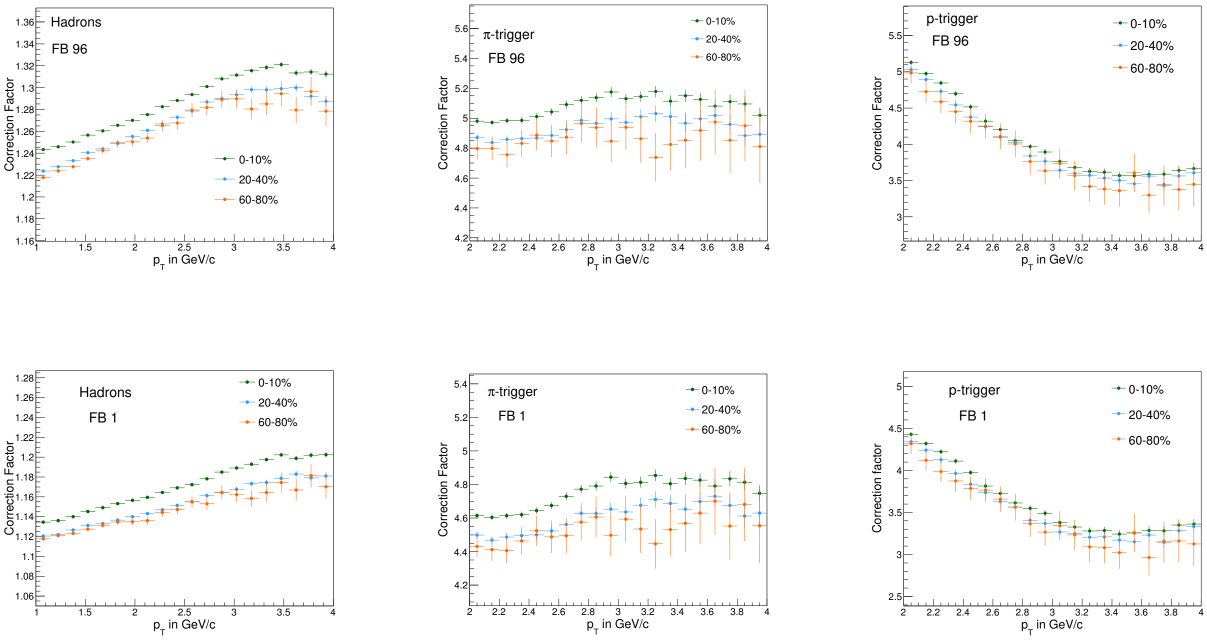

Figure 4.20: Correction Factors for Filter Bit 96 and 1 for hadrons , pions and protons

In this section, the systematic study of the yield for different track cuts are presented. Filter Bit 768 is the default filter bit.

1. Filter bit is set to 96 - global tracks with stricter DCA cut (32+64, additionally FB 32 requires hit on SPD and FB 64 requires SDD and no SPD hit).

2. Filter Bit is set to 1 - tracks reconstructed only by TPC with loose DCA.

The correction factors for FB 96 and FB 1 for hadrons, pions and protons are shown in Fig.4.20.

The corresponding relative variation in yield is shown in Fig.4.21. The variation in the yield is $<$ 2% for pion trigger and $<$ 5% for proton trigger.

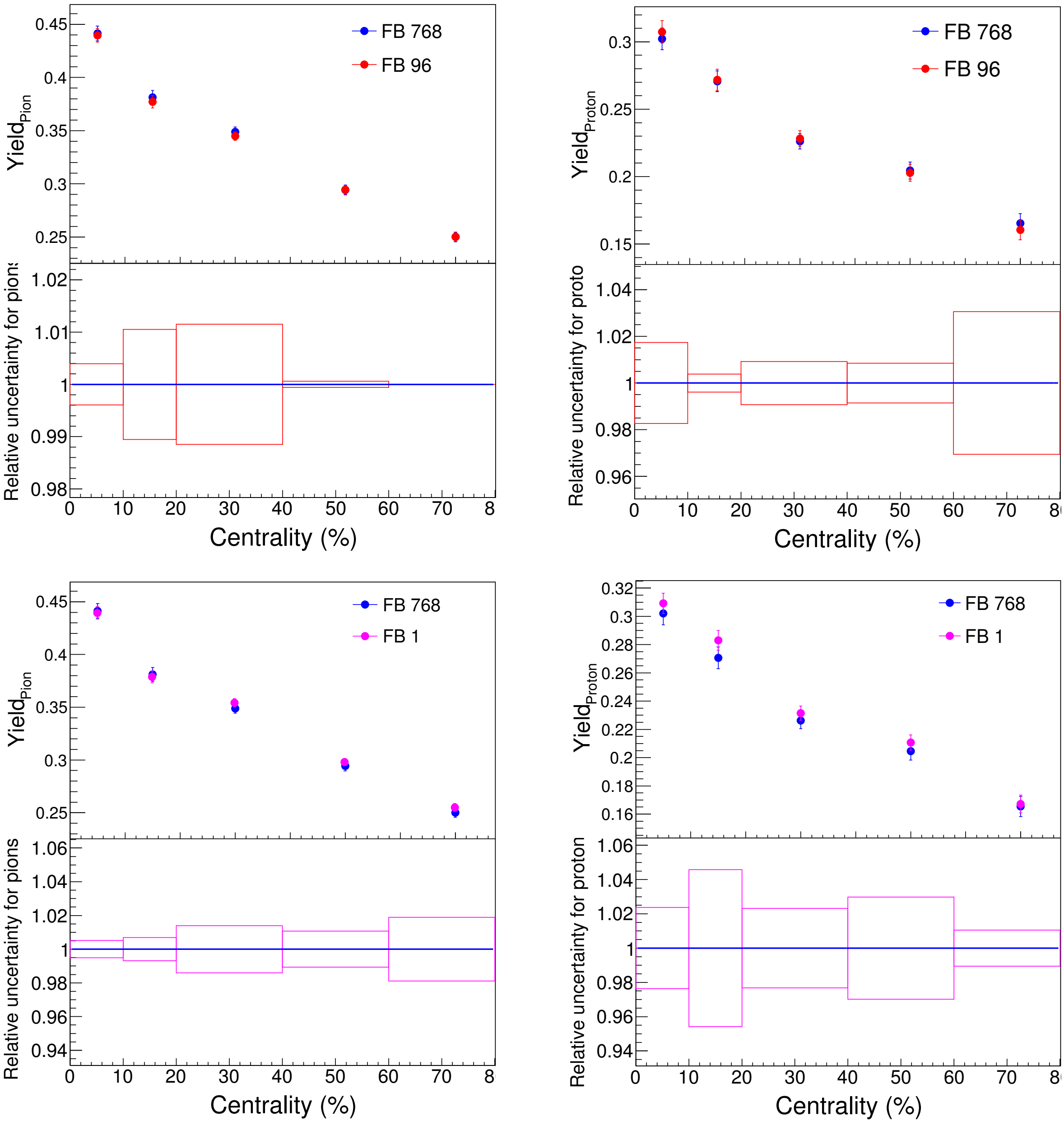

Figure 4.21: Systematic uncertainty for two Filter Bits for pion and proton triggered correlation

4.5.2 PID N_σ cuts variation

Here, results with different PID cuts have been reported. The default PID cut is $N_\sigma < 2$ (no double counting). The PID N_σ cut is then set to 3. The corresponding correction factors are shown in Fig. 4.22 and the corresponding change in yield is shown in Fig. 4.23. The variation in yield is <2 % for pions and <5% for protons.

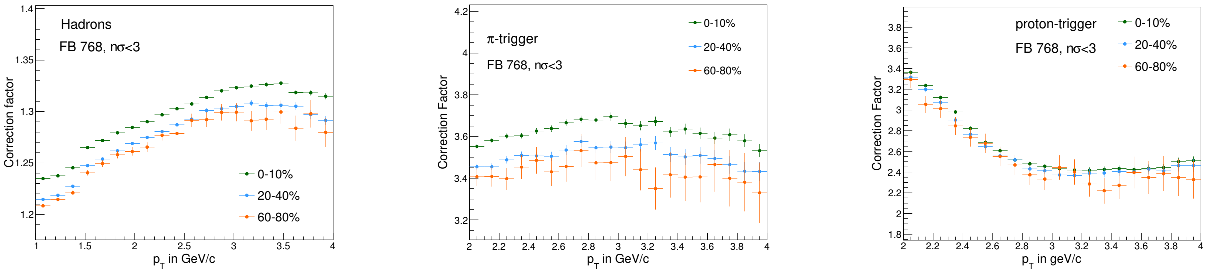

Figure 4.22: Correction factors for $N_\sigma < 3$ for hadrons,pions and protons

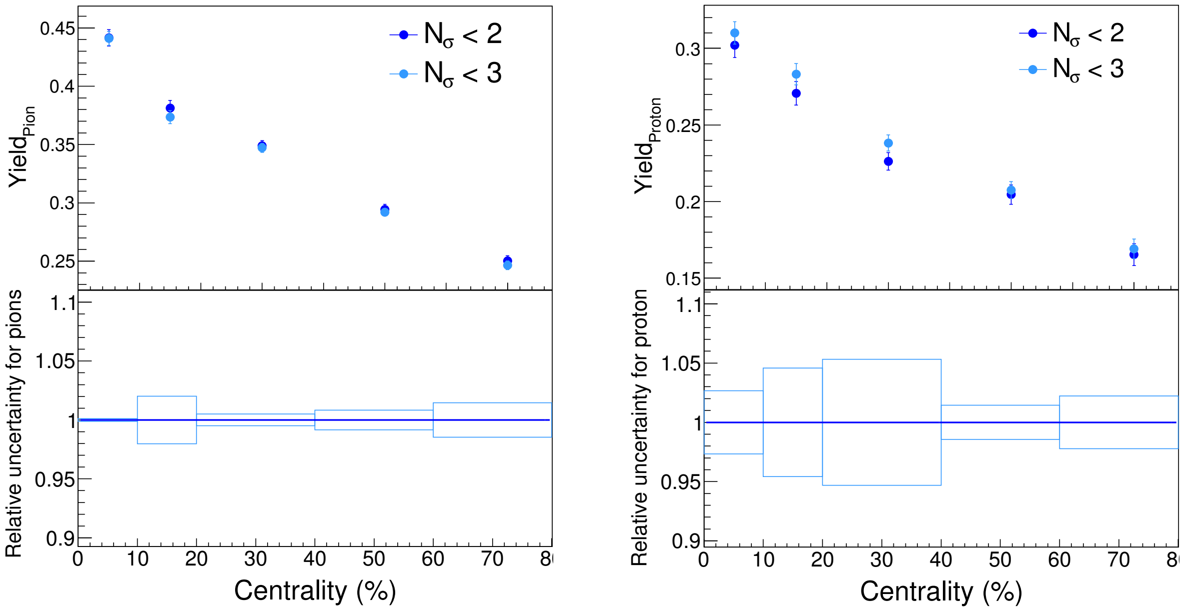

Figure 4.23: Systematic Uncertainty in the yield of the associated particles for $n\sigma < 3$ for pion and proton triggered correlation

4.5.3 Varying the electron rejection cut

As a systematic check, electron rejection cut is applied at the track level. The number of sigmas N_σ using TPC is calculated for every track from pion, proton, kaon and electron. A track is rejected if it falls within the electron band but is outside the region of pion, proton and kaon i.e. if $N_{\sigma,electron} < 2.0$ & $N_{\sigma,pion} > 2.0$ & $N_{\sigma,kaon} > 2.0$ & $N_{\sigma,proton} > 2.0$ then the track is rejected. The corresponding correction factors and the relative change in yield are shown in Fig.4.24 and fig.4.25. The variation in yield is <2% for both cases.

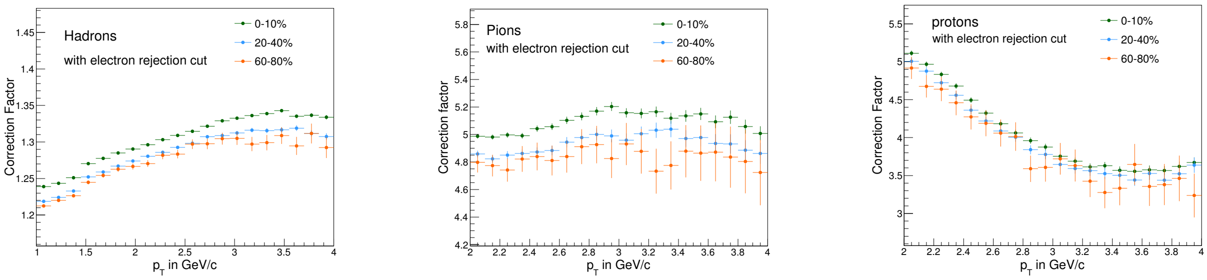

Figure 4.24: Correction factor with electron rejection cut implemented for hadrons,pion and proton

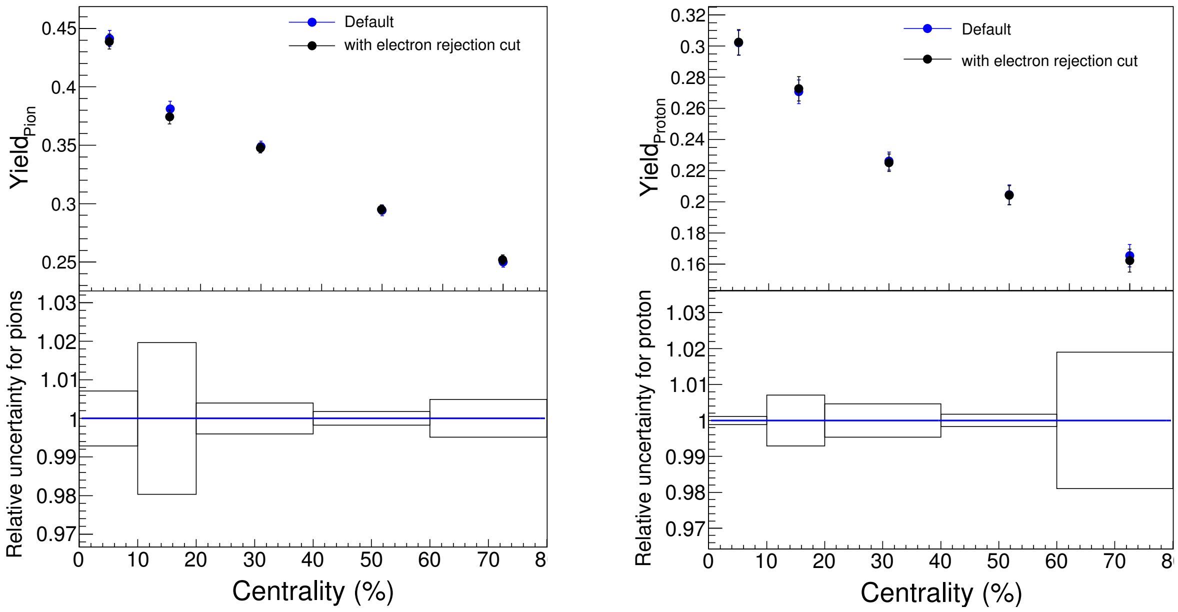

Figure 4.25: Systematic Uncertainty in yields of associated hadrons estimated by implementation of electron rejection cut for pion and proton triggered correlation

4.5.4 Varying the Z-vertex cut

The default vertex cut is $|V_Z| <7$ cm. For systematic study, the cut is changed to $|V_Z| <9$ cm and $|V_Z| <5$ cm. The correction factors for $|V_Z| <9$ and $|V_Z| <5$ for pion and proton are shown in Fig 4.26 and the corresponding yield variation is shown in Fig.4.27. The variation is <6% for pions and <5% for protons.

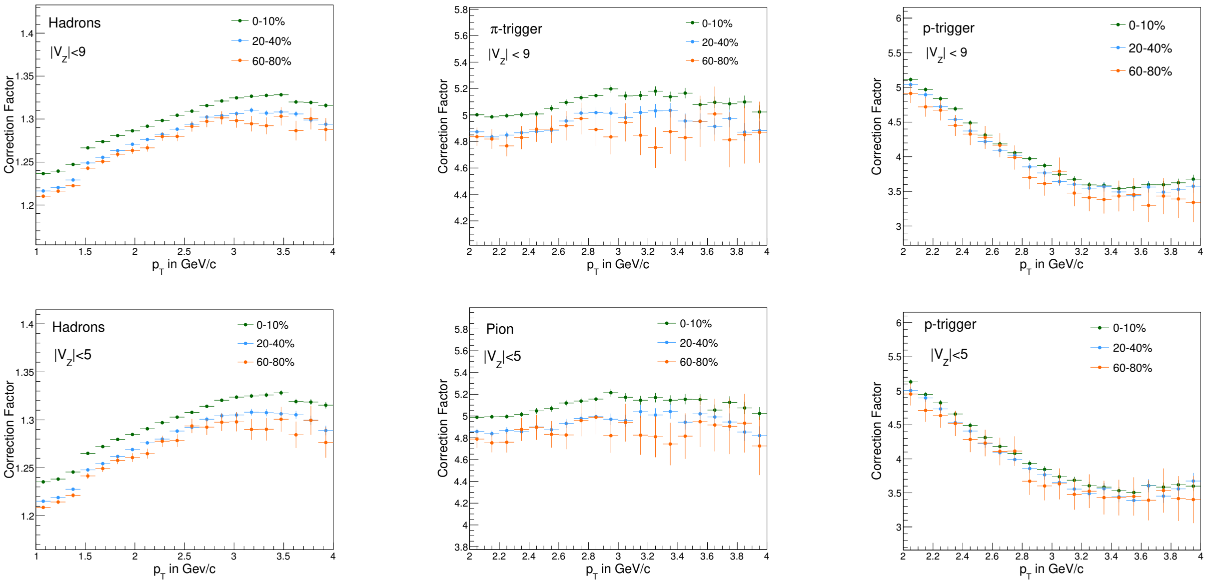

Figure 4.26: Correction Factors for $|V_Z| <9$ and $|V_Z| <5$ for hadrons as associateds and pion and proton as trigger particles.

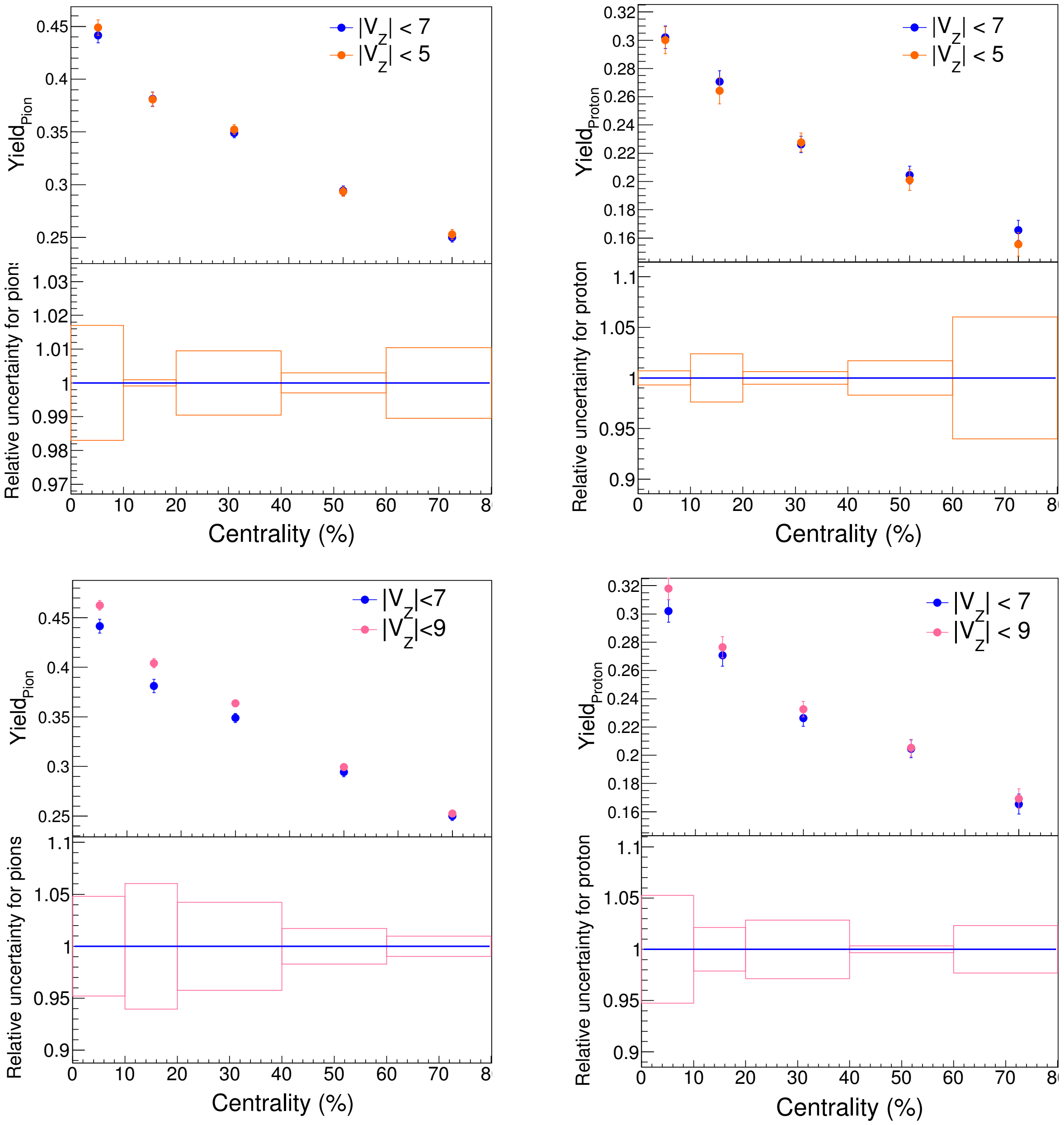

Figure 4.27: Systematic Uncertainty in yields of associated hadrons estimated by using two different vertex cuts for pion and proton triggered correlation functions.

4.5.5 Varying the mixed event binning

The default binning in the z-Vertex in the mixed event is 10 bins, 2 cm wide and for systematic study, it is changed to 20 bins, 1 cm wide. As this cut deals with the mixed event, the correction factors are same as default. The relative uncertainty is shown in Fig.4.28. The variation is found to be <3% for pions and <6% for protons.

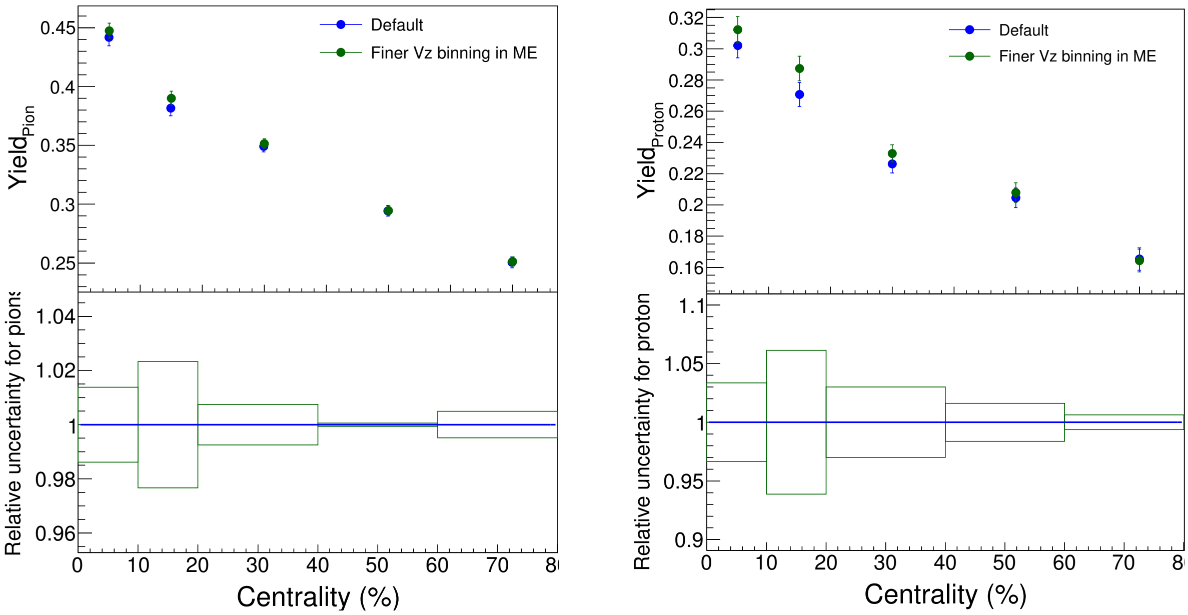

Figure 4.28: Systematic Uncertainty in yield of associated hadrons estimated by varying the Z-vertex binning in mixed event for pion and proton triggered correlation.

4.5.6 ZYAM bin counting vs Fit

The default yield extraction method is ZYAM bin counting. The yield has also been extracted by fitting with a Gaussian function. The difference between these two cases is shown in Fig 4.29. The variation is <2% for pions and <6% for protons.

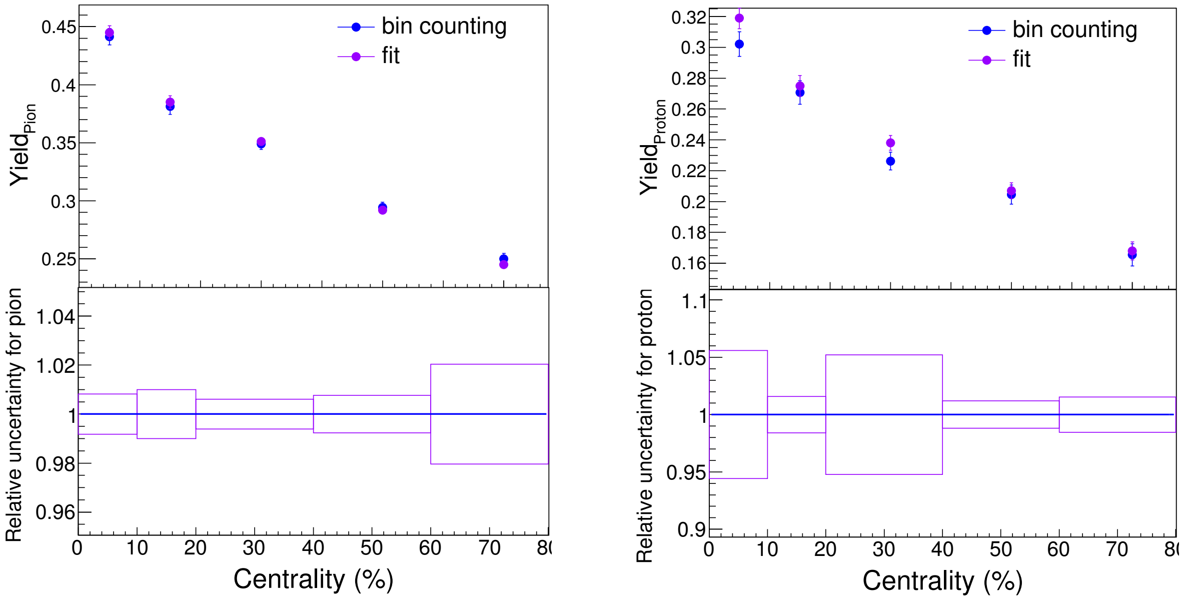

Figure 4.29: Comparison between the yields extracted using the bin counting method and the Gaussian fit method

4.5.7 Change in the bulk range

The bulk region range is changed to $|\Delta\eta| > 1.4$ from the default range $|\Delta\eta| > 1.2$ keeping the peak region same $|\Delta\eta| < 1.2$ to check the variation in the near side yield after subtracting the bulk region from peak. The plots are shown in Fig 4.30. The variation is <7% for both.

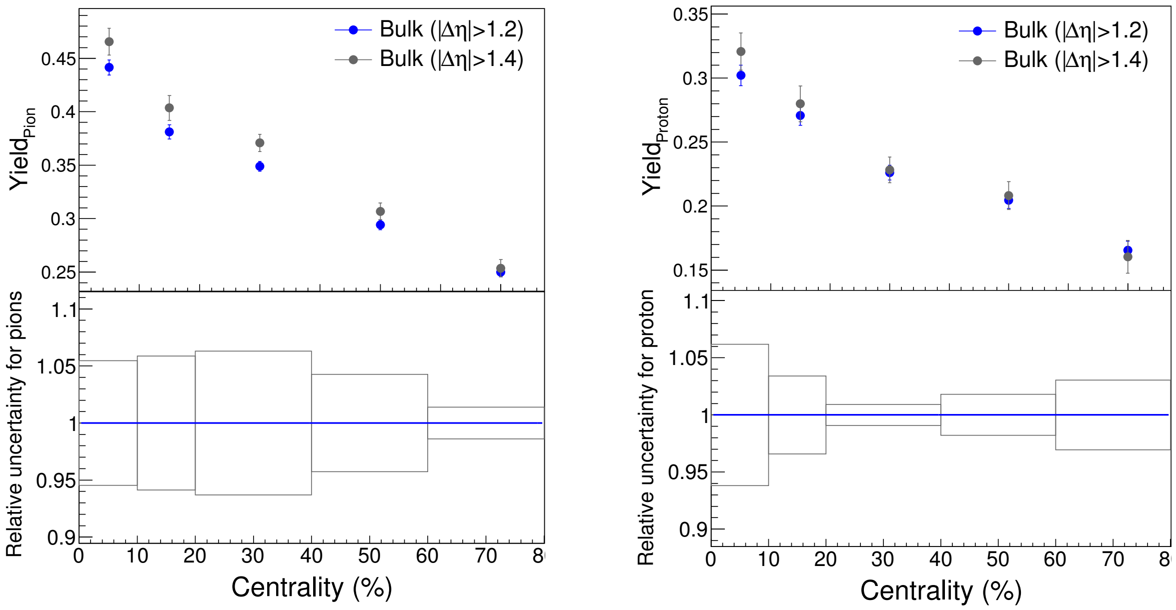

Figure 4.30: Systematic Uncertainty in yields of associated hadrons due to the change in bulk region

4.5.8 Change in the secondary contamination

The contaminations from the secondary pions and protons are calculated using MC (sec.2.2) on track by track basis. For the pion tracks, this extracted factor is increased by 5% and for the proton tracks, this is increased by 10% and are used in the correction factor. The variations in the yield are quoted as systematics in Fig.4.31. The variation is <1% for pions and <3% for protons.

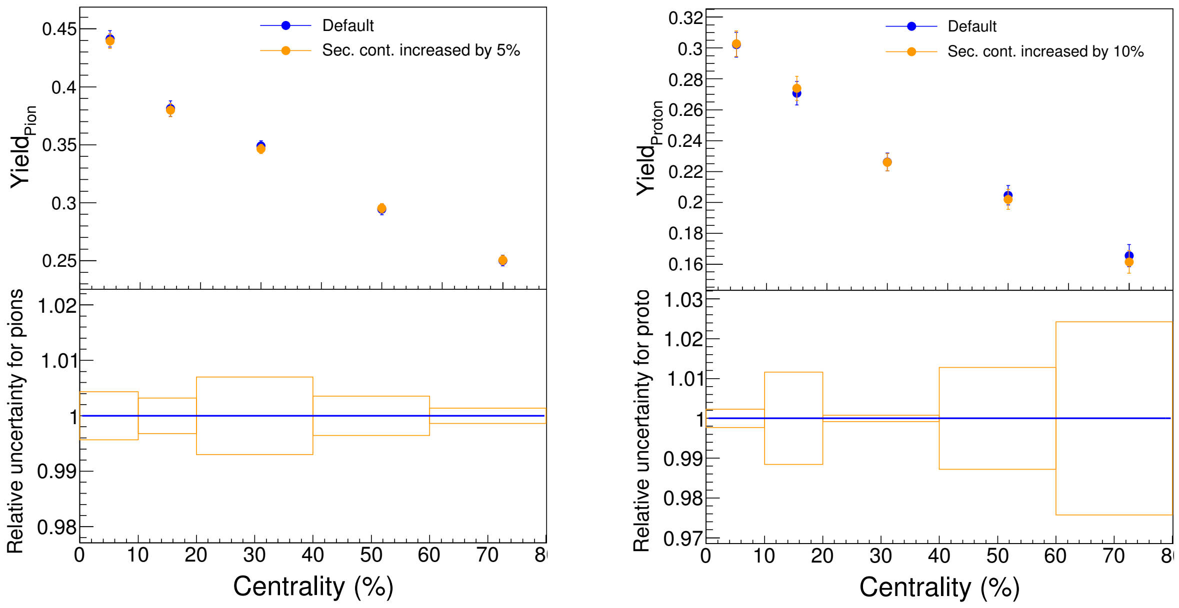

Figure 4.31: Systematic Uncertainty in yields of associated hadrons estimated by varying the secondary contamination percentage.

4.5.9 Different productions

The analysis has also been performed with the pass1 Low interaction rate (IR) ($2 < IR < 4$ kHz), Mid IR ($4 < IR < 5.5$ kHz) and High IR ($IR > 5.5$ kHz) separately. The variation relative to full dataset is shown in Fig.4.32. The maximum variation is almost 10% for pions and 16% for protons.

4.5.10 Summary of systematics

Fig.4.33 shows all the relative uceratinties studied so far for pion and proton triggered yields. To evaluate whether these systematics checks are statistically significant or not, Barlow check is performed. For each variation, the quantity D-D' & its error $\sqrt{(D_{err}^2 \pm D_{err}'^2)}$ are calculated, where D,D',D_{err},D'_{err} are the yield with default cut, yield with changed cut and their statistical errors respectively. The errors will be summed if the samples are uncorrelated, and the difference is for correlated samples. Then, the Barlow factor F is calculated as, F=$|\frac{D-D'}{\sqrt{(D_{err}^2 - D_{err}'^2)}}|$. If $F < 1$, this

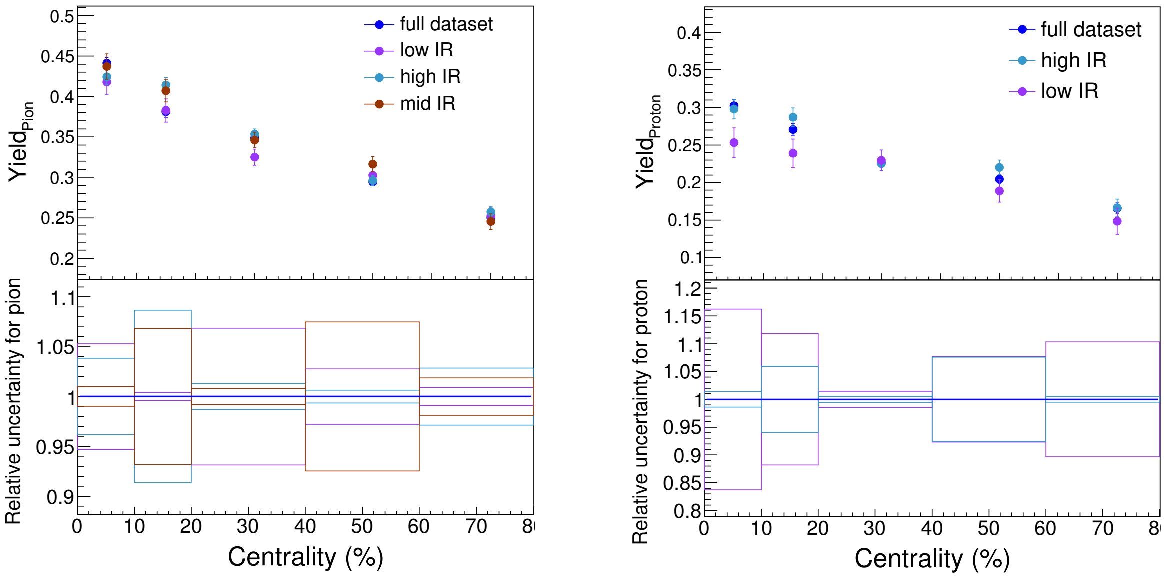

Figure 4.32: Systematic Uncertainty in yields of associated hadrons estimated by using different production passes.

is not considered as systematic uncertainty, as this can be due to statistical fluctuation. Only the errors with $F > 1$ are considered as systematic uncertainties. The table 4.1 and Table 4.2 present the barlow factors for all variations for all centralities.

The total systematic uncertainty is then obtained by adding all the significant systematic uncertainties satisfying the Barlow test in quadrature and taking the square root value. The final corrected plots with statistical error (shown in bar) and total systematic error (shown in box) are shown in Fig.4.34.

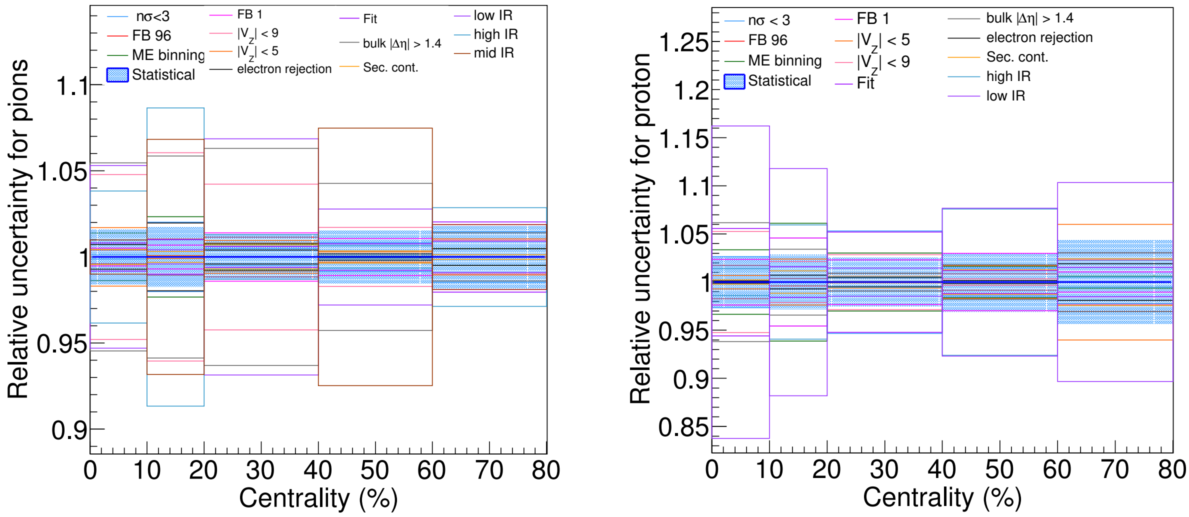

Figure 4.33: Relative Uncertainties (statistical and systematics)

Barlow check for Pions										
Centrality	0-10%		10-20%		20-40%		40-60%		60-80%	
D-D’	D'_{err}	F	D'_{err}	F	D'_{err}	F	D'_{err}	F	D'_{err}	F
$n\sigma < 2$-$n\sigma < 3$	0.0059	0.142	0.0055	2.146	0.0038	0.721	0.0036	0.913	0.0038	1.515
FB768-FB96	0.0062	0.573	0.0057	1.220	0.0040	1.897	0.0040	0.082	0.0040	0.016
FB 768 - FB 1	0.0059	0.616	0.0055	0.731	0.0038	2.020	0.0036	1.174	0.0038	1.948
ME10-ME20	0.0064	2.302	0.0059	3.005	0.0040	1.237	0.0040	0.082	0.0040	0.577
$V_Z 7 - v_Z 9$	0.0048	4.239	0.0045	4.763	0.0031	4.504	0.0031	1.540	0.0032	0.766
$V_Z 7 - v_Z 5$	0.0073	3.357	0.0068	0.227	0.0047	2.609	0.0046	1.158	0.0047	2.060
$bulk_{>1.2} - bulk_{>1.4}$	0.012	2.305	0.011	2.319	0.008	3.320	0.0078	1.960	0.008	0.527
electron rej.	0.0064	1.184	0.0059	2.533	0.0042	0.8	0.0040	0.247	0.0042	0.7
sec. cont.	0.0062	0.630	0.0057	0.371	0.0040	1.154	0.0040	0.494	0.0040	0.164
Low IR	0.0153	1.709	0.0143	0.123	0.0099	2.70	0.0095	0.969	0.0099	0.256
Mid IR	0.0157	0.310	0.0139	2.116	0.0095	0.330	0.0094	2.662	0.0095	0.557
High IR	0.0099	2.388	0.0092	5.115	0.0064	0.987	0.0062	0.441	0.0064	1.557
ZYAM vs fit	0.0058	0.928	0.0054	0.992	0.0037	0.802	0.0036	0.819	0.0037	1.943

Table 4.1: Barlow check for systematic uncertainty for Pions

Barlow check for Protons										
Centrality	0-10%		10-20%		20-40%		40-60%		60-80%	
D-D'	D'_{err}	F	D'_{err}	F	D'_{err}	F	D'_{err}	F	D'_{err}	F
$n\sigma < 2$-$n\sigma < 3$	0.0073	2.180	0.0069	3.444	0.0052	5.019	0.0055	1.030	0.0064	1.188
FB768-FB96	0.0083	2.566	0.0079	0.486	0.005	2.36	0.0063	3.196	0.0073	3.819
FB 768 - FB 1	0.0071	1.965	0.0069	3.873	0.0050	1.905	0.0054	1.912	0.0063	0.509
ME10-ME20	0.0084	4.028	0.0078	9.182	0.0055	4.837	0.0063	5	0.0073	0.658
$V_Z7 - v_Z9$	0.0078	9.539	0.0075	3.537	0.0055	4.589	0.0059	0.338	0.0069	2.444
$V_Z7 - v_Z5$	0.0095	0.398	0.0092	1.252	0.0066	0.424	0.0073	0.924	0.008	2.283
$bulk_{>1.2} - bulk_{>1.4}$	0.0144	1.548	0.0139	0.793	0.0101	0.251	0.0109	0.406	0.0127	0.480
electron rej.	0.0082	0.207	0.0078	1.166	0.0055	0.744	0.0061	0.237	0.0073	1.975
sec. cont.	0.0082	0.414	0.0078	1.908	0.0056	0.124	0.0064	1.755	0.0073	2.524
Low IR	0.0197	2.722	0.0190	1.835	0.0137	0.264	0.0150	1.152	0.0174	1.074
High IR	0.0130	0.405	0.0125	1.614	0.0090	0.174	0.009	2.074	0.0113	0.099
ZYAM vs fit	0.0070	4.294	0.0067	1.145	0.0048	3.708	0.0052	0.693	0.0059	0.627

Table 4.2: Barlow check for systematic uncertainty for Protons

From the Barlow test results, smoothing is done on the systematics. If there is a systematic trend for a particular trial and the barlow factor F $>$ 1 for at least two or three bins out of five centrality classes, then that trial is considered to be systematic and an average value of relative uncertainty of the five bins is assigned to all centrality classes. If F>1 for one bin only, then that is likely to be a statistical fluctuation, so that trial can be ignored. This is smoothing. The relative uncertainties after smoothing are shown in Fig.4.34

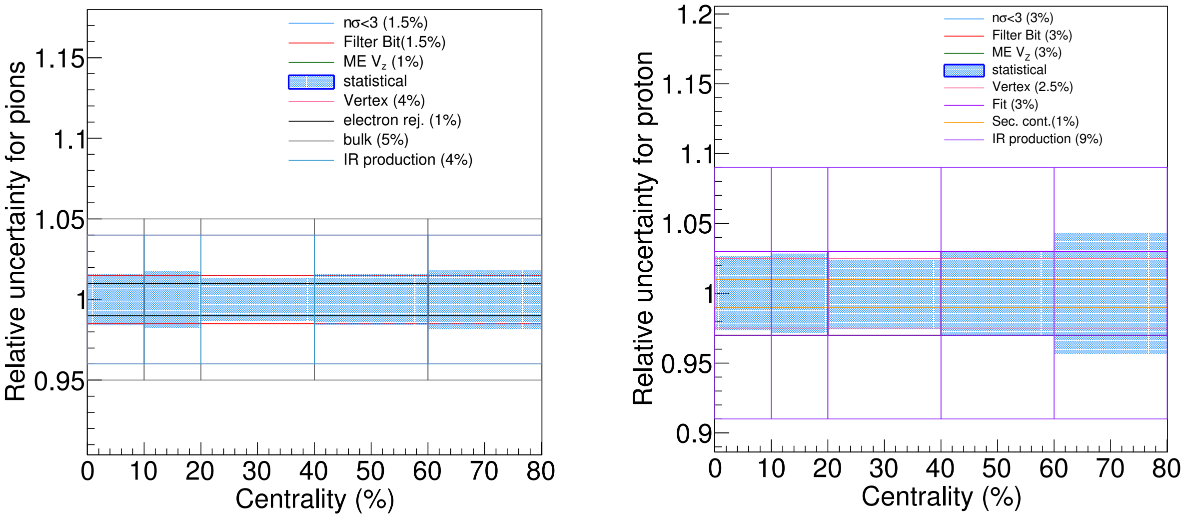

Figure 4.34: Relative Uncertainties after smoothing (statistical and systematics)

4.6 Estimation of systematics on the $\Delta\phi$-projection plot

The systematic uncertainties on the $\Delta\phi$ projection of the bulk subtracted correlation function have been estimated by varying different cuts. For every varied cut, corresponding $\Delta\phi$ projection of the correlation function has been plotted with the default one (Fig 4.35 left panel). Then, the difference between these two (Fig 4.35 right panel) and the corresponding relative uncertainties (Fig 4.36) are plotted. The fit value obtained by fitting the flat region around $\Delta\phi$ gives the systematic uncertainty corresponding to that cut for all $\Delta\phi$ bins. Likewise, the systematic uncertainties for all the varied cuts are obtained and added in quadrature to get the total systematic uncertainty in every $\Delta\phi$ bin which has been used in Fig 4.46.

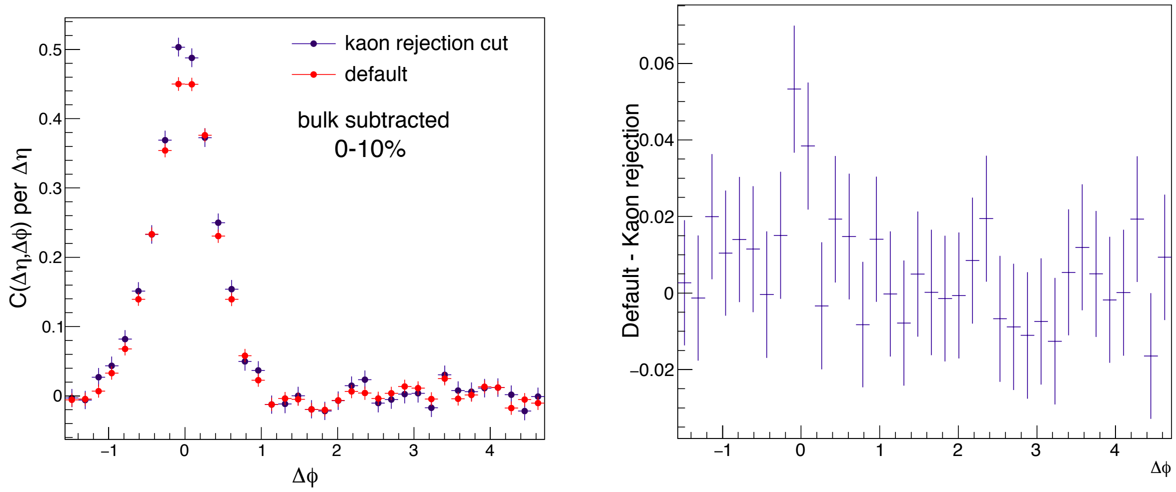

Figure 4.35: Left panel:Bulk subtracted correlation function projection on $\Delta\phi$ with default cut and with kaon rekection cut. Right panel: The difference between the two with $\Delta\phi$

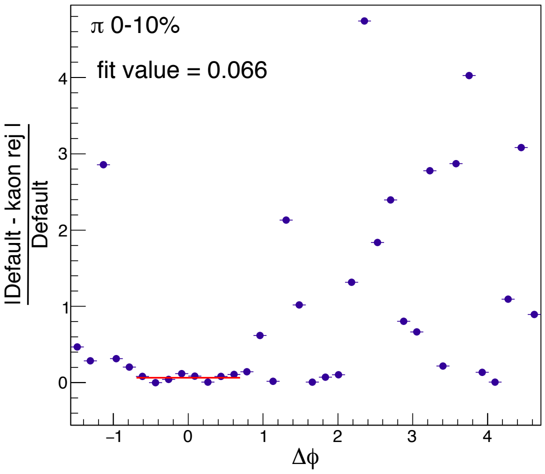

Figure 4.36: The corresponding relative uncertainty

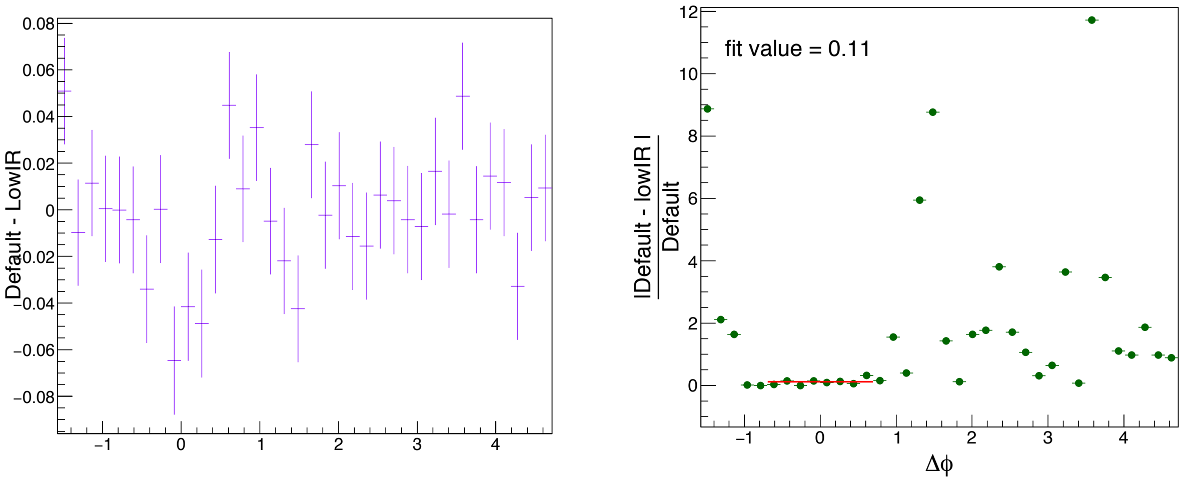

Figure 4.37: Left panel:Difference between bulk subtracted correlation function projection with full statistics and with low IR. Right panel: The corresponding relative uncertainty.

4.7 Model comparison

Results from the ALICE data have been compared with that from the model Heavy Ion Jet INteractionGenerator (HIJING) and A multi-phase transport (AMPT) . HIJING is a Monte-Carlo model to study the jets and particle production in high energy nuclear collisions [1]. Various physics processes involved in HIJING are multiple minijets production, multiple scattering in nuclear collisions, nuclear shadowing, final state interaction (jet quenching), jet fragmentation or hadronization. PYTHIA is used to generate kinetic variables of scattered partons for each hard or semihard interaction. The AMPT model has the initial conditions, partonic interactions, partonic to the hadronic matter conversion and hadronic interactions as its components [2]. AMPT generates the initial conditions using HIJING and models partonic interactions using Zhang's Parton Cascade (ZPC). In the default version, partons are combined to hadrons using the Lund string fragmentation model and in the string melting version, a quark coalescence model is used instead for partons to hadrons conversion. The subsequent hadronic interaction is described by a hadronic cascade, which is based onthe ART model.

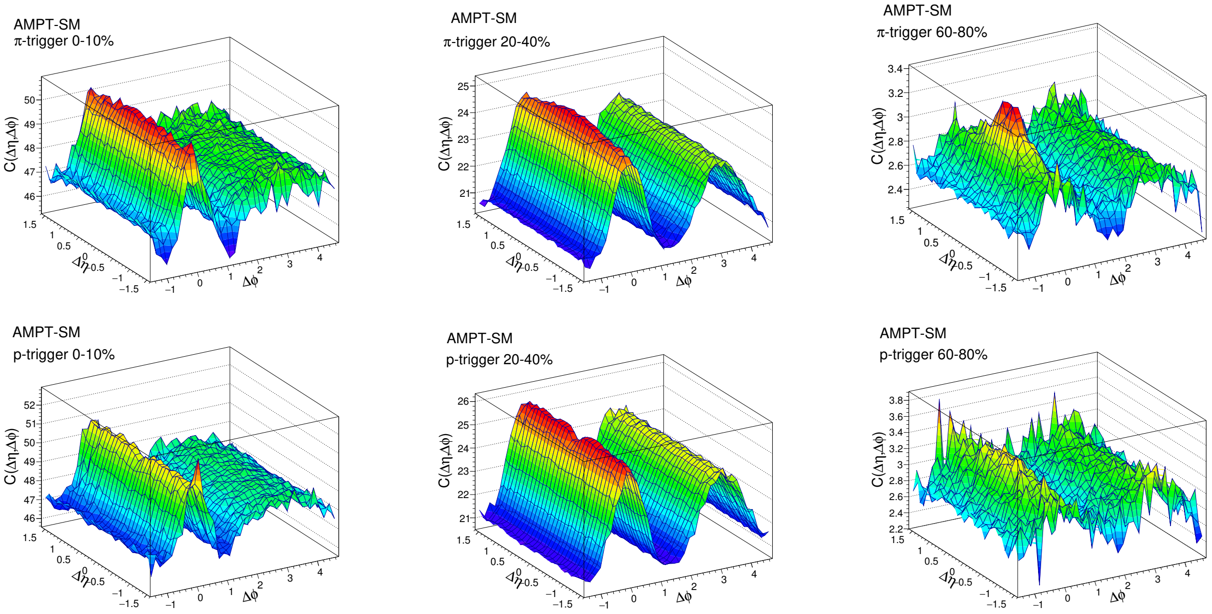

AMPT-SM
π-trigger 0-10%

AMPT-SM
π-trigger 20-40%

AMPT-SM
π-trigger 60-80%

AMPT-SM
p-trigger 0-10%

AMPT-SM
p-trigger 20-40%

AMPT-SM
p-trigger 60-80%

Figure 4.38: pion and proton triggered correlation from the AMPT-SM version.

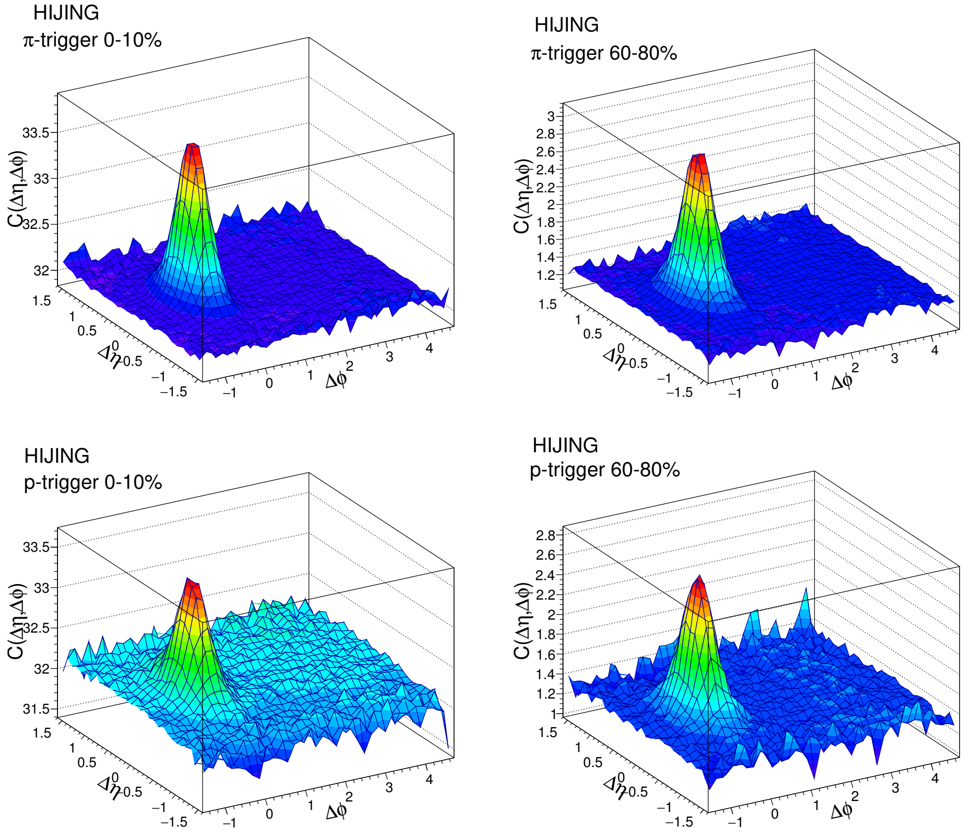

HIJING
π-trigger 0-10%

HIJING
π-trigger 60-80%

HIJING
p-trigger 0-10%

HIJING
p-trigger 60-80%

Figure 4.39: pion and proton triggered correlation from the HIJING model.

4.8 Wing Correction

The mixed event corrected correlation function shows an increase or decrease at large $|\Delta\eta|$ shown in Fig. 4.40. This is known as the "Wing effect". As per the previous studies, this effect might be due to finite bin width in event mixing. Fig. 4.40 (left panel) shows the $\Delta\eta$ projection of the 2D correlation function for $2 < \Delta\phi < 4$ (away-side) and $-\pi/2 < \Delta\phi < \pi/2$. Assuming no physics reason responsible for the wings, the structure should be flat at the away-side region. By, fitting this away-side region with a constant, the whole correlation structure is weighted by the data to fit ratio to flatten the structure forcefully. The same correlation function shown in Fig. 4.40 (right panel) is almost flat over the full $\Delta\eta$ in away-side region and over $\Delta\eta$ on both sides of the peak after the wing correction. Yield variation due to wing correction is $< 0.2\%$

4.8.1 Study of dip in the correlation function

A dip is developed in the correlation function with centrality around $\Delta\eta, \Delta\phi \approx 0, 0$. This dip is prominent in the correlation function for central collisions and for protons as trigger at low to intermediate p_T . The dip vanishes in peripheral collision as well as for pions. Also, the dip vanishes when the correlation function is constructed with high p_T trigger. To investigate whether it is a physics effect or detector effect, the dip as a function of $\eta - \phi$ distance between two tracks has been studied. But no difference between the dip structures for $|\Delta\eta$ & $\Delta\phi$ >0.02 and $|\Delta\eta$ & $\Delta\phi$ >0.04 is observed (Fig. 4.43 and Fig. 4.44) which suggests that the dip is probably not due to detector effect. The variation between the two is $< 1\%$. To understand the dip, a model-based work has been performed [3]. There, a dip was observed in the correlation function with AMPT in Pb-Pb collision at 2.76 TeV at low p_T. The depletion was observed for the configuration of AMPT with hadronic rescattering where the radial flow velocity is largest. It was observed that the stronger the radial flow, the stronger the observed effects were. No depletion was found with

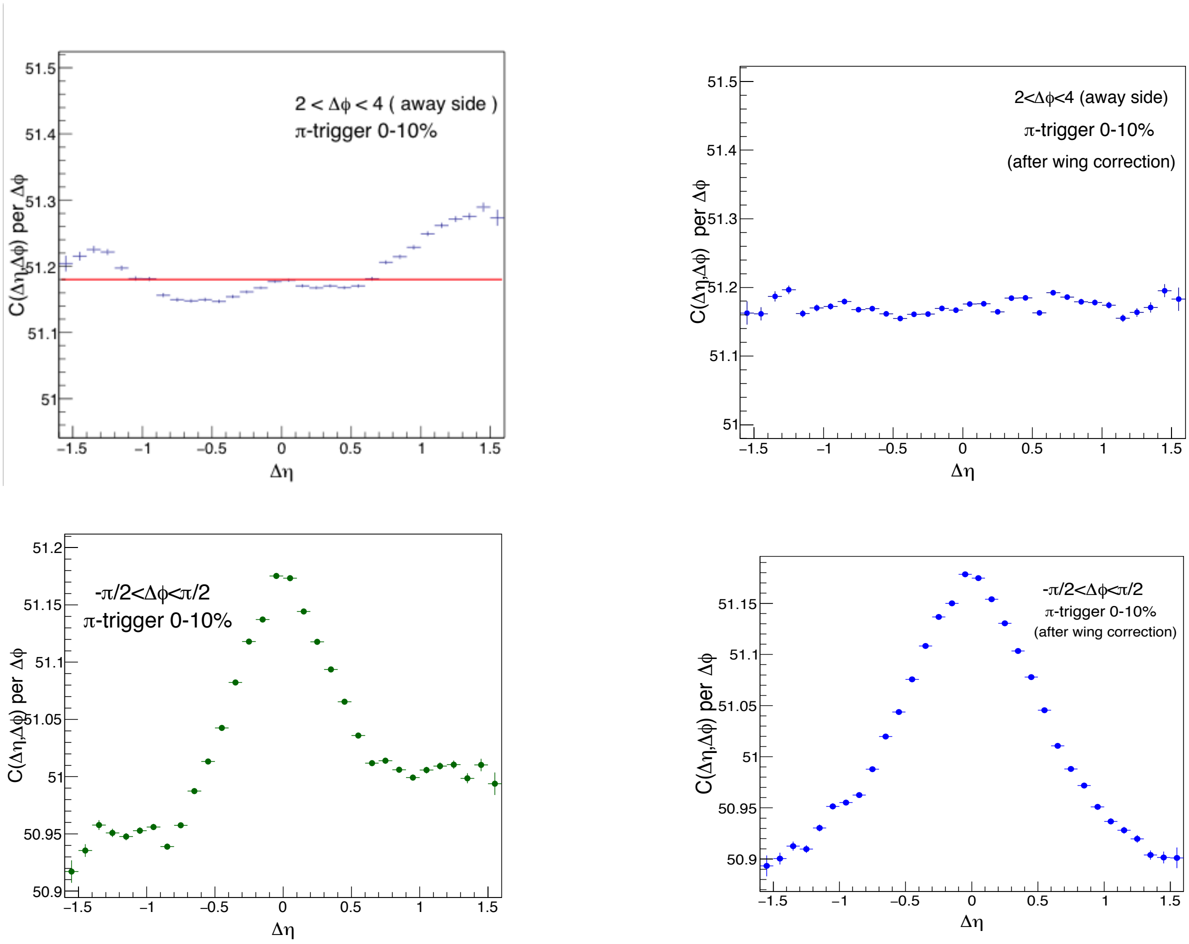

Figure 4.40: $\Delta\eta$ projection of correlation function before wing correction (left panel) and after wing correction (right panel)

the configuration when hadronic rescattering is absent and the radial flow velocity is also small. These studies suggest that the radial flow can be a possible reason for the dip in the correlation function. This needs further detailed investigation.

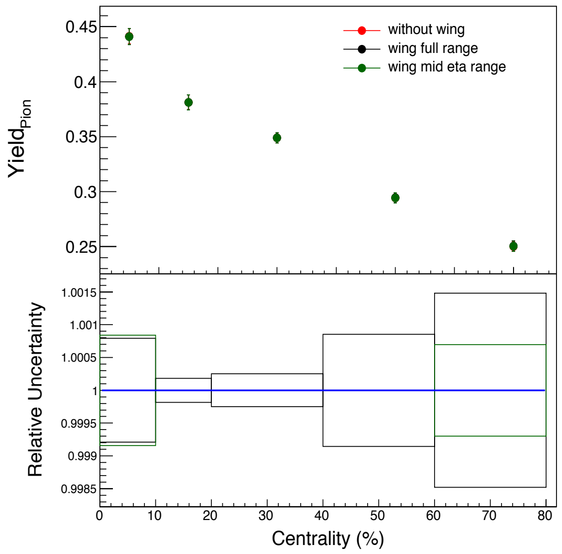

Figure 4.41: Systematic Uncertainty in yield of associated hadrons due to wing correction

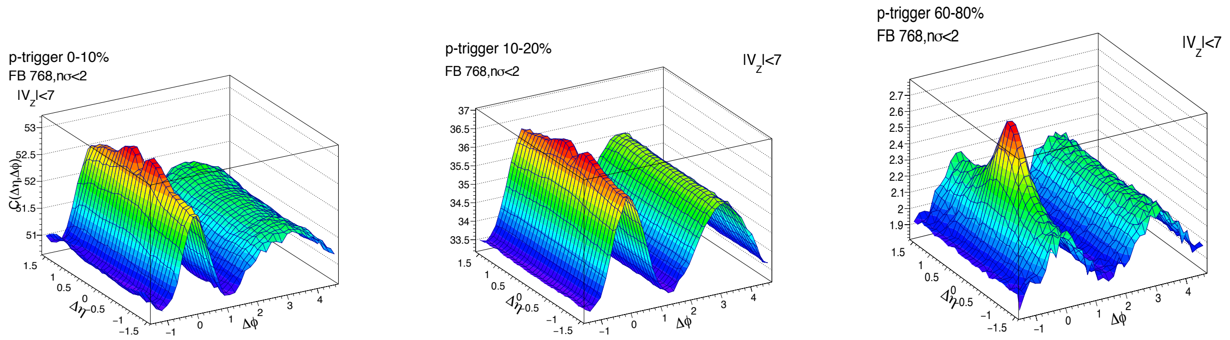

Figure 4.42: proton-triggered correlation function for $|\Delta\eta|$ & $|\Delta\phi| > 0.02$

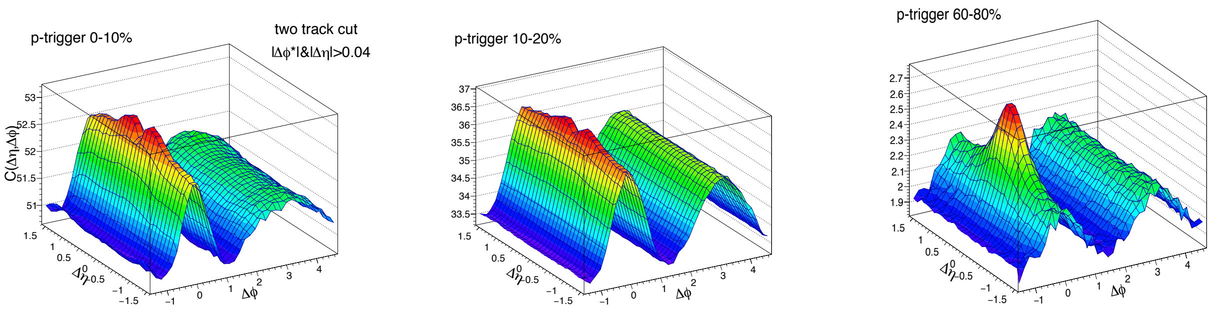

Figure 4.43: proton-triggered correlation function for $|\Delta\eta|$ & $|\Delta\phi| > 0.04$

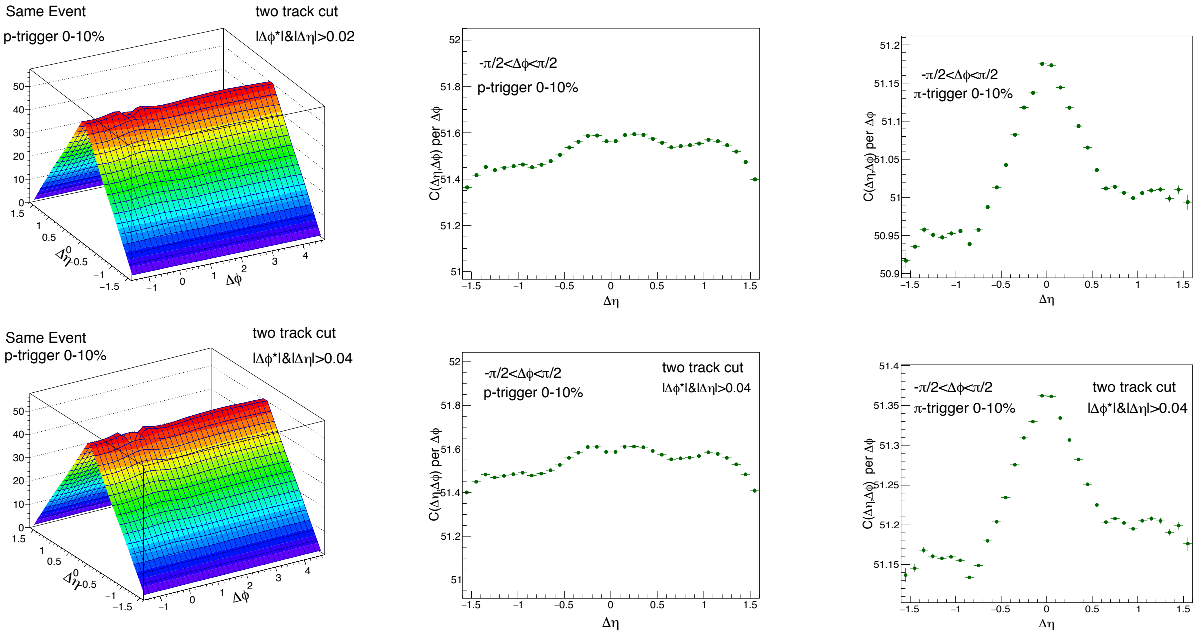

Figure 4.44: projection of proton-triggered correlation function (same event) for $|\Delta\eta|$, $|\Delta\phi| > 0.02$ and $|\Delta\eta|$, $|\Delta\phi| > 0.04$

4.9 Corrected ALICE results (Preliminary)

Final results as approved by the evaluation process in ALICE are shown in Fig 4.45 to 4.47. These results are tagged as "preliminary" ALICE results.

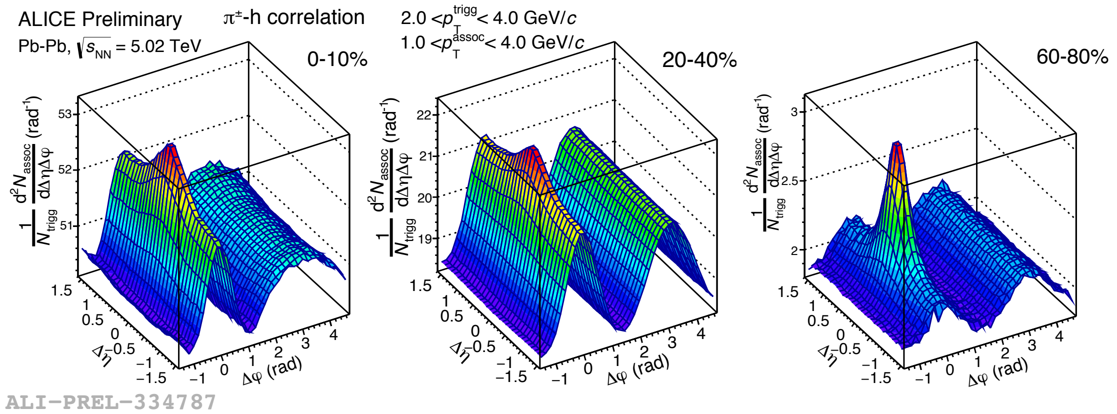

Figure 4.45: Pion triggered 2D correlation for three centralities

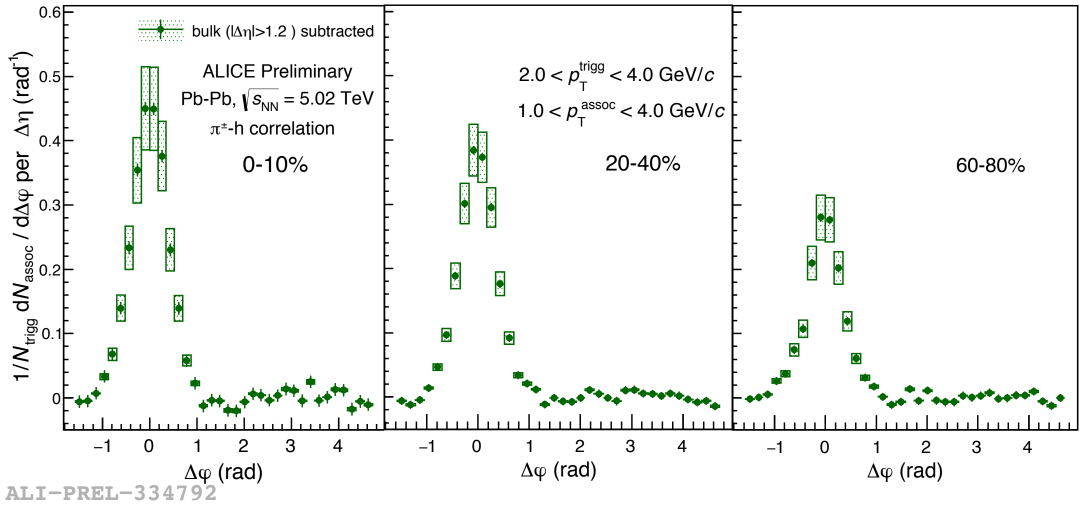

Figure 4.46: $\Delta\phi$-projection of Pion triggered correlation function (statistical errors are shown as vertical lines and systematics errors are as boxes)

The pion-triggered 2D correlation functions for the three centralities are shown in Fig. 4.45. The $\Delta\phi$-projection of the bulk subtracted pion triggered correlation function with statistical and systematic uncertainties are presented in Fig 4.46 and the final near-side yield for pion triggered

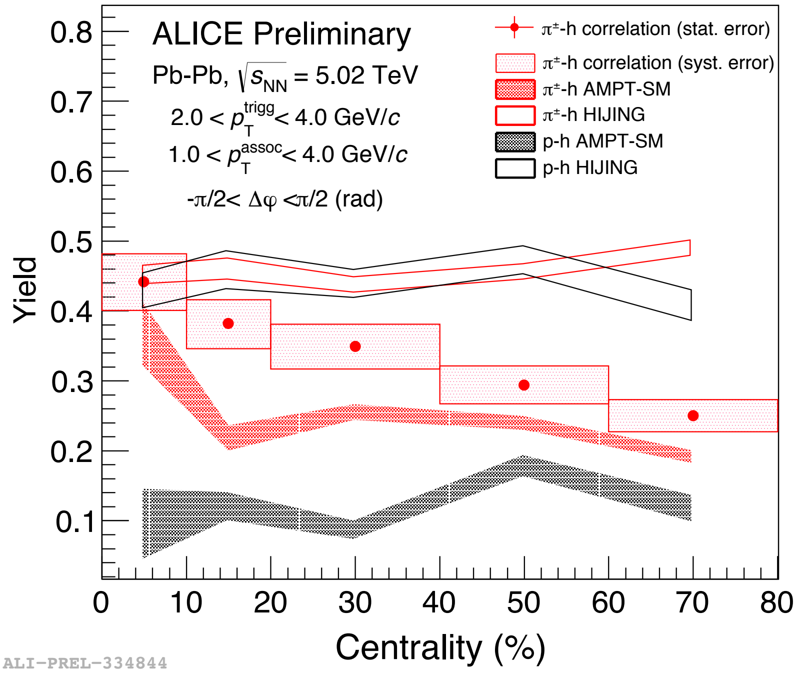

Figure 4.47: Near side pion triggered yield as a function of centrality with model comparison (statistical errors are shown as vertical lines and systematics errors are as boxes)

correlation along with model comparison has been shown in Fig 4.47 with centrality. A detailed study on the purity of protons and the dip in the correlation function is under investigation. The pion trigger yield shows a decreasing trend with centrality. The origin is to be investigated whether from recombination or other sources. For conclusion on recombination, the ratio with the proton-triggered yields is to be extracted with centrality.

In the intermediate pT range, formation of protons via coalescence or recombination rather than fragmentation is more probable than pions. Therefore, the pions in this region are mostly from fragmentation of partons, whereas, protons at that pT are mostly originated from coalescence. Therefore, pions have more number of associated particles with them than protons. So the yield is more for pion-trigger. The AMPT model comparison shows an increasing pion-triggered yield towards most central collision, which is also consistent with data particularly for most central collision and nearly constant proton-triggered yield with centrality. The ratio of proton-triggered yield to pion-triggered yield two gives a hint of dilution in the yield towards most central collision. This will be verified in data when we will have the final results for proton-triggered yield. On the other hand, HIJING results gives almost constant yield with centrality for both pion and proton-triggered correlation.

4.10 Summary

In this analysis, two-particle correlation with pions and protons as trigger particles having $2 \leq p_T \leq 4$ GeV/c and charged hadrons as associated particles with $1 \leq p_T \leq 4$ GeV/c in Pb-Pb collisions at $\sqrt{s_{NN}} = 5.02$ TeV has been studied. Particles are identified using TPC and TOF detectors by combined $n\sigma$ method. Efficiency, purity and correction factors are estimated from Monte Carlo and the correlation functions are weighted with these correction factors. Closure test has been performed to check the validity of the correction factors. Finally, the yields are estimated as a function of centrality and systematic uncertainties are extracted. The yields are compared with models and the final results are presented. The final results show that the pion-triggered yield increases from peripheral to central collisions and AMPT results can describe this trend qualitatively. The AMPT values are also closer to data. The proton-triggered yield from AMPT shows a nearly constant value for all centrality bins which indicates a dilution in proton-triggered yield with respect to pion-triggered yield towards central collisions.

Bibliography

[1] X. N. Wang and M. Gyulassy, HIJING: A Monte Carlo model for multiple jet production in p p, p A and A A collisions, Phys. Rev. D **44** (1991), 3501-3516

[2] Z. W. Lin, C. M. Ko, B. A. Li, B. Zhang and S. Pal, A Multi-phase transport model for relativistic heavy ion collisions, Phys. Rev. C **72** (2005), 064901

[3] J. Adam *et al.* [ALICE], Evolution of the longitudinal and azimuthal structure of the near-side jet peak in Pb-Pb collisions at $\sqrt{s_{\mathrm{NN}}} = 2.76$ TeV, Phys. Rev. C **96** (2017) no.3, 034904 doi:10.1103/PhysRevC.96.034904

Chapter 5

p_T dependence of the correlation between initial spatial anisotropy and final momentum anisotropies in relativistic heavy ion collisions

5.1 Introduction

The anisotropic flow of hadrons is known as one of the key observables produced in relativistic heavy ion collisions that provides a strong indication of the formation of hot and dense Quark Gluon Plasma (QGP) phase and its collective behaviour [1, 2, 3, 4]. The spatial asymmetry in the initial energy density distribution on the overlapping zone between two colliding nuclei gives rise to anisotropic flow in the momentum distribution where the magnitude of the flow parameters depends on several factors such as particle mass, beam energy, collision centrality, transverse momentum.

It is well known that the relativistic hydrodynamics is one of the most successful model frameworks which has been used extensively to study the evolution of the QGP medium in order to estimate the several final state observables [2, 5, 6, 7, 8, 9, 10, 1, 11, 12, 13]. The simultaneous explanation of the experimental data of the elliptic flow coefficient and the charged particle spectra by hydrodynamical model calculations at RHIC energy was one of the initial milestones in this field of research which confirms an early thermalization and collective behaviour of the system produced in relativistic heavy ion collisions [14].

The initial spatial anisotropy (ϵ_n), specially the ellipticity increases significantly from central to mid-central collisions and consequently the magnitude of the elliptic flow coefficient increases towards peripheral collisions. On the other hand, the rise in initial spatial triangularity (ϵ_3) with collision centrality is relatively slower compared to that of ϵ_2. The efficiency of conversion of the initial spatial eccentricity to the final momentum anisotropy depends on the initial state as well as on the evolution of the produced hot and dense matter. Hydrodynamic model calculations can be quite useful to estimate the initial states (obtained by tuning the model parameter to reproduce the experimental data) and also the space time evolution as we cannot get direct information of the initial state from the experimental data.

The relation between the initial spatial anisotropy and the final state anisotropic flow parameters has been studied by several groups earlier [1, 18, 12, 15, 16, 17, 19, 20, 21, 22, 23, 24, 25, 26, 27, 28, 29]. The effect of η/s as well as of the fractional contributions of the number of participants ($N_{\rm part}$) and the number of binary collisions ($N_{\rm coll}$) to the initial entropy and/or energy density production was studied for the first time in an interesting work by Niemi *et. al.* [16] for Au-Au collisions at RHIC energy. The initial state anisotropies and their uncertainties in ultrarelativistic heavy ion collisions have been studied from the Monte Carlo Glauber model by Alvioli *et. al.* [30]. Recent experimental data have shown a correlation between the mean transverse momentum of the outgoing particles and the anisotropic flow parameter in Pb-Pb collisions at the LHC [31]. The correlation between the mean transverse momentum and the anisotropic flow parameter using a hydrodynamical model framework has been studied by Bozek *et. al.* [32, 33]. A recent theory calculation has shown that the magnitude of such correlation can be directly predicted from the initial conditions using the initial spatial anisotropy ϵ_n and the initial energy per unit rapidity [34].

These studies suggest that the particle transverse momentum, beam energy, collision centrality, all play crucial role in determining the final momentum anisotropy. Thus, in order to understand the correlation between ϵ_n and the anisotropic flow better, it is important to know the simultaneous effect of all these parameters in detail.

In this work we study the p_T dependent (linear) correlation between initial ϵ_n and the final momentum anisotropies (v_n) of positively charged hadrons using a state-of-the art hydrodynamical model calculation. We focus on the elliptic and triangular flow parameters and the corresponding initial eccentricities are obtained from a sufficiently large number of events. It has already been shown in the earlier studies that the correlation between ϵ_4 and v_4 is significantly weak [16] and as a result we do not consider this and the other higher order harmonics for the present study. The dependence of the correlation coefficient on collision centrality is studied in detail for three different types of hadrons from Pb-Pb collisions at LHC. The correlation coefficients and the relative fluctuations in the anisotropic flow parameters are calculated for two different η/s values to check the sensitivity of the results to the shear viscosity coefficient.

In the next section we briefly discuss the model framework and the initial state produced in heavy ion collisions. We calculate the p_T dependent correlation coefficients between $\epsilon_n - v_n$ and discuss our results from Pb-Pb collisions at LHC energy in section III and IV. We show the η/s dependence of the correlation coefficient and the relative fluctuations in section V. In section VI, the summary and conclusions of all the results are presented.

5.2 Framework

We use the (2+1) dimensional longitudinally boost invariant hydrodynamical model framework MUSIC [35] with fluctuating initial conditions to calculate the initial spatial anisotropies and the corresponding anisotropic flow parameters from heavy ion collisions at different centrality bins at mid-rapidity. The initial formation time of the plasma is considered as 0.4 fm/c at 2.76A TeV Pb-Pb collisions at the LHC energy.

A Monte Carlo Glauber initial condition is considered and the value of η/s is kept fixed at 0.08 (later we change this value to check the sensitivity of the results to η/s). The initial energy density is considered to be dependent on a linear combination of soft (N_{part}) and hard (N_{coll}) contributions with appropriate weight factors. A constant temperature freeze out is considered and a lattice based equation of state is used for a cross-over transition between the QGP and hadronic matter phases [36]. The centrality bins are selected using an impact parameter range from Ref [37]. The model parameters are set by simultaneously reproducing the experimental data of the final state charged particle multiplicity, p_T spectra and anisotropic flow parameters [38, 39, 40, 41]. The standard Cooper-Frye formula along with the feed down contributions of higher resonances is used to estimate the production of the hadrons from freeze-out surface [42, 35].

The initial spatial eccentricity is calculated using the relation [16]:

$$\epsilon_n = -\frac{\int \mathrm{d}x\mathrm{d}y\ r^n \cos\left[n\left(\phi - \psi_n\right)\right] \varepsilon\left(x, y, \tau_0\right)}{\int \mathrm{d}x\mathrm{d}y\ r^n \varepsilon\left(x, y, \tau_0\right)}\,. \tag{5.1}$$

Where ψ_n is the n^{th} order participant plane angle and ε is the energy density. The corresponding anisotropic flow parameters v_n can be obtained [16] from the invariant particle momentum distribution as :

$$\frac{dN}{d^2p_T dY} = \frac{1}{2\pi}\frac{dN}{p_T dp_T dY}[1 + 2\sum_{n=1}^{\infty} v_n(p_T)\cos \mathrm{n}(\phi - \Psi_\mathrm{n})]\,, \tag{5.2}$$

where Ψ_n is n^{th} order event plane angle.

5.3 Pb-Pb collisions at the LHC

An estimation of the strength of the linear correlation between two variables is obtained by dividing the covariance of the variables by the product of their respective standard deviations. Thus, the correlation coefficient C between the initial spatial eccentricity and final momentum anisotropies can be quantified using the relation [16]:

$$C(\epsilon_n,\, v_n) \;=\; \left\langle \frac{(\epsilon_n - \langle\epsilon_n\rangle_{\mathrm{av}})(v_n - \langle v_n\rangle_{\mathrm{av}})}{\sigma_{\epsilon_n}\sigma_{v_n}} \right\rangle_{\mathrm{av}}. \tag{5.3}$$

The quantities σ_{ϵ_n} and σ_{v_n} are the standard deviations of ϵ_n and v_n respectively. The average is taken over events using hadron multiplicity as weight factor. The correlation coefficient can take any value between -1 to +1. Two quantities are strongly linearly (anti-linearly) correlated when the coefficient is close to 1 (-1). On the other hand, the value of C close to zero implies that the quantities are not correlated linearly.

The correlation coefficients for π^+, K^+ and p from Pb-Pb collisions at different centrality bins are shown in Fig. 5.1. The values of the correlation coefficient of π^+ for 0–20% and 20–40% centrality bins remain almost same at about 0.95. For 40–60% centrality bin, we observe a very small drop in the value of $C(\epsilon_2,\, v_2)$ (to 0.91). Whereas, $C(\epsilon_2,\, v_2)$ drops to a significantly lower value of 0.60 for 60–80% centrality bin. It is to be noted that we have used a larger number of events for peripheral collisions to reduce the statistical uncertainty in the calculation.

The correlation coefficient $C(\epsilon_2,\, v_2)$ for K^+ and p is also found to be large and positive (0.94 and 0.93 for kaon and proton respectively) for 0–20 and 20–40% centrality bins. The value of C is about 0.9 for 40–60% and at 60–80% centrality bin and it drops significantly to a value of about 0.6 for both the particles.

It is well known that the triangular flow of charged particles does not show strong dependence on the collision centrality [43]. However, the initial triangularity of the medium is found to be sensitive to the system size which makes the estimation of correlation coefficient between ϵ_3 and v_3 important.

The correlation coefficient C(ϵ_3, v_3) is about 0.75, 0.68 and 0.4 for 0-20%, 20-40% and 40-60% centrality bins respectively for all π^+, K^+, and p at LHC. For 60–80% centrality bin, we see a complete absence of linear correlation as the value of C is found to be close to zero.

The variation of correlation strength with collision centrality is shown in Fig. 5.1. The correlation strength for π^+, K^+, and p is found to be close to each other although the (p_T integrated) anisotropic flow is different for them. We also see that C(ϵ_3, v_3) shows a stronger sensitivity to the collision centrality as it decreases faster for peripheral collisions compared to C(ϵ_2, v_2) as expected.

We estimate error in the correlation coefficient calculation with finite number of events. The statistical errors in the correlation coefficients for (ϵ_2, v_2) and (ϵ_3, v_3) are found to be less than 1% and 2% respectively.

5.4 correlation between ϵ_n and $v_n(p_T)$

We understand that the final p_T integrated anisotropic flow parameter is a consequence of the initial spatial deformation of the medium formed in heavy ion collisions. Although the magnitude of both the elliptic flow and the spatial anisotropy increases while going away from central collisions, the correlation strength between ϵ_2 and v_2 decreases towards peripheral collisions. We see similar

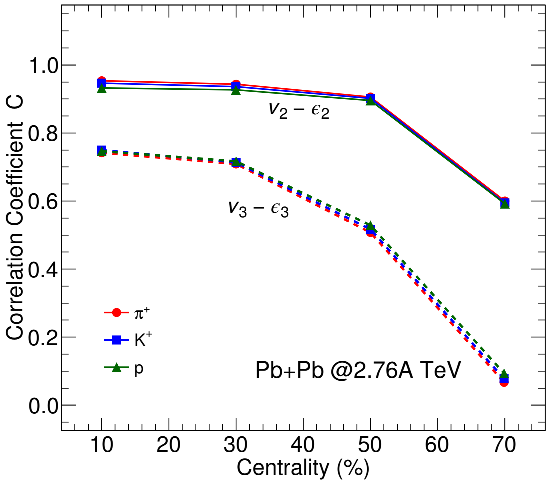

Figure 5.1: (Color online) C(ϵ_n, v_n) as a function of centrality from 2.76A TeV Pb-Pb collisions at LHC.

reduction in correlation strength with collision centrality between ϵ_3 and v_3 as well.

The values of the correlation strength C($\epsilon_n,\ v_n$) for all π^+, K^+ and p are found to be similar as a function of centrality and do not depend on the particle mass significantly as shown in Fig. 5.1. We know that the mass ordering of differential anisotropic flow ($v_n(p_T)$) parameters is a signature of the collective behaviour of the medium formed in heavy ion collisions and it is well explained by hydrodynamical model calculation. Thus, it is important to know if there also exists any mass dependence in the p_T dependent correlation coefficients for the different hadrons and the underlying mechanism does not depend on the particle mass significantly which results in a similar correlation strength for them.

It is to be noted that the freeze-out temperature plays a crucial role in determining the p_T dependent correlation coefficient even though with our simplified assumption of constant temperature freeze-out for all hadrons. Some earlier studies have shown that the differential anisotropic flow parameter is sensitive to the freeze-out temperature mostly towards larger $p_T (> 1 - 1.5$ GeV/c) region [22]. A detailed study using dynamical freeze-out conditions would be important, however the present study is also expected to provide valuable insight about the correlation between the initial geometry and the final anisotropic flow parameters.

The correlation coefficient C(ϵ_n, $v_n(p_T)$) for π^+, K^+, p at different centrality bins is shown in Figs 5.2, 5.3, and 5.4 respectively. A clear mass dependence in the correlation coefficient between $\epsilon_2 - v_2$ can be seen for all the centrality bins. The value of $C(\epsilon_2, v_2(p_T))$ is found to be larger for lighter particles in the p_T region 0.1 to 2 GeV/c shown in the figs.

The strength of $\epsilon_2 - v_2$ correlation for pions remain close to 0.9 in the p_T region of 0.2 to 2 GeV/c for all three centrality bins and then drops slowly for higher p_T values. At very low p_T (< 0.3 GeV), the value of C for π^+ is smaller, as those may be emitted from the initial few fm time period when the build up of transverse flow is not very strong and the elliptic flow $v_2(p_T)$ is also small. We see a relatively stronger p_T dependent correlation for K^+ and p where the coefficients for them fall sharply with smaller p_T values in the region $p_T < 1$ GeV/c. The correlation coefficient is found to be slightly higher for heavier particles in the region $p_T > 2$ GeV/c.

The correlation between $\epsilon_3 - v_3$ as a function of p_T also shows a behaviour similar to $\epsilon_2 - v_2$ although the magnitude is considerably smaller. The strength of the correlation for protons is found to be very small below $p_T = 0.5$ GeV/c for all centrality bins. We see that C($\epsilon_n, v_n(p_T)$) drops faster towards the peripheral collisions for n=3 compared to n=2 at higher p_T values.

These results clearly show that the p_T dependent correlation coefficient strongly depends on the mass of the particle and p_T region that contributes maximum to the correlation strength is also different for different particles.

Fig 5.5 shows the $\langle v_n \rangle / \langle \epsilon_n \rangle$ as a function of centrality for Pb-Pb collisions. The slope (C_n) between two linearly correlated variables ϵ_n and v_n can be written as $v_n = C_n \epsilon_n + \delta$. After averaging over large number of events the slope is simply $C_n = \langle v_n \rangle / \langle \epsilon_n \rangle$ as $\langle \delta \rangle$ is zero [16]. The C_3 for Pb-Pb collisions falls faster than C_2 towards peripheral collisions.

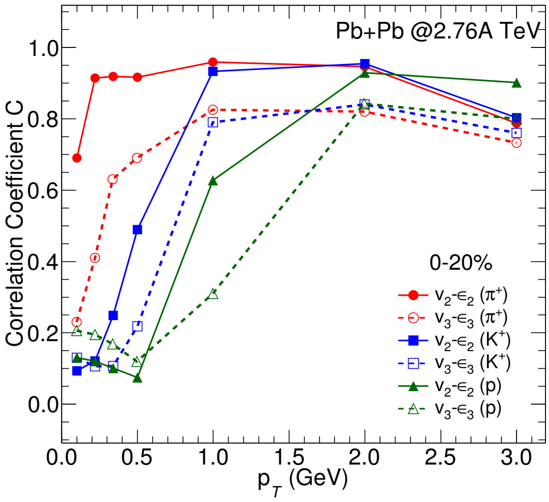

Figure 5.2: (Color online) Correlation between ϵ_n and $v_n(p_T)$ for π^+, K^+ and p at $\sqrt{s_{NN}}$ =2.76 TeV Pb-Pb collisions for $0-20\%$ centrality bin.

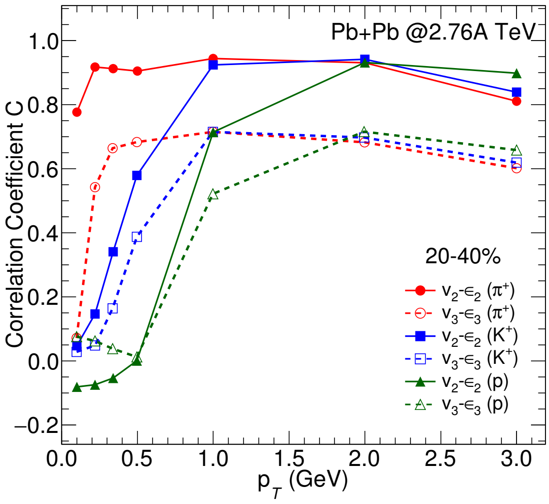

Figure 5.3: (Color online) Correlation between ϵ_n and $v_n(p_T)$ for π^+, K^+ and p at $\sqrt{s_{NN}} = 2.76$ TeV Pb-Pb collisions for $20-40\%$ centrality bin.

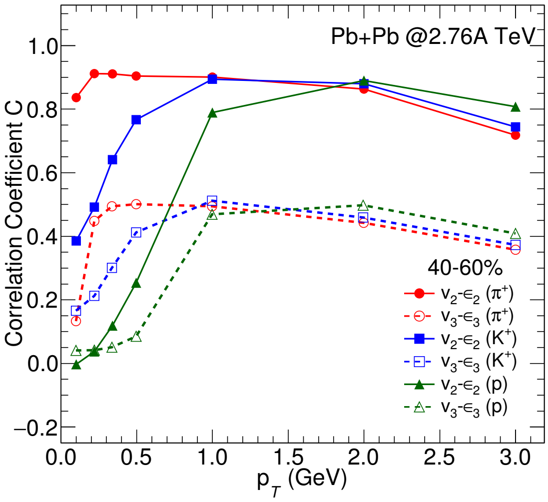

Figure 5.4: (Color online) Correlation between ϵ_n and $v_n(p_T)$ for π^+, K^+ and p at $\sqrt{s_{NN}} = 2.76$ TeV Pb-Pb collisions for $40 - 60\%$ centrality bin.

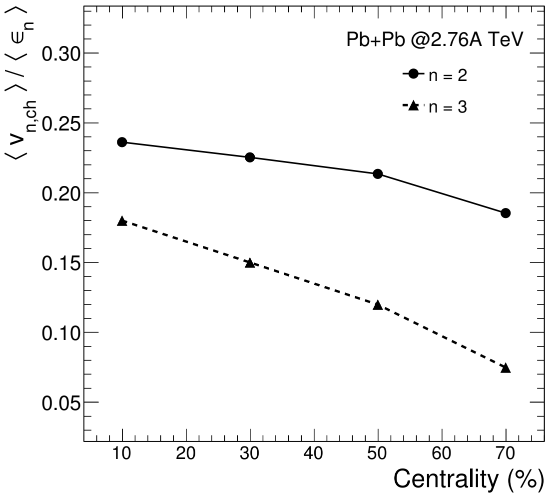

Figure 5.5: (Color online) The ratio of $\langle v_n \rangle$ and $\langle \epsilon_n \rangle$ as a function of collision centrality.

5.5 η/s dependence

The dependence of the $\epsilon_n - v_n$ correlation on the value of η/s has been studied in detail in the literature. It has been shown in Ref. [16] that the higher order correlation coefficients are more sensitive to the value of the η/s. In Fig 5.6, we show the correlation coefficients for two different η/s values for 20–40% and 40–60% Pb-Pb collisions at the LHC. The value of C for all the three particles are found to vary only marginally when η/s is changed from 0.08 to 0.16. A better understanding of the initial state from the final state flow observables has always been a primary goal for flow analysis in heavy ion collisions. Due to the varying relation of the linear response parameter with multiplicity, it is challenging to relate the initial anisotropy to the final state momentum anisotropy in a linear fashion. The relative fluctuation in the anisotropic flow parameters $\sigma_{v_n}/\langle v_n\rangle$ is considered to be a potential observable, reflecting the ratio of the first two moments of the initial state eccentricity distribution (i.e, σ_{ϵ_n}). The relative fluctuations in the anisotropic flow parameters for the same set of collisions are shown in Fig. 5.7. Interestingly, the relative fluctuation $\sigma_{v_n}/\langle v_n\rangle$ as a function of p_T is found to be quite sensitive to the value of η/s. One can see from the figures that the sensitivity to the value of η/s is much stronger for protons than for pions and also in the low $p_T(< 1$ GeV) region for Pb-Pb collisions.

5.6 summary and Conclusions

We calculate the correlation between the initial spatial anisotropy and the final momentum anisotropy for positively charged π, K and p from 2.76A TeV Pb-Pb collisions at LHC and at different centrality bins using an event-by-event viscous hydrodynamic model framework with fluctuating initial conditions.

The linear correlation is found to be stronger for central collisions than for peripheral collisions

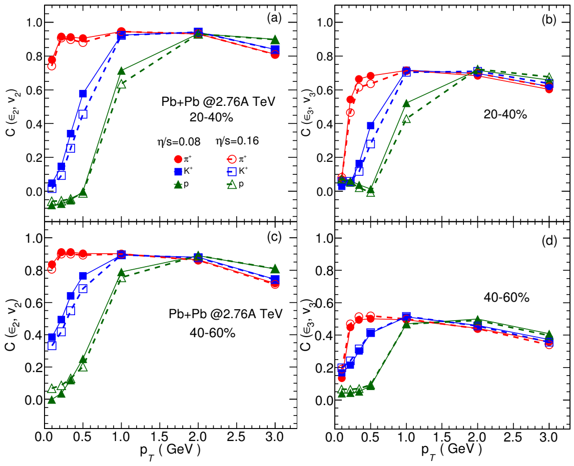

Figure 5.6: (Color online) p_T dependent correlation coefficients at the LHC considering two different η/s values.

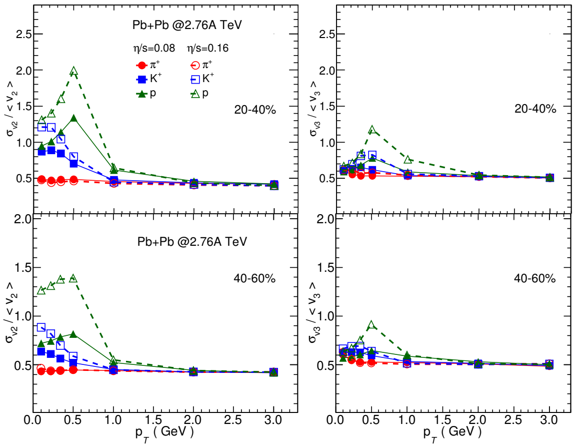

Figure 5.7: (Color online) Relative fluctuations in the anisotropic flow parameters at the LHC considering two different η/s values.

for all the particles studied. In addition, the correlation between $\epsilon_3 - v_3$ is found to be weaker than $\epsilon_2 - v_2$. However, the correlation between $v_n(p_T)$ and ϵ_n as a function of p_T shows interesting behaviour where the correlation coefficient C is found to depend strongly on the mass of the particles. We see a clear ordering of the correlation coefficient in the lower p_T region depending on the particle mass where the correlation strength is found to be larger for lighter particles. The p_T range for the ordering depends on the collision centrality. The p_T dependent correlation strength is found to rise with p_T, reach maximum, and then drop slowly beyond p_T= 2 GeV/c for the Pb-Pb collisions. The correlation strength for π^+ reaches maximum at a relatively smaller p_T value than for K^+ and protons. Although the strength of the correlation between ϵ_3 and v_3 is found to be relatively weaker compared to ϵ_2 and v_2, we see a similar qualitative p_T dependent behaviour of correlation co-efficient for both of them.

The correlation coefficient is found to depend only marginally on the value of η/s. However, the relative fluctuations in the anisotropic flow parameter show strong sensitivity to the value of η/s. The value of $\sigma_{v_n}/\langle v_n \rangle$ is found to be significantly larger for larger η/s for heavier particle and in the region $p_T < 1$ GeV.

Bibliography

[1] H. Stoecker and W. Greiner, Phys. Rept. **137**, 277-392 (1986).

[2] P. Kolb and U Heinz, Hydrodynamic description of ultrarelativistic heavy ion collisions Quark gluon plasma, R. C. Hwa (ed.) *et al.*, p634 (2003).

[3] U. Heinz and R. Snellings, Ann. Rev. Nucl. Part. Sci. **63**, 123 (2013).

[4] R. S. Bhalerao, Pramana - J Phys **61**, 1021(2003).

[5] P. Huovinen, in Quark Gluon Plasma 3 , edited by R. C. Hwa and X. N. Wang (World Scientific, Singapore, 2004), p. 600 [nucl-th/0305064];

[6] D. A. Teaney, arXiv:0905.2433 [nucl-th].

[7] P. F. Kolb, J. Sollfrank, and U. Heinz Phys. Rev. C **62**, 054909 (2000).

[8] D. Teaney, J. Lauret, E.V. Shuryak, arXiv:0110037 [nucl-th].

[9] P. Huovinen and P. V. Ruuskanen, Ann. Rev. Nucl. Part. Sci. **56**, 163 (2006).

[10] P. Romatschke and U. Romatschke, Phys. Rev. Lett. **99**, 172301 (2007);

[11] J. Y. Ollitrault, Eur. J. Phys. **29**, 275-302 (2008).

[12] A. Jaiswal and V. Roy, Adv. High Energy Phys. **2016**, 9623034 (2016).

[13] L. Yan, Chin. Phys. C **42**, 042001 (2018).

[14] P. F. Kolb and U. W. Heinz, [arXiv:nucl-th/0305084 [nucl-th]].

[15] G-Y. Qin, H. Petersen, S. A. Bass, and B. Muller, Phys. Rev. C **82**, 064903 (2010).

[16] H. Niemi, G. S. Denicol, H. Holopainen and P. Huovinen, Phys. Rev. C **87**, no.5, 054901 (2013).

[17] A.K. Chaudhuri, R. Haque, V. Roy, and B. Mohanty, Phys. Rev. C **87**, 034907 (2013).

[18] F. G. Gardim, F. Grassi, M. Luzum, J.-Y. Ollitrault, Phys. Rev. C **85**, 024908 (2012).

[19] A. K. Chaudhuri, Phys. Lett. **B713**, 91-92 (2012).

[20] L. Ma, G. L. Ma, and Y. G. Ma, arXiv:0610:04733

[21] A. Bzdak, B. Schenke, P. Tribedy, and R. Venugopalan, phys. Rev. C **87**, 064906 (2013).

[22] V. Greco, M.Colonna, M. Di Toro, G.Ferini Prog. in part. and Nucl. Phys **62**, 562, 2009.

[23] B. H. Alver, C. Gombeaud, M. Luzum and J. Y. Ollitrault, Phys. Rev. C **82**, 034913(2010).

[24] J. Noronha-Hostler, L. Yan, F. G. Gardim, and J.-Y. Ollitrault, Phys. Rev. C **93**, (2016).

[25] P. Alba, V. Mantovani Sarti, J. Noronha, J. Noronha-Hostler, P. Parotto, I. Portillo Vazquez, and C. Ratti, Phys. Rev. C **98**, 034909 (2018).

[26] M. Sievert and J. Noronha-Hostler, Phys. Rev. C **100**, 024904 (2019).

[27] R. Snyder, M. Byres, S.H. Lim, J.L. Nagle, arXiv:2008:08729

[28] M. Luzum, C. Gombeaud, and J.-Y. Ollitrault, Phys. Rev. C **81**, 054910 (2010).

[29] F. G. Gardim, F. Grassi, M. Luzum, and J. Noronha-Hostler, Phys. Rev. C **95**, 034901 (2017).

[30] M. Alvioli, H. Holopainen, K. J. Eskola, and M. Strikman, Phys. Rev. C **85**, 034902 (2012).

[31] G. Aad *et. al.*, Eur. Phys. J C **79** , 985 (2019).

[32] P. Bozek, Phys. Rev. C **93**, 044908 (2016).

[33] P. Bozek and H. Mehrabpour, Phys. Rev. C **101**, 064902 (2020).

[34] G. Giacalone, F. G. Gardim, J. Noronha-Hostler and J. Y. Ollitrault, Phys. Rev. C **103** no.2, 024909 (2021) .

[35] B. Schenke, S. Jeon, and C. Gale, Phys. Rev. C **82**, 014903 (2010).

[36] P. Huovinen and P. Petreczky, Nucl. Phys. A **837**, 26-53 (2010).

[37] B. Abelev *et al.* [ALICE], Phys. Rev. C **88** (2013)no.4,044909 doi:10.1103/PhysRevC.88.044909 [arXiv:1301.4361 [nucl-ex]].

[38] B. Alver *et al.* [PHOBOS], Phys. Rev. Lett. **96** (2006), 212301 doi:10.1103/PhysRevLett.96.212301 [arXiv:nucl-ex/0512016 [nucl-ex]].

[39] B. Alver *et al.* [PHOBOS], Phys. Rev. Lett. **102** (2009), 142301 doi:10.1103/PhysRevLett.102.142301 [arXiv:0709.4008 [nucl-ex]].

[40] A. Adare *et al.* [PHENIX], Phys. Rev. C **92** (2015) no.3, 034913 doi:10.1103/PhysRevC.92.034913 [arXiv:1412.1043 [nucl-ex]].

[41] J. Adam *et al.* [ALICE], Phys. Rev. C **93** (2016) no.3, 034913 doi:10.1103/PhysRevC.93.034913

[42] F. Cooper and G. Frye, Phys. Rev. D **10**, 186 (1974).

[43] H. Petersen, G. Y. Qin, S. A. Bass and B. Muller, Phys. Rev. C **82**, 041901 (2010).